Spring 5-15-2020

Studies of Maximum Supercooling and Stirring in Levitated Liquid Metallic Alloys

Mark Edward Sellers
Washington University in St. Louis

Recommended Citation

Sellers, Mark Edward, "Studies of Maximum Supercooling and Stirring in Levitated Liquid Metallic Alloys" (2020). *Arts & Sciences Electronic Theses and Dissertations*. 2242.
https://openscholarship.wustl.edu/art_sci_etds/2242

WASHINGTON UNIVERSITY IN ST. LOUIS

Department of Physics

Dissertation Examination Committee:
Kenneth F. Kelton, Chair
Katharine Flores
Erik Henriksen
Zohar Nussinov
Li Yang

Studies of Maximum Supercooling and Stirring in Levitated Liquid Metallic Alloys

by
Mark Edward Sellers

A dissertation presented to
The Graduate School
of Washington University in
partial fulfillment of the
requirements for the degree
of Doctor of Philosophy

May 2020
St. Louis, Missouri

Table of Contents

List of Figures

List of Tables

List of Abbreviations

ANL	Argonne National Laboratory
APS	Advanced Photon Source
BCC	Body Centered Cubic
BESL	Beamline Electrostatic Levitator
BESL2013	X-ray scattering experiments performed during Summer 2013
BESL2016	X-ray scattering experiments performed during Summer 2016
CFD	Computational Fluid Dynamics
CNT	Classical Nucleation Theory
DIT	Diffuse Interface Theory
DLR	Deutsches Zentrum für Luft- und Raumfahrt (German Aerospace Institute)
DTA	Differential Thermal Analysis
EML	Electromagnetic Levitation
ESA	European Space Agency
ESL	Electrostatic Levitation
ISRO	Icosahedral Short-Range Order
ISS	International Space Station
KKZNT	Avoided Critical-Point Theory of Viscosity
LED	Light Emitting Diode
NESL	Neutron Electrostatic Levitator
ORNL	Oak Ridge National Laboratory
Pa·s	Pascal seconds
PSD	Position Sensitive Detection
SNS	Spallation Neutron Source

SRD	Science Requirement Document
VUV	Vacuum Ultraviolet Lamp
WU-BESL	Washington University Beamline Electrostatic Levitator

Acknowledgments

I want to first acknowledge Prof. Ken Kelton. He kept me going forward to overcome the challenges of maintaining, upgrading, and running the ESL. From his example, I've learned a tremendous amount about physics, from questions about theory, to practical issues related to experimental procedures, equipment, and laboratory training and safety. I will carry the skills and acumen learned under your mentorship into my future career. Dr. Anup Gangopadhyay deserves recognition for his extensive knowledge of nucleation, metallic liquids, and his supporting work using the EML on the ISS. With his help, I learned how to make pristine samples for nucleation studies and acquired data from the space station for analysis.

I want to applaud the work of several staff members in the physics department. First up are the great craftsmen of the machine shop—Todd Hardt, Denny Huelsman, Nathan Lundak, and Tony Biondo. They are skilled professionals who can work magic with machines and metal. Their help, both in manufacturing new ESL parts from my amateur blueprints and training me on how to use the machine shop, was instrumental resolving many of the challenges I faced. Sarah Akin has always been a helpful resource and generously offered her time and advice when I needed it. Her input enabled me to navigate the forms, deadlines, and procedures needed to pave the path towards my degree. Linda Trower, in addition to her great conversations and wit, was instrumental in helping me file innumerable purchase orders for ESL parts. Shirley McTigue also deserves recognition and thanks for her willingness to help me with questions of funding, both from my NSF Fellowship and for conference travels.

I want to acknowledge several of the previous graduate students from the Kelton lab. I would have felt totally lost without the LabVIEW analysis programs written by or published research from Dr. James Bendert, Dr. Matt Blodgett, Dr. Mark Johnson, or Dr. Rongrong Dai. Several graduate students within the group deserve individual recognition and appreciation. Dr. Chris Pueblo helped train me on experimental and data analysis techniques. Dr. Robert Ashcraft was always willing to help me with ESL issues, debugging code, answering questions, or just talking and enjoying each other's company. I will always remember the time I spent with him during the BESL2016 run and how he kept going forward despite great challenges. I am thankful for Robert's patience when answering my questions. Daniel Van Hoesen has been a great co-worker and always willing to work through experimental and theoretical problems. His extensive python knowledge enabled me to write my curve fitting program central to my research. The ESL and my research both benefitted from Daniel's and Robert's knowledge of electronics, diagnostic and troubleshooting abilities, and efforts on the new TargetPC, PSD box, and A to D cards. Xinsheng Xia was also a great lab companion and always someone I could talk to about nucleation or lab safety.

A special thanks goes to Dr. Dante Quirinale at Oak Ridge National Laboratory, who taught me how to gain-switch on the ESL so I could acquire the data discussed in Chapter 5. His help, camaraderie, mentorship, and friendship guided me through the many challenges of my Ph.D. studies. I especially appreciate his companionship and enlightening conversations during the 2018 Oak Ridge scattering run.

I want to also recognize my previous advisors at Rhodes College, Prof. Brent Hoffmeister and Prof. Ann Viano. Even after I had graduated from Rhodes, Brent and Ann were always willing to offer help and advice and insights about graduate school. Brent's phrase of "eyes on the prize" kept me focused on the goal of this endeavor—earning the degree and learning to become a scientist. Likewise, I also want to acknowledge Prof. Jim Miller—Brent's Ph.D. advisor at Wash U—for his close mentorship when I was his TA for Physics of the Heart and throughout my graduate studies.

I gratefully acknowledge my sources of funding, namely partial support by the National Science Foundation Graduate Research Fellowship under Grant No. DGE-1745038 and by the National Aeronautics and Space Administration Grant No. NNX16AB52G. The NSF GRFP in particular was a talisman through my graduate studies, affording me financial peace-of-mind and several opportunities for new experiences. Also, I acknowledge the U.S. Department of Energy, Basic Energy Science, Office of Science, under contract DE-AC02-06CH11357 for their generous support of scattering studies at the Advanced Photon Source.

I would like to thank my family, both immediate and extended, for all of their love and support through my graduate school career. They always offered an ear when I needed to vent, a hug when I needed comfort, and love and encouragement when I needed inspiration. They offered this support even when they had no idea what I was doing or what had gone wrong. My parents, sisters, aunts, uncles, and grandparents would listen, sympathize, offer suggestions, and push me forward. What Profe Henager and Profe Doyle at Rhodes College said is true—*la familia Sellers es súper*—and I will never take that for granted.

Finally, I want to thank my partner, Sarah Nelson. You appeared in my life at just the right moment when I began my research. When I think about my graduate school career, you always appear as a guiding star. You've seen me at my best and at my worst and stayed with me through all of it. Even half-way across the country from New York City, I still feel your love and support keeping me going through these experiences. Better yet, I feel our relationship continuing to grow and strengthen with each passing day. A frequent theme throughout my undergraduate and graduate studies has been "relationships matter" and my relationship with you matters the most to me.

Mark Sellers

Washington University in St. Louis

May 2020

Dedicated to my family.

ABSTRACT OF THE DISSERTATION

Studies of Maximum Supercooling and Stirring in Levitated Liquid Metallic Alloys

by

Mark Edward Sellers

Doctor of Philosophy in Physics

Washington University in St. Louis, 2020

Professor Kenneth F. Kelton, Chair

Nucleation—or the formation of some cluster in a medium undergoing a phase transition—is usually the initial step in a phase transition. However, this process is still not fully understood, as outstanding questions related to the role of structure, local order, and diffusion remain unanswered. Systematic supercooling studies on metallic liquids performed using electrostatic and electromagnetic (ESL and EML, respectively) will be presented and discussed within the context of several nucleation theories, such as the Classical Nucleation Theory, Diffuse Interface Theory, and Coupled-Flux theory. To study the role of diffusion on nucleation, studies on the International Space Station using the on-board EML were performed. Initial results suggest that diffusion becomes an important factor for nucleation in quiescent liquids, as predicted by the Coupled-Flux theory. Initial results on several metallic liquids (Ti-Zr-Ni, Zr-Pt, Zr-Pd, Cu-Zr) using ground-based ESL techniques suggest that the local order in the liquid, structure of the nucleating phase, and number of phases formed are important factors to consider to understand nucleation.

Chapter 1: Introduction to Nucleation

1.1 A Historical Overview of Nucleation

To nucleate means to form some initial cluster in a medium undergoing a phase transition, such as a liquid droplet from a saturated gas or a crystallite from a liquid or glass. One of the simplest examples of nucleation is the formation of carbon dioxide bubbles within a glass of champagne, where small flecks of dust or cracks within the glass act as nucleation sites for dissolved carbon dioxide. When the size of the nucleated clusters of condensed carbon dioxide passes a critical size, they are favored to continue growing until the buoyancy force on the droplet equals the capillarity force holding the bubble to the crack or dust particle. At this point, the bubble will break free and grow as it floats up to the surface.

A key distinction between nucleation and other aggregation processes is that nucleation is stochastic—or random—and relies on small fluctuations within the parent phase to generate the new phase. These small fluctuations can sometimes bring particles together and, if enough particles come together, a nuclei can form and transform the parent phase into the new phase. However, certain requirements on the nuclei's size must be met before this phase transformation can occur. In other words, there exists a nucleation barrier, which is responsible for many of the historical examples explained below and for much of the data presented in this dissertation. Therefore, nucleation and the nucleation barrier are key to understanding processes that rely on phase transitions, from the Czochralski process for nucleating and growing single crystal silicon used in computer chips, to the crystallization of glass into a glass-ceramic (known by the brand name Corning Ware), to more worldly phenomenon like cloud formation.

Some of the earliest recorded scientific literature on nucleation came from Fahrenheit in 1721, where he discovered that boiled water stored in a clean and sealed glass container could be kept outside overnight in temperatures as low as 15 °F and remain a liquid [1]. However, disturbing the supercooled liquid by shaking the container, as Fahrenheit discovered when he tripped while carrying the glass vial, or introducing a seed crystal, could spur the crystallization of the supercooled water into ice. In both cases, Fahrenheit found the temperature of the mixture in the container would rise back up to 32 °F, a process now known as recalescence, where the heat of fusion is released from the material as it forms the ordered crystal phase.

Other studies on the supercooling of water, described in the letter Professor Joseph Black's sent to Sir John Pringle in 1775, have confirmed and extended Fahrenheit's discovery [2]. Since then, as outlined in Angell's 1983 review [3], water has been supercooled to -31 °C (-24 °F) in bulk and -34 °C (-29 °F) in a capillary, while a more recent study has supercooled water to 232 K (-42 °F) [4]. In these cases, the nucleation barrier is related to the cleanliness of water and the container. The deep supercooling of water, as reported by Angell, requires the removal of nucleating impurities through "very laborious and painful procedures… [such as]…prolonged distillation of the primary water sample" [3]. As should be clear for the rest of this dissertation, minimizing heterogeneous nucleation sites and contamination is key to studying supercooled liquids and homogeneous nucleation.

Studies of nucleation have extended beyond water, like in the experiments on supersaturated salt solution reported by Lowitz [5] and later Gay-Lussac [6,7] in the late eighteenth and early nineteenth centuries. Lowitz's studies were some of the first reported observations of supersaturation. Lowitz's work also demonstrated the technique of seeding, whereby a crystal of the same salt is introduced into the solution, catalyzing the growth of crystals out of solution and onto the seed. Today, a similar process is used to make rock candy from supersaturated sugar water or highly ordered single-crystal silicon for computer chips with the Czochralski process. Lowitz noted that his observations of catalyzed crystallization were analogous to Fahrenheit's observations in supercooled water. Gay-Lussac's work further supported Fahrenheit's observations that mechanically disturbing the supersaturated liquid by shaking or scratching it could induce crystallization. Furthermore, Gay-Lussac showed that supersaturation is a general phenomenon.

These studies were some of the first suggestions of phase metastability, described by Kelton and Greer as:

> "[a] state for which the free energy has a local minimum…[where] the system is stable to small fluctuations…but will eventually evolve (possibly after an extremely long time) to a more stable state." [8]

A schematic representation of a free-energy curve and the corresponding phase evolution is shown in Fig. 1.1, reproduced from [8] with permission from Elsevier. In this case, the nucleation barrier can be understood as the energy required to move from the metastable equilibrium (liquid water below its freezing temperature) to the point of unstable equilibrium, where the smallest fluctuations will be enough to trigger formation of the stable phase.

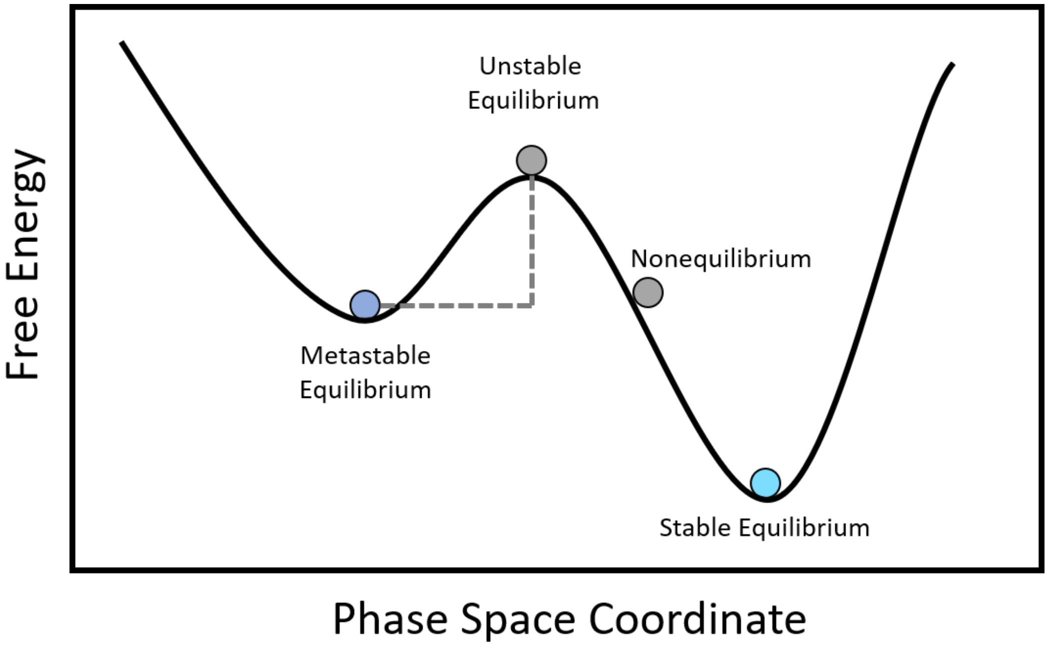

Figure 1.1: A schematic representation of the process by which a metastable state evolves to a stable state. As the barrier between metastable and stable equilibriums shrinks (indicated by dashed lines), smaller and smaller fluctuations are required to transform to the stable phase. The colors represent water (left) and ice (right). Reproduced from [8] with permission from Elsevier.

Gibbs, through a thermodynamic treatment of this problem, first proposed that metastable phases transformed by a nucleation and growth process, while unstable phases transformed via a spinodal process [9] and that a clear distinction existed between the two mechanisms. In the case of nucleation, a system quenched into the metastable region shown in Fig. 1.1 would generally show a droplet morphology due to large, short-range chemical fluctuations and phase separation. A system quenched to the unstable region, in contrast, would show an interconnected structure due to long-range, small-amplitude fluctuations. However, as reported by Kelton and Greer:

> "Gibbs was primarily concerned with processes occurring near equilibrium where the probability of a significant number of fluctuations leading to the stable phase is infinitesimal, corresponding to a large barrier to the phase transition. When the system is quenched deeply into the metastable region, this barrier decreases until it becomes of the same order as the thermal energy." [8]

Far from equilibrium, as shown through density functional calculations, the nucleation barrier either exists and is small (on the order of thermal energy) or vanishes [8]. Since spinodal transformations are characterized by no nucleation barrier and a regularity in order parameter spacing, it would be challenging to positively identify which mechanism is responsible for the transformation through structure alone. Some studies of Cu-Co binary alloys may have observed spinodal transformations for small concentrations of Co using electron microscopy and small-angle scattering techniques [10]; however, other studies failed to observe the characteristic regularity in particle spacing [8].

As will be described in detail later, Volmer and Weber evolved Gibbs's ideas for liquid condensation from a vapor by arguing that the metastability of the supersaturated phase must be due to kinetics [11]. These calculations would be revisited by Becker and Döring [12], forming the Classical Theory of Nucleation (CNT), which would later be adapted for liquid-to-crystal transformations by Turnbull and Fisher [13].

Since then, many liquids have been supercooled below their melting temperatures, but it wasn't until the early 1950s when Turnbull and Cech discovered that metallic liquids could be supercooled as well [14–16]. At the time, only a few degrees of supercooling could be achieved before the metallic liquid crystallized, whereas Turnbull and Cech developed new experimental methods that showed that metals could be supercooled anywhere from 18 to over 30% below their liquidus temperatures. As outlined in Frank's 1952 paper, the original belief that metals could not be supercooled emerged from ideas that the structures within the metallic liquid must look very similar to their crystalline structures [17]. Hence, a small nucleation barrier separated the two phases, making crystallization of the liquid easy. Frank argued that this interpretation must be wrong, given the observations of Turnbull and Cech. Frank wrote:

> “Consider the question: ‘In how many different ways can one put twelve billiard balls in simultaneous contact with one, counting as different the arrangements which cannot be transformed into each other without breaking contact with the centre ball?’ The answer is *three*. Two which come to the mind of any crystallographer occur in the face-centred cubic and hexagonal close-packed lattices. The third comes to the mind of any good schoolboy, and it is to put one at the center of each face of a regular dodecahedron. That body has five-fold axes, which are abhorrent to crystal symmetry…this one cannot be continuously extended in three dimensions…I infer that this will be a very common grouping in liquids.” [17]

As icosahedral order does not fill three-dimensional space completely, it must be rearranged into a different order to satisfy crystal periodicity conditions, which could give rise to the large supercooling observed by Turnbull and Cech [14]. There are no such requirements for long range order in liquids; therefore, short and medium range icosahedral order could be possible in liquids. While Frank’s hypothesis is somewhat dated now, given that the 2011 Nobel Prize was awarded to Dan Shechtman for the discovery of quasicrystals (regularly ordered crystals without long-range periodicity, such as icosahedrally ordered Al-Mn), [18] it still works in the case of the formation of periodic crystal phases from supercooled metallic liquids. Frank’s hypothesis did not have experimental verification until 2003, when Kelton *et. al.* observed strong icosahedral order in supercooled liquid $Ti_{39.5}Zr_{39.5}Ni_{21}$, which crystallized to a metastable icosahedral quasicrystal instead of the predicted stable C-14 polytetrahedral Laves phase [19].

1.2 Classical Theory of Nucleation (CNT)

The Classical Theory of Nucleation is one of the most common theories used to understand nucleation and the nucleation barrier. The following section will detail the theory’s development by Volmer and Weber [11] and Becker and Döring [12].

1.2.1 Volmer Weber Treatment

Before delving into the kinetic treatment of nucleation, it is informative to first examine the case of condensation of droplets from a vapor. The following derivation is reproduced from [8,20]. Following the statistical arguments of Gibbs [21], the probability of a fluctuation producing a nuclei of size *n*, P_n, is proportional to a Boltzmann distribution:

$$P_n \propto \exp\left(-\frac{W(n)}{k_B T}\right) \tag{1.1}$$

where $W(n)$ is the reversible work of cluster formation for a cluster of size *n*, k_B is Boltzmann's constant, and *T* is the temperature. Thus, the equilibrium cluster distribution per mole, $N^{eq}(n)$, is:

$$N^{eq}(n) = N_A \exp\left(-\frac{W(n)}{k_B T}\right) \tag{1.2}$$

where N_A is Avogadro's number.

Assuming that, at constant pressure, spherical clusters with the same composition as the original phase are formed by these fluctuations, the reversible work of cluster formation of a cluster containing *n* atoms is:

$$W(n) = n\Delta\mu + (36\pi)^{1/3}\bar{v}^{2/3}n^{2/3}\sigma \tag{1.3}$$

where $\bar{v}$ is the molecular volume and the form of the second term is acquired by expressing the surface free energy $(4\pi r^2\sigma)$ in terms of the number of clusters using $n\bar{v} = (4/3)\pi r^3$. Inherent in this equation is the assumption of an isotropic interfacial free energy σ, which will be discussed in the following sections. The first term in Eq. 1.3 is a volume term that represents the "strength" of the thermodynamic driving free energy, while the second is a surface term and represents an energy penalty for creating an interface in the parent phase. When the phase transition is favored, such as at temperatures below the equilibrium liquidus temperature in the case of metallic alloys, the first term is negative. The surface term will always be positive, as there is always a penalty associated with forming an interface between the liquid and crystal phases. A schematic representation of Eq. 1.3 is produced below in Fig. 1.2, reproduced with permission from Elsevier from [8]. The maximum work of cluster formation can be found by solving $dW(n)/dn = 0$, giving:

$$W(n^*) = \frac{16\pi}{3}\frac{\sigma^3}{(\Delta g)^2} \tag{1.4}$$

where Δg is the Gibbs free energy difference per unit volume ($\Delta g = \Delta\mu/\bar{v}$) and n^* corresponds to the critical cluster size given by:

$$n^* = \frac{32\pi}{3\bar{v}}\frac{\sigma^3}{|\Delta g|^3} \tag{1.5}$$

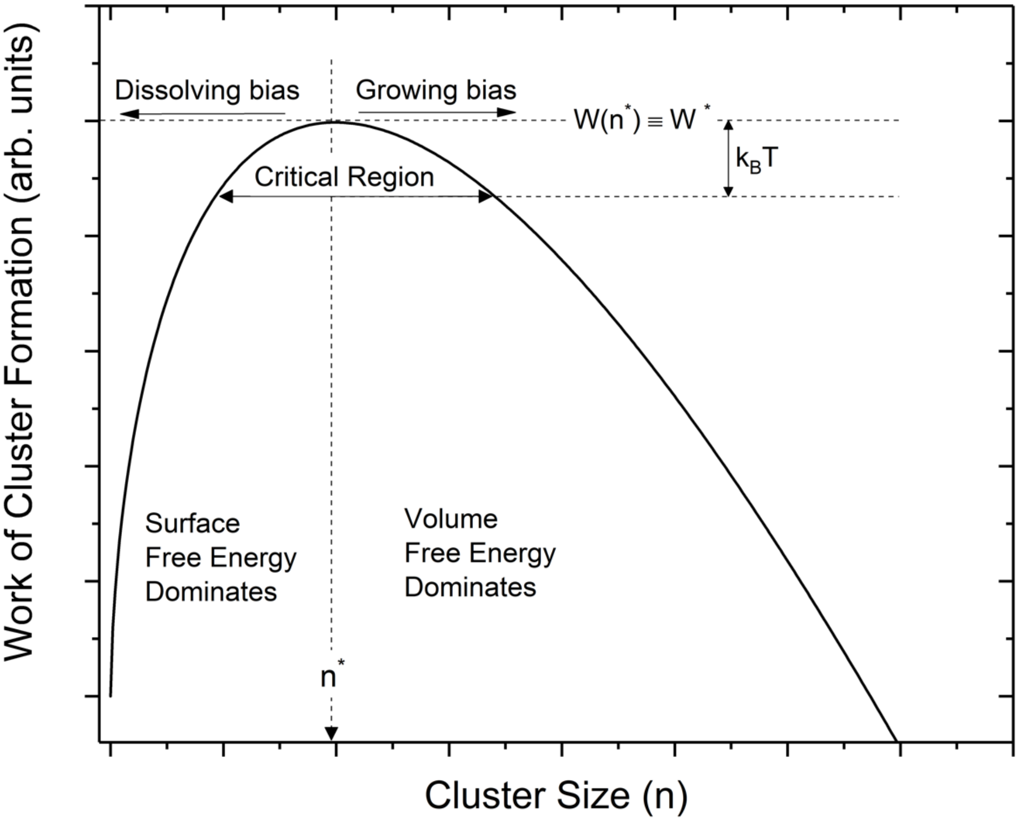

Figure 1.2: A schematic representation of Eq. 1.3. Note that there exists a maximum in the work of cluster formation, indicated by W^*, which occurs at the critical cluster size n^*. In metallic systems, n^* is usually 400-800 particles. Reproduced from [8] with permission from Elsevier.

If the cluster exists to the left of n^*, then it is stochastically biased towards dissolving back into the parent phase, as the surface free energy penalty exceeds the driving volume free energy. Consequently, clusters to the right of n^* are stochastically biased towards growth, as the volume free energy dominates the surface energy penalty. As this is a stochastic process, it is possible for a cluster to exist either on the left or right of n^* but experience the opposing effect. Near the critical size, thermal fluctuations of order k_BT are responsible for either growing or dissolving a cluster.

The work of cluster formation can also be expressed in terms of the cluster radius, which more clearly shows the competition between the volume and surface free energy contributions. For a spherical cluster, the work of cluster formation in terms of cluster radius is:

$$W(r) = \frac{4\pi}{3}r^3\Delta g + 4\pi r^2\sigma \tag{1.6}$$

As seen in Fig. 1.3, the volume free energy is negative when below the liquidus temperature and, for clusters much smaller than the critical radius $r^* = 2\sigma/|\Delta g|$, the surface free energy will dominate and inhibit cluster formation.

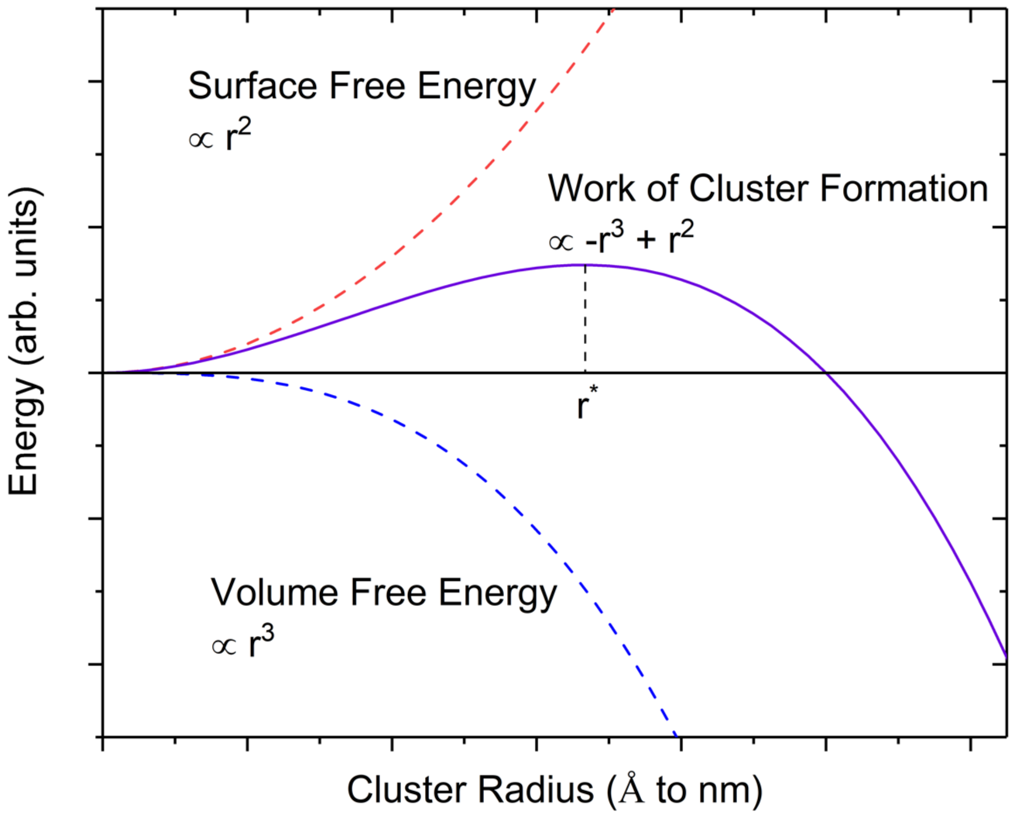

Figure 1.3: The work of cluster formation from Eq. 1.6, with the volume and surface free energy contributions shown with dashed lines. The critical cluster radius is shown as r^*. The units of cluster radius typically range from Å to nm, with metallic systems having r^* around 1.0-1.5 nm.

The kinetic model proposed by Volmer and Weber [11] assumes that nuclei, instead of forming all at once from one large fluctuation, grow or shrink slowly by the addition or loss of single particles. The reaction describing this process is:

$$E_{n-1} + E_1 \underset{k^-(n)}{\overset{k^+(n-1)}{\rightleftarrows}} E_n$$

$$E_n + E_1 \underset{k^-(n+1)}{\overset{k^+(n)}{\rightleftarrows}} E_{n+1} \qquad (1.7)$$

where $k^+(n)$ is the attachment rate of a particle to a cluster of size n and $k^-(n)$ is the loss rate. The time-dependent cluster size distribution $N(n,t)$ can be determined by solving a system of coupled differential equations of the form:

$$\frac{\partial N(n,t)}{\partial t} = N(n-1,t)k^+(n-1) - N(n,t)\big(k^+(n) + k^-(n)\big) + N(n+1,t)k^-(n+1) \qquad (1.8)$$

which has the form of a master equation. The time-dependent flux of clusters past a cluster of size n—also known as the nucleation rate, $I(n,t)$—is given by:

$$I(n,t) = N(n,t)k^+(n) - N(n+1,t)k^-(n+1) \qquad (1.9)$$

The evolution of the cluster distribution thus takes a “stair-step” appearance due to the decrease in the cluster size distribution. This is schematically represented in Fig. 1.4. As will be discussed with other models, the classical theory assumes that nucleation kinetics are controlled primarily by interfacial effects, with the extra assumption of a sharp interface between the cluster and the parent phase. A cluster size of 10 was taken as the lower limit distinguisher between clusters and the equilibrium liquid, which can be justified by considering the close-packed structure of many crystalline structures [22].

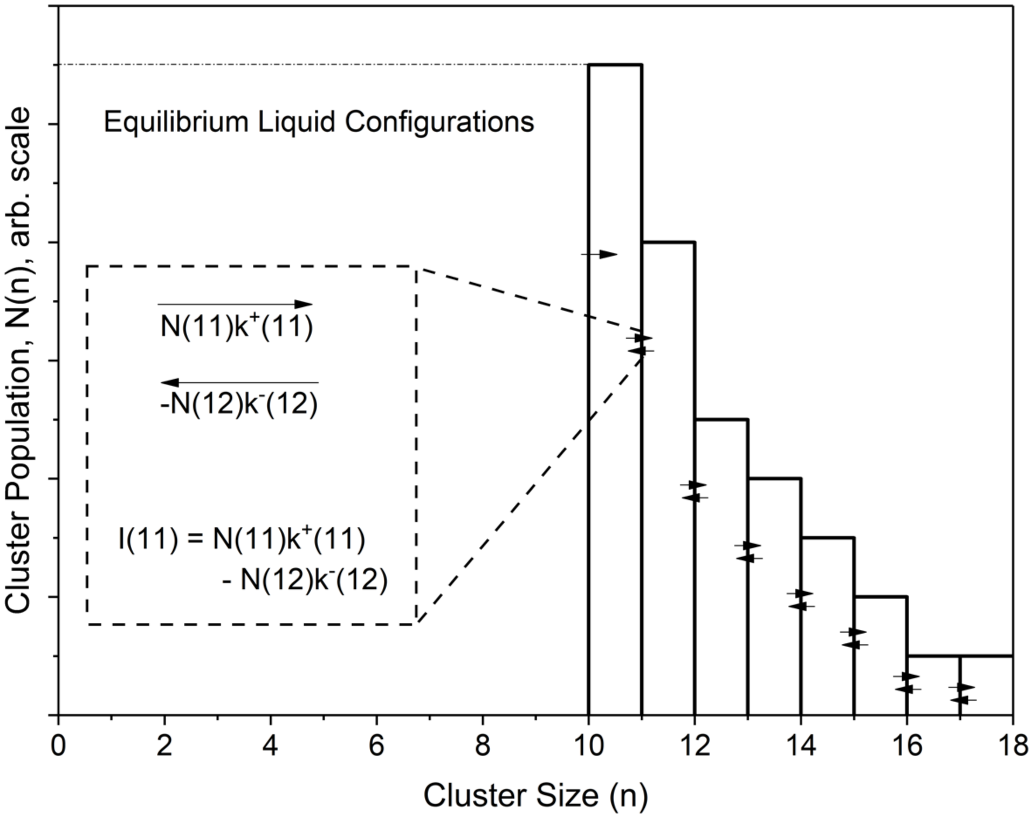

Figure 1.4: A schematic histogram of cluster population at a given cluster size *n*. Below some limit, it is impossible to distinguish clusters from the equilibrium fluctuations in the liquid. Reproduced from [20] with permission from Elsevier.

In their derivation, Volmer and Weber assumed an equilibrium distribution of clusters and that clusters larger than n^* will quickly grow and leave the distribution. For clusters smaller than n^*, the distribution of cluster sizes is set equal to the equilibrium distribution from Eq. 1.2. Therefore, using Eq. 1.9, it is possible to write the Volmer-Weber nucleation rate, I^{VW}, from these assumptions as:

$$I^{VW} = N^{eq}(n^*)k^+(n^*) = k^+(n^*)N_A \exp\left(-\frac{W(n^*)}{k_B T}\right) \tag{1.10}$$

While Eq. 1.10 captures several key features about nucleation, the assumption of an equilibrium distribution is inherently flawed. The equilibrium distribution assumed by Volmer and Weber predicts an unphysical divergence for cluster sizes much larger than n^*. As will be seen in the next section, a steady-state distribution is the correct assumption for the behavior of clusters. Further discussion of the consequences of assuming an equilibrium distribution may be found elsewhere [8].

1.2.2 Becker Döring Treatment

Becker and Döring [12] derived an expression for the steady-state nucleation rate; their derivation is reproduced below. A steady-state nucleation rate, I^{ST}, must be derived from the steady-state distribution of clusters, N^{ST}:

$$I^{ST} = N^{ST}(n)k^{+}(n) - N^{ST}(n+1)k^{-}(n+1) \tag{1.11}$$

To satisfy steady-state conditions, I^{ST} must be independent of time and give the same rate for every cluster size. The rates must also be computed. If there is no net cluster flux, whereby a nucleation rate of zero is obtained for all cluster sizes, the rates can be written in terms of the equilibrium distribution:

$$N^{eq}(n+1)k^{-}(n+1) = k^{+}(n)N^{eq}(n) \tag{1.12}$$

Equation 1.12 can be solved for the backwards nucleation rate, which allows for Eq. 1.11 to be re-written as:

$$I^{ST} = N^{eq}(n)k^{+}(n)\left[\frac{N^{ST}(n)}{N^{eq}(n)} - \frac{N^{ST}(n+1)}{N^{eq}(n+1)}\right] \tag{1.13}$$

The boundary conditions for Eq. 1.13 are as follows:

$$\begin{gathered} n \to 0, N^{ST}(n) \to N^{eq}(n) \\ and \\ n \to \infty, N^{ST}(n) \to 0 \end{gathered} \tag{1.14}$$

As mentioned elsewhere [20], the solution does not depend strongly on these boundary conditions as long as the energies corresponding to the given cluster sizes are at least k_BT lower than W^*, as represented earlier in Fig. 1.2. In practice, values for n are chosen to approximate the limits stated in Eq. 1.14 such that for $n \leq i, N^{ST}(n) = N^{eq}(n)$ and for $n \geq j, N^{ST}(n) = 0$. By dividing $N^{eq}(n)k^+(n)$ over to the left in Eq. 1.13, summing over all values of n between i and j, and applying the boundary conditions in Eq. 1.14:

$$I^{ST}\sum_{n=i}^{j}\frac{1}{N^{eq}(n)k^+(n)} = \sum_{n=i}^{j}\left(\frac{N^{ST}(n)}{N^{eq}(n)} - \frac{N^{ST}(n+1)}{N^{eq}(n+1)}\right) = \frac{N^{ST}(i)}{N^{eq}(i)} - \frac{N^{ST}(j+1)}{N^{eq}(j+1)} = 1 \tag{1.15}$$

The steady-state nucleation rate can be obtained from Eq. 1.15 by following several assumptions given in both [8] and [20]. For completeness, the assumptions are briefly outlined here. First, terms near n^* dominate the sum, as seen in the maximum in Fig. 1.2. Second, $k^+(n)$ is replaced with $k^+(n^*)$, as the dependence of the rate on the cluster size for large clusters is small, as seen in Fig. 1.3. Third, W^* is expanded in a Taylor series around n^* and the first two nonzero terms are used. Fourth, N^{eq} is taken to be a continuous function of n, allowing for the sum in Eq. 1.15 to be replaced by an integral extended from $-\infty$ to ∞, due to the strong peak at n^*. Finally, given Eq. 1.15, I^{ST} is equal to the inverse of the sum of $1/N^{eq}$. Following all of these approximations and defining $\xi = n - n^*$ from the Taylor Series expansion gives:

$$\sum_{n=i}^{j}\frac{1}{N^{eq}(n)} = \frac{1}{N_A}\exp\left(\frac{W(n^*)}{k_BT}\right)\int_{-\infty}^{\infty} d\xi \, \exp\left(-\frac{\xi^2 W(n^*)}{3k_BT(n^*)^2}\right) \tag{1.16}$$

The integral in Eq. 1.16 is in the form of an error integral, with a solution of:

$$\sum_{n=i}^{j} \frac{1}{N^{eq}(n)} \cong \frac{1}{N_A} \exp\left(\frac{W(n^*)}{k_B T}\right) \left(\frac{3\pi k_B T}{W(n^*)}\right)^{1/2} n^* \tag{1.17}$$

Thus, the steady-state homogeneous nucleation rate equation for spherical clusters is:

$$I^{ST} = N^{eq}(n^*) k^+(n^*) Z \tag{1.18}$$

where Z is the Zeldovich factor, typically 0.01 to 0.1 in value, defined as:

$$Z = \left(\frac{|\Delta\mu|}{6\pi k_B T n^*}\right)^{\frac{1}{2}} \tag{1.19}$$

In the Becker-Döring treatment, the steady-state nucleation rate in Eq. 1.18 is of the same form as the Volmer-Weber nucleation rate in Eq. 1.10, except for the additional Zeldovich factor. Numerical computations have shown that the nucleation rate calculated from the Volmer-Weber treatment is larger than the rate calculated from the Becker-Döring treatment [8]. From Zeldovich [23] and Frenkel [24], the forward and backward rates may be defined as:

$$k^+ = 4n^{2/3}\gamma \exp(-\delta W(n)/2k_B T) \tag{1.20a}$$

$$k^- = 4(n-1)^{2/3}\gamma \exp(+\delta W(n-1)/2k_B T) \tag{1.20b}$$

where $\delta W(n)$ is the difference in the work of cluster formation between a cluster of size $n+1$ and n and γ is the molecular jump frequency at the interface. In practice, γ is usually assumed to be the same as the jump frequency for bulk diffusion, D, which gives: $\gamma = 6D/\lambda^2$, where λ is the atomic jump distance, typically on the order of an angstrom [13]. Putting the pieces together gives the steady-state nucleation rate equation in a condensed system as:

$$I^{ST} = \frac{24DN_A(n^*)^{2/3}}{\lambda^2}\left(\frac{\Delta\mu}{6\pi k_B T n^*}\right)^{1/2} \exp\left(-\frac{W^*}{k_B T}\right) = A^* \exp\left(-\frac{W^*}{k_B T}\right) \tag{1.21}$$

The Stokes-Einstein diffusion coefficient is typically assumed in Eq. 1.21: $D = k_B T / 6\pi a\eta$, where η is the viscosity and a is a typical atomic distance on the order of an angstrom. All of the terms before the exponential are commonly represented by a single pre-factor term A^*. The classical theory can also be expanded to look at time-dependent nucleation, as was derived by Kashchiev [25]. Time-dependent nucleation can be important slow nucleation processes, like the crystallization of silicon-oxide glasses, but is not necessary for the quickly crystallizing metallic liquids studied here. More detail on this can be found elsewhere [20,25].

In addition, $\Delta\mu$ is typically approximated using several different forms, outlined elsewhere [20]. In this thesis, the two approximations used for $\Delta\mu$ are the Turnbull approximation and the Spaepen-Thompson approximation. The Turnbull Approximation is defined as:

$$\Delta G = \frac{\Delta H_f \Delta T}{T_l} \tag{1.22}$$

where ΔH_f is the enthalpy of fusion, $\Delta T = T_l - T_u$ is the supercooling, T_l is the liquidus temperature, and T_u is the maximum achieved supercooling temperature. ΔG is converted to $\Delta\mu$ by normalizing by N_A. Turnbull argued that this approximation should be used if no data on ΔC_p, the specific heat, exist [16]. In practice, this is a reasonable approximation for most metals because the difference in specific heat between liquid and crystal faces is approximately zero. The Spaepen-Thompson approximation is a slight extension of the Turnbull approximation, with the specific heat is now set equal to the entropy of fusion ΔS_f [26], giving:

$$\Delta G = \frac{\Delta H_f \Delta T}{T_l} \frac{2T}{T_l + T} \tag{1.23}$$

1.3 Moving Beyond the Classical Theory

The Classical Theory of Nucleation (CNT) is arguably the most popular theory used to describe nucleation phenomena. It has been applied to several different types of systems, from metallic liquids and solids, to vapor condensation, to silicate glasses and beyond. Within the classical theory are a few simplifying approximations, the most notorious of which is capillarity approximation. By invoking capillarity, the theory assumes a sharp interface between the cluster and parent phase. The CNT uses bulk thermophysical properties to discuss physics occurring at the atomic and molecular level, since the clusters can sometimes contain only tens of atoms. Additionally, the impact of the structures of the initial and final phases on nucleation are completely disregarded. Finally, CNT is inherently an interface-limited kinetics theory and does not take proper account of long-range diffusion in nucleation.

As discussed elsewhere [20], the use of the CNT has resulted in measured pre-factors being anywhere from 7 to 25 orders of magnitude larger than predicted. For the experimental values to agree with theoretical predictions, σ must increase linearly with temperature, which is opposite of the behavior expected for a free energy. At the time, Turnbull [27] and Spaepen *et. al.*[28,29] argued that the positive linear temperature dependence must be due to ordering near the interface of the cluster. As will be discussed in the next section, the Diffuse Interface Theory provides an explanation for such an observed effect in the Classical Theory.

1.3.1 Diffuse Interface Theory of Nucleation

Spaepen [30] and Gránásy [31,32] independently proposed a phenomenological thermodynamic approach to nucleation. Gránásy wrote that:

> “computer simulations [33] and microscopic models [34] imply that nuclei are nearly ‘all interface’; thus, the ‘capillarity’ approximation, i.e., the assumption that the thickness of the interface region is small compared with the size of nuclei, is probably responsible for the failure of the CNT.” [31]

The discussion on the Diffuse Interface Theory (DIT) below follows the Gránásy treatment [31]. Gránásy assumed that clusters had spherical symmetry and that “bulk properties prevail *at least* at the center” [31] of the cluster. Gránásy assumes that the enthalpy and entropy are smooth functions of distance that change from one phase to the other (so called “cross-interfacial enthalpy and entropy distributions”, see Fig.1.5, reproduced from [31] with permission from Elsevier). Thus, the work of cluster formation can be written as:

$$W = \int_0^\infty (\Delta h - T\Delta s) 4\pi r^2 dr \tag{1.24}$$

where $\Delta h = N(r)[H(r) - H_1], \Delta s = N(r)[S(r) - S_1]$, $N(r)$ is the local number density of molecules, $H(r)$ and $S(r)$ are the local enthalpy and entropy per molecule, and the subscript “1” indicates the parent phase. By replacing Δh and Δs with the respective “rectangularized” distributions $\Delta h_{eff} = \Delta h_0[1 - \theta(r - R_H)]$ and $\Delta s_{eff} = \Delta s_0[1 - \theta(r - R_S)]$, where θ is the step function, Δh_0 and Δs_0 are the enthalpy and entropy differences between the parent and new phase, and R_H and R_S are the locations of the enthalpy and entropy surfaces locations allows Eq. 1.21 to be re-written as a simple difference between the enthalpy and entropy surfaces:

$$W = \kappa(R_H^3 \Delta h_0 - R_S^3 T \Delta s_0) \tag{1.25}$$

In Eq. 1.25, $\kappa = 4\pi/3$. Gránásy, citing Turnbull [27], claims that the area enclosed by the enthalpy and entropy curves is proportional to the interfacial free energy and that, for a positive interfacial free energy, the enthalpy curve must lie higher than the entropy curve. This is represented schematically in Fig. 1.5, which has been reproduced from [31] with permission from Elsevier.

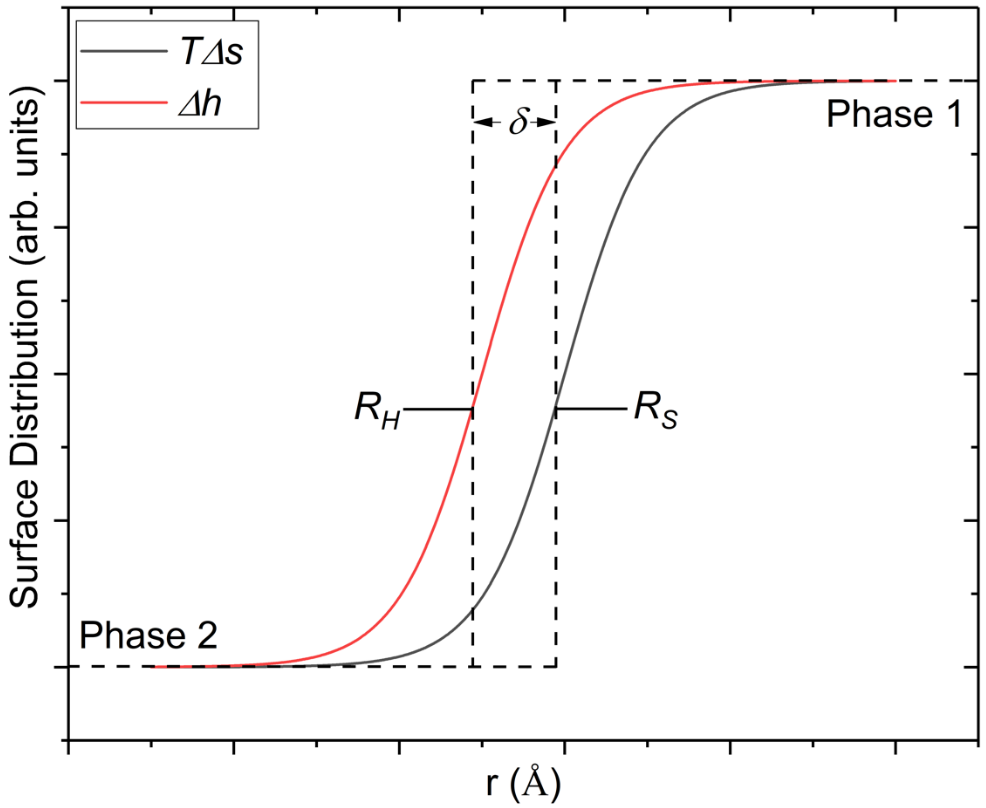

Figure 1.5: A schematic representation of the enthalpy and entropy surfaces between two phases in the Diffuse Interface Theory. The dashed lines represent the "rectangularized" distributions for both surfaces. This figure represents equilibrium distributions, further detail for non-equilibrium distributions may be found elsewhere [31] Reprinted with permission from Elsevier.

As noted by Gránásy, δ may be significantly smaller than that the interfacial thickness. For clusters significantly larger than δ, Gránásy postulates $R_S - R_H = \delta$. From there, R_H may be expressed in terms of δ and R_S and Eq. 1.25 can be maximized with respect to R_S, ultimately yielding an expression for the critical work of cluster formation:

$$W^* = -\kappa\delta^3\Delta g_0\psi(\eta) \tag{1.26}$$

where $\Delta g_0 = \Delta h_0 - T\Delta s_0$, $\psi(\eta) = 2(1+q)\eta^{-3} - (3+2q)\eta^{-2} + \eta^{-1}$, $q = (1-\eta)^{-1/2}$, and $\eta = \Delta g_0/\Delta h_0$. Finally, Gránásy follows a similar kinetic approach as outlined earlier [20] to arrive at the same functional form of the steady-state nucleation rate defined in Eq. 1.19: $I^{ST} = A^* \exp(-W^*/k_B T)$. As the functional form of the steady-state nucleation rate in DIT is the same as CNT, it can be used in the probability density curve fits outlined in later sections.

As mentioned earlier, to fit experimental data, the CNT would predict a positive temperature dependence in the interfacial free energy. As shown in more detail elsewhere [8], the temperature dependence of σ can be approximated with DIT parameters:

$$\frac{d\sigma}{dT} \approx \delta\left(\left(s_{liquid} - s_{interface}\right) - \frac{\Delta s_f}{2}\right) \tag{1.27}$$

where s_{liquid} and $s_{interface}$ are the entropies of the liquid and interface, respectively, and Δs_f is the entropy of fusion. As mentioned earlier, the positive temperature dependence in the interfacial free energy was thought to be associated with ordering at the interface. From Eq. 1.27, this requires $s_{interface} < s_{liquid} - \frac{\Delta s_f}{2}$. Since $s_{interface}$ is smaller, it demonstrates that order must be occurring at the cluster interface. The DIT extends the thermodynamic considerations in the CNT, but assumes the same kinetics. So like the CNT, it cannot model the cases when diffusion is dominant in nucleation. One approach for this case is explained in the next section.

1.3.2 Coupled Flux Theory of Nucleation

In general, the classical theory of nucleation applies to cases where the diffusion rates are sufficiently fast that the rate-limiting step is interfacial attachment of atoms or molecules onto the cluster. Because the classical theory of nucleation is inherently interface-limited, it may fail to fully describe nucleation that relies on slow, long-range diffusion effects, such as solid precipitation or nucleation in quiescent liquids. For example, the classical theory was found to be inconsistent with its description of oxygen precipitation in single crystal silicon, requiring an extension of the classical theory to match the data with theoretical predictions [35–37]. In most cases, it is standard to analyze data assuming a steady-state nucleation rate; however, as shown in these references, time-dependent nucleation can also be important for diffusion limited nucleation.

To more fully explore the impact of long-range diffusion on nucleation, a new theory that couples interface and diffusion effects has been proposed [38–40]. This theory, known as the "Coupled-Flux" theory, broadens the scope of the classical theory by considering both interfacial cluster attachment rates and diffusion rates around the neighborhood of the cluster. This is represented in Fig 1.6, reproduced with permission from Elsevier from [38].

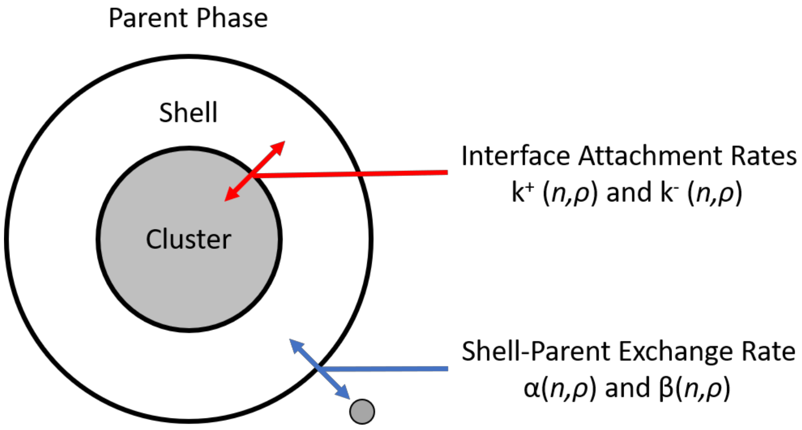

Figure 1.6: A schematic illustration of the Coupled-Flux model for nucleation, showing the interfacial attachment rates in red, the shell-parent exchange rates in blue, and the location of the cluster, shell, and parent phase. Reproduced with permission from Elsevier from [38].

The following derivation is a brief summary from the presentation in [38,39]. In the classical theory, nucleation is described with bimolecular reactions at each cluster size. However, the CNT does not consider changes in composition around the newly formed nuclei. In most cases, the nuclei and parent phase do not have the same composition, resulting in size and compositional effects on the driving free energy. Therefore, the dynamic changes of cluster and parent phase composition must be considered to fully address this problem. However, such a problem is currently intractable. The simplified model for this problem is to consider three regions—the nuclei, the parent phase, and a shell of the original phase between these two. The shell approximates the change in local composition around the cluster by a set of discrete jumps between the parent phase and shell. For the Coupled-Flux theory, the equilibrium cluster distribution has the form:

$$N(n,\rho) = N_0 \exp\left(\frac{W_n}{k_B T}\right) P\{\rho\} \tag{1.28}$$

where N_0 is the number of solute atoms per unit volume in the initial phase, W_n is the work of cluster formation, and $P\{\rho\}$ is the probability of having ρ solute atoms in the nearest neighbor shell around the cluster. As a simplifying approximation, the work of cluster formation is taken to be the same as the classical theory, defined earlier in Eq. 1.3. $P\{\rho\}$ is calculated from the difference in entropy for an atom randomly located either in the original phase or in the nearest-neighbor shell. The derivation of $P\{\rho\}$ is discussed in more detail elsewhere [38]. As $P\{\rho\}$ is dependent on entropy configurations, it has the form of the number of available microstates and Eq. 1.28 can be re-written as:

$$N(n,\rho) = \alpha_n N_0 \exp\left(\frac{W_n}{k_B T}\right) \frac{\rho_n^m!}{\rho!\,(p_n^m! - \rho)!} \left(\frac{N_0}{N_s - N_0}\right)^{\rho} \tag{1.29}$$

where α_n is a normalization constant determined for each n from the condition $\sum_{\rho=0}^{\rho_m} P\{\rho\} = 1$, ρ_n^m is the maximum number of atom sites in the nearest-neighbor shell of a cluster of n atoms, N_0 is the number of atoms, and N_s are the number of sites (and N_0/N_s is the atom fraction).

For a cluster of size n with ρ particles in the cluster neighborhood, there will be several governing rates describing cluster formation and growth, as represented in the figure below, reproduced from [38] with permission from Elsevier. From the figure, $\alpha(n,\rho)$ and $\beta(n,\rho)$ are the forward and backward diffusion rates for solute atoms into or out of the shell, while k^+ and k^- are the forward and backward attachment rates for particles onto the cluster. For all rates, an extra dependence on ρ is included to account for the depletion of particles from the shell.

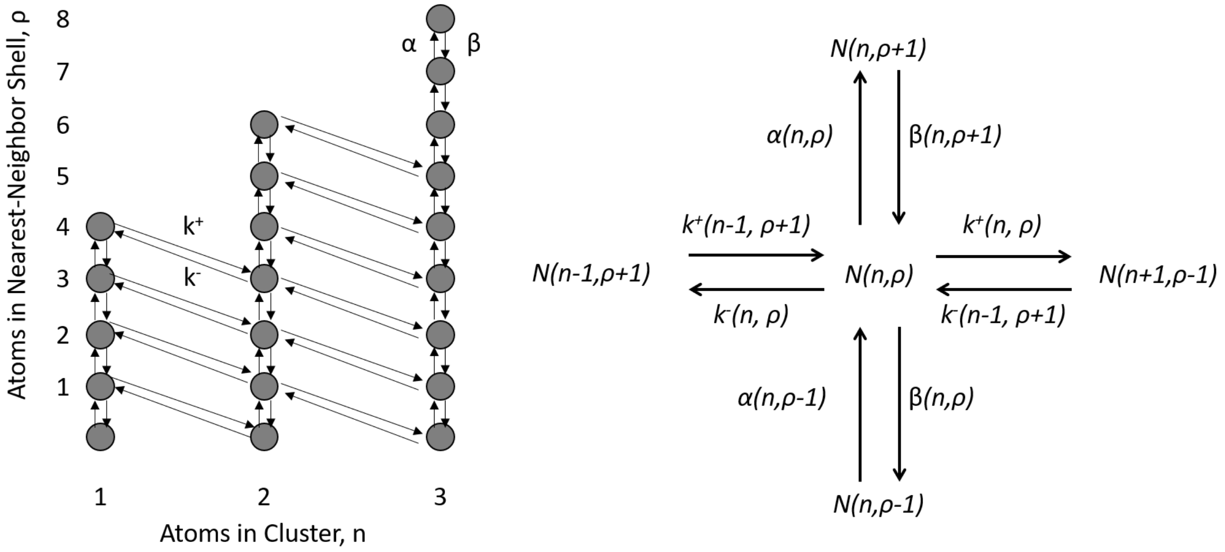

Figure 1.7: (Left) A schematic of the rates and growth of clusters when interfacial and diffusion rates are important. (Right) The set of fluxes describing the growth of a cluster and the exchange of particles within the shell. Reproduced with permission from Elsevier from [38].

Like for the classical theory, the Coupled-Flux theory is governed by a general master equation of the form:

$$\frac{\partial N(n,\rho,t)}{\partial t} = \alpha(n,\rho-1)N(n,\rho-1,t) - [\alpha(n,\rho)+\beta(n,\rho)]N(n,\rho,t)$$

$$+\beta(n,\rho+1)N(n,\rho+1,t) + k^{+}(n-1,\rho+1)N(n-1,\rho+1,t) +$$

$$k^{-}(n+1,\rho-1)N(n+1,\rho-1,t) - [k^{+}(n,\rho)+k^{-}(n,\rho)]N(n,\rho,t) \tag{1.30}$$

In a similar fashion to the CNT, the rates may be computed by assuming a net-zero flux between the shell and parent phase, giving:

$$N(n,\rho-1)\alpha(n,\rho-1) = N(n,\rho)\beta(n,\rho) \tag{1.31}$$

Equation 1.31 can then be used to calculate the rates for α and β by using Eq. 1.29:

$$\alpha(n,\rho-1) = \xi\rho\frac{D}{\lambda^2}\left(\frac{\rho_n^m-\rho+1}{\rho}\right)^{1/2}\left(\frac{N_0}{N_s-N_0}\right)^{1/2} \tag{1.32a}$$

$$\beta(n,\rho) = \xi\rho\frac{D}{\lambda^2}\left(\frac{\rho_n^m-\rho+1}{\rho}\right)^{1/2}\left(\frac{N_0}{N_s-N_0}\right)^{1/2} \tag{1.32b}$$

Here, $\rho D/\lambda^2$ is proportional to the rate at which a particle leaves the shell and returns to the parent phase, with D being the diffusion coefficient in the parent phase and λ is the jump distance. ξ is a constant accounting for particles not immediately equilibrating with the parent phase after leaving the shell. It will become very small in the limit of a highly dilute solute. Repeating this process for the k^+ and k^- rates yields:

$$k^{+}(n,\rho) = \rho\frac{6D'}{\lambda^2}\exp\left(-\frac{\delta W_n}{2k_BT}\right)G(n,\rho) \tag{1.33a}$$

$$k^{-}(n+1,\rho-1) = \rho\frac{6D'}{\lambda^2}\exp\left(\frac{\delta W_n}{2k_BT}\right)\left(\frac{1}{G(n,\rho)}\right) \tag{1.33b}$$

Here, *D'* reflects the mobility at the interface and *G(n,ρ)* is a correction factor accounting for entropy changes in the shell and parent phase as particles attach to the cluster. The full form of *G(n,ρ)* is outlined elsewhere [38]. Just like the DIT, the Coupled-Flux theory has a steady-state nucleation rate of the form: $I^{ST} = A^{*} \exp\left(-\frac{W^{*}}{k_B T}\right)$ [8].

Numerical solutions for the Coupled-Flux model are challenging with approaches like Runge-Kutta, as the differential equations are stiff. Implicit methods [41] can solve the problem and estimate the associated time-dependent rates. Earlier, Russell proposed an analytical solution to a problem of this type by first introducing the concept of coupled (or linked) flux [40], arguing that the steady-state nucleation rate in the Coupled-Flux theory could be expressed as the steady-state nucleation rate from CNT multiplied by a scaling factor proportional to β, k^{+}, and the concentration. Kelton's approach eliminated many of Russel's approximations [38] and found that scaling the classical theory by the ratio of $\alpha(n^{*},0)/k^{+}(n^{*},1)$ resulted in better agreement with Coupled-Flux theory predictions.

As in the time-dependent nucleation case discussed earlier in this section, the Coupled-Flux theory provides an explanation for the difference in composition around the cluster. In general, clusters that are smaller than the critical size are biased towards dissolving [20]. For precipitation, this results in a local composition that can be higher in the species nucleating than the parent phase. Clusters larger than the critical size are biased towards growth, which (for precipitation) reduces the concentration of the species nucleating in the neighborhood of the nucleating cluster. These two cases can be understood within the framework of the coupled flux theory. In diffusion-limited systems, the processes in the coupled flux model can significantly slow down the nucleation and growth of a new phase. In cases where diffusion is not the rate limiting step, such as in highly stirred liquids or where diffusion in the parent phase is fast, the Coupled-Flux theory recovers the predictions of the classical theory.

Studies on the International Space Station (ISS) were proposed to “measure, in the absence of gravitationally-induced flow, the effects of alloy composition on nucleation and to compare with predictions from the Coupled-Flux model for nucleation [42].” With ground-based ESL measurements of liquids, gravitational and Marangoni-induced convection are the two primary contributors to stirring [42–44]. Since samples in the ESL are usually heated with a single axial laser, large thermal gradients within the liquid will be generated due to the sample’s finite thermal conductivity. In practice, these gradients can be reduced by a tetrahedral arrangement of heating lasers to more uniformly heat samples [45]; however, this is beyond the scope of this chapter. Regardless, the calculated flow velocity of gravitational and Marangoni convection were found to be a factor of two larger than the maximum diffusion flow velocity [42]. To study these diffusion effects, gravitational and Marangoni convection must be reduced.

In ground-based EML studies, stirring due to the electromagnetic force is introduced, in addition to the already existing Marangoni and gravitational contributions [44]. However, since samples are more uniformly heated in EML, the overall impact of Marangoni convection is reduced. Processing samples in microgravity environments also further reduces the impact of gravitational stirring. More importantly, microgravity conditions mean less force must be applied to the sample to heat and position it, further reducing the stirring contributions of Marangoni and electromagnetic convection. Models of liquids in the EML have shown that the calculated flow velocity from stirring can be upwards of two orders of magnitude smaller than the predicted diffusion flow velocity [42]. As such, if diffusion effects are important in nucleation, they should be observable within the EML.

1.4 Containerless processing

Since the focus of this dissertation is the study of crystal nucleation in metallic liquids, the question of a container must be addressed. To study homogeneous nucleation in metallic liquids, a large supercooling must be achieved. Most metallic liquids have high melting temperatures, ranging from approximately 550 °C to upwards of 1900 °C and beyond. This poses several issues, as liquid metals are highly reactive and likely to alloy with a metallic container. Even if an inert crucible were used, there would still be several issues: (1) liquid metals react strongly with oxygen at high temperatures, leading to the formation of oxide layers; (2) containers contribute to the scattering intensity in diffraction experiments, which will interfere with any scattering signal from the sample; (3) containers introduce heterogeneous nucleation sites for the sample, such as microscopic cracks in the container wall, drastically limiting its supercooling ability. To study metallic liquids, containerless processing techniques have been developed. This section will briefly outline several of the possible techniques and the next chapter will discuss two of these in more detail, i.e.Electrostatic Levitation (ESL) and Electromagnetic Levitation (EML), since they were the techniques used for these studies discussed in this thesis. Further detail on all of the following techniques may also be found elsewhere [8,46,47].

Acoustic levitation [48] uses focused sound plane waves, typically in the ultrasonic regime (> 20,000 Hz) to levitate samples. Since ultrasound is used, an elastic medium must be present to support ultrasonic wave propagation. Typically, this is an inert, pressurized atmosphere of high purity gas like nitrogen or argon. However, acoustic levitation is an aggressive processing technique, requiring high radiation force to levitate dense samples and likely leading to their deformation and fragmentation, especially when melted [8]. It also has generally poor positioning control, possibly leading to sample instability. Despite that, acoustic levitation can enable the processing of lower density, non-conductive samples.

Aerodynamic and aero-acoustic [49] levitation techniques use gas flow through several nozzles to both levitate and position the sample, enabling the study of metallic, semiconducting, and nonconducting materials. In aero-acoustic levitation, ultrasound is also used to help levitate the sample, as mentioned earlier. The sample is usually heated via a high-intensity laser, which enables the melting of metallic samples and the study of their liquid phases. However, since gas is used as the levitation engine, any contaminants present in the gas are likely to be introduced to the sample. This can lead to the formation of oxide layers on reactive samples. In addition, high levels of gas flow will generate large thermal gradients in the sample. The aero-acoustic method has been shown to be useful for nonconductive and inert materials like ceramics.

Electromagnetic Levitation (EML) induces eddy currents in the sample via high-frequency electromagnetic fields [50]. The eddy currents, in addition to resistively heating the sample, also levitate it via Lenz's law. Ground-based EML studies must apply a high-intensity electromagnetic field to the sample to overcome Earth's gravitational field. For some low melting point samples, this either limits or completely blocks the supercooled liquid from being studied. A high purity cooling gas may be used to cool the sample below its liquidus temperature, but this may also introduce contamination into the sample. In microgravity environments on the ISS, EML requires significantly less power to levitate samples. By using a superimposed dipole-quadrupole field, where the dipole field heats the sample and the quadrupole field positions the sample, or by using two separate coils, positioning and heating of the sample can be somewhat decoupled from each other. In microgravity, this further enables exploration of the supercooled liquid. EML also offers a high degree of sample stability and control. Compared to the other techniques discussed here, EML also enables the measurement of specific heat and resistivity [51], which are very difficult to measure in liquids on Earth. While not necessarily a drawback for this group, only metallic samples or samples that become metallic in the liquid (like silicon) can be studied in the EML. Further detail on this technique will follow in Chapter 2.

Electrostatic Levitation (ESL) [52,53] is the technique used most throughout this dissertation and will be discussed in more detail in Chapter 2. As a brief overview, ESL uses a set of electrodes and a large negative potential difference to induce a positive surface charge on the sample. As levitation is handled through electrostatic fields, heating and levitation are completely decoupled in the ESL. This allows for some of the broadest temperature ranges to be explored, ranging from the high-temperature liquid down to its maximum supercooling temperature. This large temperature range makes ESL an excellent technique for measuring thermophysical properties like density and viscosity [54]. In terms of stability, ESL techniques are comparable to or better than any other levitation method, including EML. ESL can process any sample that can hold a surface charge, thereby extending its usefulness over EML techniques. However, ESL is a highly complex technique that requires a large array of instruments and supporting equipment to operate.

1.5 Skripov Treatment of the Classical Theory

Nucleation is an inherently random event that can be described using Poisson statistics. The criteria for Poisson statistics to apply to a random event are as follows: (1) events occur independently of each other and (2) they occur with some average frequency. In the case of nucleation, each nucleation event is independent of the previous one and occurs at a specific average supercooling temperature. Skripov [55] derived a probability density function using CNT; a brief outline of his derivation follows below. A similar derivation is included elsewhere if Skripov's publication cannot be obtained [8,56].

The probability of m accidental events occurring in some time interval τ is defined by Poisson's formula:

$$\omega(m,\tau) = \frac{(\lambda\tau)^m}{m!}\exp(-\lambda\tau) \tag{1.34}$$

where λ is the mean rate of occurrence of the events, also known as the Poisson parameter. Equation 1.34 has a maximum value for $m = \lambda\tau$. In practice, λ is a temperature-dependent quantity, which means it also depends on time. Under non-isothermal conditions, the probability of m = 1 event occurring in a time interval of τ+$\delta\tau$ is given by:

$$\omega'(1,\tau+\delta\tau) = \lambda(\tau)\delta\tau\exp\left(-\int_0^{\tau}\lambda(t)dt\right) \tag{1.35}$$

Here, a prime (') symbol has been introduced to separate this probability equation from the final probability density defined at the end of this section. Skripov then takes temperature as an independent variable and defines the constant temperature variation rate (also known as the cooling rate) as $\dot{T} = dT/d\tau$, enabling a transformation of variables giving:

$$\omega'(1,T+\delta T) = \lambda(T)\big(\delta T/\dot{T}\big)\exp\left(-\int_{T_1}^{T}\lambda(T)\big(dT/\dot{T}\big)\right) \tag{1.36}$$

The limits of the integral here are general, but for most applications, it is useful to set the lower limit as the maximum supercooling temperature achieved before nucleation (T_u) and the upper limit as the liquidus temperature (T_l). Skripov then defines the Poisson parameter as:

$$\lambda(T) = I^{ST}V \tag{1.37}$$

where I^{ST} is the classical steady-state nucleation rate and V is the volume nucleated. This parameter emerged from an argument that only a single viable nuclei is required to initiate crystallization in a metastable liquid during some amount of time, which can be expressed as:

$$I^{ST}Vt = 1 \tag{1.38}$$

where t is a characteristic crystallization time. Substituting Eq. 1.37 into Eq. 1.36, dividing over δT and defining the probability density $\omega(T)$ as $\omega'(1,T+\delta T)/|\delta T|$ yields:

$$\omega(T) = \frac{I^{ST}V}{\dot{T}}\exp\left(-\frac{V}{\dot{T}}\int_{T_u}^{T_l} I^{ST}dT\right) \tag{1.39}$$

The only requirements when using Eq. 1.39 for fitting applications is a knowledge of the temperature dependence of A^*, W^*, and σ based on the choice of the approximation for the driving free energy (Eq. 1.22 or 1.23) and whether σ is chosen to be a constant or linearly dependent on temperature. No previous knowledge on whether the observed nucleation event was homogeneous or heterogeneous is required. In practice, both $A*$ and $W*$ are used as fit parameters, which then allows for the direct calculation of σ based on Eq. 1.4. The fit value for A^* and the shape of the distribution will provide clues as to whether a homogeneous or heterogeneous nucleation mechanism was responsible. As described by Turnbull, the value for A^* for heterogeneous nucleation is typically 10 or more orders of magnitude smaller than the value of $A*$ for homogeneous nucleation [15]. Based on laboratory observations, homogeneous nucleation is characterized by a small distribution of supercooling temperatures and a sharply defined peak; heterogeneous nucleation, in contrast, is characterized by a broad distribution of supercooling. In addition, since the form of I^{ST} does not change from CNT to DIT, the same probability density may be fit to a histogram of supercoolings if the correct form of W^* (Eq. 1.4 or Eq. 1.26) is used. In the case of DIT, δ can be calculated from Eq. 1.26 based on the fit value for W^*. More detail on the non-linear, least-squares fitting technique used to fit Eq. 1.39 to distributions of supercooling may be found in Chapter 2.

1.6 Summary and Roadmap of the Dissertation

This chapter covered the relevant nucleation theories and general background needed for the following chapters in this dissertation. Details on the manufacture of samples, processing with containerless techniques, and general overview of analysis techniques are covered in Chapter 2. Chapter 3 presents data from the International Space Station analyzed within the context of both CNT and DIT to begin exploring the impact of diffusion on nucleation. Chapter 4, a version of which was published in the Journal of Chemical Physics, details a set of supercooling experiments performed in ESL on three alloys ($Ti_{39.5}Zr_{39.5}Ni_{21}$, $Ti_{40}Zr_{30}Ni_{30}$, and $Zr_{80}Pt_{20}$) to investigate the role of structure on nucleation. Chapter 5 is a follow up study based on questions reviewers raised to the results in Chapter 4, where two binary alloy families were chosen (Cu-Zr and Zr-Pd) and supercooling experiments were performed on several different compositions within each family ($Cu_{50}Zr_{50}$, $Cu_{55}Zr_{45}$, $Cu_{64}Zr_{36}$, $Zr_{50}Pd_{50}$, $Zr_{45}Pd_{55}$, and $Zr_{75.5}Pd_{24.5}$) to understand the impact of multiple phase formation and structure on nucleation. Chapter 6 will summarize the results of previous chapters and present ideas for future projects.

1.7 References

1. Fahrenheit, D. G. VIII. Experimenta & observationes de congelatione aquæ in vacuo factæ. *Philos. Trans. R. Soc. London* **33**, 78–84 (1724).
2. Black, J. The supposed effect of boiling upon water, in disposing it to freeze more readily, ascertained by experiments. *Philos. Trans.* **65**, 133–134 (1775).
3. Angell, C. A. Supercooled water. *Annu. Rev. Phys. Chem.* **34**, 593–630 (1983).
4. Moore, E. B. & Molinero, V. Structural transformation in supercooled water controls the crystallization rate of ice. *Nature* **479**, 506–508 (2011).
5. Lowitz, J. T. Bemerkungen über das Krystallisiren der Salze, und Anzeige eines sichern Mittels, regelmässige Krystallen zu erhalten. *Chem. Ann.* **1**, 3–11 (1795).
6. Gay-Lussac, L.-J. *De l'influence de la pression de l'air sur la cristallisation des sels*. (1813).
7. Gay-Lussac, L.-J. *Sur la dissolubilité des sels dans l'eau*. (1819).
8. Kelton, K. & Greer, A. L. *Nucleation in condensed matter: applications in materials and biology*. **15**, (Elsevier, 2010).
9. Gibbs, J. W. *Scientific Papers*. (Longmans, Green, and Co, 1906).
10. Chisholm, M. F. Spinodal Nucleation in Binary Alloys. *Diss. Abstr. Int.* **47**, 156 (1987).
11. Volmer, M. & Weber, A. Keimbildung in übersättigten Gebilden. *Zeitschrift für Phys. Chemie* **119**, 277–301 (1926).

12. Becker, R. & Döring, W. Kinetische Behandlung der Keimbildung in übersättigten Dämpfen. *Ann. Phys.* **416**, 719–752 (1935).

13. Turnbull, D. & Fisher, J. C. Rate of nucleation in condensed systems. *J. Chem. Phys.* **17**, 71–73 (1949).

14. Turnbull, D. & Cech, R. E. Microscopic observation of the solidification of small metal droplets. *J. Appl. Phys.* **21**, 804–810 (1950).

15. Turnbull, D. Formation of crystal nuclei in liquid metals. *J. Appl. Phys.* **21**, 1022–1028 (1950).

16. Turnbull, D. Kinetics of Solidification of Supercooled Liquid Mercury Droplets. *J. Chem. Phys.* **20**, 411–424 (1952).

17. Frank, F. C. Supercooling of Liquids. *Proc. R. Soc. London.* **215**, 43–46 (1952).

18. Shechtman, D. The Nobel Prize in Chemistry 2011. (2011).

19. Kelton, K. F. *et al.* First X-Ray Scattering Studies on Electrostatically Levitated Metallic Liquids: Demonstrated Influence of Local Icosahedral Order on the Nucleation Barrier. *Phys. Rev. Lett.* **90**, 195504 (2003).

20. Kelton, K. F. Crystal Nucleation in Liquids and Glasses. *Solid State Phys. - Adv. Res. Appl.* **45**, 75–177 (1991).

21. Landau, L. D. & Lifshitz, E. M. *Statistical Physics*. (Pergamon Press, 1969).

22. Kelton, K. F., Greer, A. L. & Thompson, C. V. Transient nucleation in condensed systems. *J. Chem. Phys.* **79**, 6261–6276 (1983).

23. Zeldovich, Y. B. On the theory of new phase formation: cavitation. *Acta Physicochem. USSR* **18**, 1 (1943).

24. Frenkel, J. *Kinetic Theory of Liquids*. (Clarendon Press, 1946).

25. Kashchiev, D. Solution of the non-steady state problem in nucleation kinetics. *Surf. Sci.* **14**, 209–220 (1969).

26. Thompson, C. V & Spaepen, F. On the Approximation of the Free Energy Change on Crystallization. *Acta Metall.* **27**, 1855 (1979).

27. Turnbull, D. Physics of non-crystalline solids. in *Physics of Non-crystalline Solids. Proc Int Conf. Prins JA edition* 41–56 (North-Holland, Amsterdam, 1964).

28. Spaepen, F. A structural model for the solid-liquid interface in monatomic systems. *Acta Metall.* **23**, 729–743 (1975).

29. Spaepen, F. & Meyer, R. B. The surface tension in a structural model for the solid-liquid interface. *Scr. Metall.* **10**, 257–263 (1976).

30. Spaepen, F. Homogeneous nucleation and the temperature dependence of the crystal-melt interfacial tension. in *Solid State Physics* (eds. Ehrenreich, H. & Turnbull, D.) **47**, 1–32 (Academic Press, 1994).

31. Gránásy, L. Diffuse interface theory of nucleation. *J. Non. Cryst. Solids* **162**, 301–303 (1993).

32. Gránásy, L. Nucleation theory for diffuse interfaces. *Mater. Sci. Eng. A* **178**, 121–124 (1994).

33. Van Duijneveldt, J. S. & Frenkel, D. Computer simulation study of free energy barriers in crystal nucleation. *J. Chem. Phys.* **96**, 4655–4668 (1992).

34. Harrowell, P. & Oxtoby, D. W. A molecular theory of crystal nucleation from the melt. *J. Chem. Phys.* **80**, 1639–1646 (1984).

35. Kelton, K. F. *et al.* Oxygen precipitation in silicon: Experimental studies and theoretical investigations within the classical theory of nucleation. *J. Appl. Phys.* **85**, 8097–8111 (1999).

36. Wei, P. F., Kelton, K. F. & Falster, R. Coupled-flux nucleation modeling of oxygen precipitation in silicon. *J. Appl. Phys.* **88**, 5062–5070 (2000).

37. Kelton, K. F. Diffusion-influenced nucleation: A case study of oxygen precipitation in silicon. in *Philosophical Transactions of the Royal Society A: Mathematical, Physical and Engineering Sciences* **361**, 429–446 (2003).

38. Kelton, K. F. Time-Dependent Nucleation in Partitioning Transformations. *Acta Mater.* **48**, 1967–1980 (2000).

39. Kelton, K. F. Kinetic model for nucleation in partitioning systems. *J. Non. Cryst. Solids* **274**, 147–154 (2000).

40. Russell, K. C. Linked flux analysis of nucleation in condensed phases. *Acta Metall.* **16**, 761–769 (1968).

41. Press, W. H., Teukolsky, S. A., Vetterling, W. T. & Flannery, B. P. *Numerical recipes in Fortran 77: the art of scientific computing*. **2**, (Cambridge university press Cambridge,

1992).

42. Kelton, K. F., Gangopadhyay, A. K., Hyers, R. & Holland-Moritz, D. Studies of Nucleation and Growth, Specific Heat and Viscosity of Undercooled Melts of Quasicrystals and Polytetrahedral-Phase-Forming Alloys. *Science Requirements Document (SRD), QUASI-RQMT-0001* (2002).

43. Marangoni, C. On the expansion of a drop of liquid floating on the surface of another liquid. *Tipographia dei Frat. Fusi, Pavia* (1865).

44. Hyers, R. W. Fluid flow effects in levitated droplets. *Meas. Sci. Technol.* **16**, 394–401 (2005).

45. Schroers, J. *et al.* Enhanced temperature uniformity by tetrahedral laser heating. *Rev. Sci. Instrum.* **75**, 4523–4527 (2004).

46. Nordine, P. C., Weber, J. K. R. & Abadie, J. G. Properties of high-temperature melts using levitation. *Pure Appl. Chem.* **72**, 2127–2136 (2000).

47. Cuello, G. J., Cristiglio, V., Hennet, L. & Puente-Orench, I. Neutron scattering at high temperature and levitation techniques. *J. Phys. Conf. Ser.* **549**, (2014).

48. Tian, Y., Holt, R. G. & Apfel, R. E. A new method for measuring liquid surface tension with acoustic levitation. *Rev. Sci. Instrum.* **66**, 3349–3354 (1995).

49. Weber, J. K. R. *et al.* Aero-acoustic levitation: A method for containerless liquid-phase processing at high temperatures. *Rev. Sci. Instrum.* **65**, 456–465 (1994).

50. Holland-Moritz, D., Schenk, T., Convert, P., Hansen, T. & Herlach, D. M.

Electromagnetic levitation apparatus for diffraction investigations on the short-range order of undercooled metallic melts. *Meas. Sci. Technol.* **16**, 372–380 (2005).

51. Wunderlich, R. K. & Fecht, H. J. Modulated electromagnetic induction calorimetry of reactive metallic liquids. *Meas. Sci. Technol.* **16**, 402–416 (2005).

52. Rhim, W. K., Collender, M., Hyson, M. T., Simms, W. T. & Elleman, D. D. Development of an electrostatic positioner for space material processing. *Rev. Sci. Instrum.* **56**, 307–317 (1985).

53. Gangopadhyay, A. K. *et al.* Beamline electrostatic levitator for in situ high energy x-ray diffraction studies of levitated solids and liquids. *Rev. Sci. Instrum.* **76**, 073901 (2005).

54. Bendert, J. C. & Kelton, K. F. Containerless measurements of density and viscosity for a Cu48Zr52 liquid. *Int. J. Thermophys.* **35**, 1677–1686 (2014).

55. Skripov, V. P. Homogeneous Nucleation in Melts and Amorphous Films. *Curr. Top. Mater. Sci.* **2**, 328–378 (1977).

56. Wert, M. J. Investigation of Effects of Dilute Oxygen Solute on Nucleation of Zirconium. (Vanderbilt University, 2002).

Chapter 2: Materials and Methods

Due to the large number of samples produced, many group members, including A. K. Gangopadhyay, C. E. Pueblo, and D. Van Hoesen were involved in the manufacture of samples and acquisition and analysis of data. The following chapter describes the relevant methods used for (i) sample preparation (2.1), (ii) containerless processing within the Washington University Beamline Electrostatic Levitator (WU-BESL) (2.2.1) and the Electromagnetic Levitator (EML) on the International Space Station (ISS) (2.2.2), (iii) thermophysical property measurements including density (2.3.1) and viscosity (2.3.2), (iv) X-ray diffraction measurements (2.4), (v) nucleation measurements using the EML facility on-board the ISS and on earth using the WU-BESL (2.5), and (vi) the nonlinear, least-squares fitting routines performed using the Skripov probability density function (2.6).

2.1 Sample Preparation

Master ingots, typically one gram in mass, were prepared from high-purity (99.95% or greater) elemental source material obtained from Alfa Aesar, now part of Thermo Fischer Scientific. If possible, material in bar or rod form was used to reduce exposure to oxygen, as form-factors like metallic sponge, shot, or powder have a larger surface area exposed to ambient air and likely contain more oxygen. In addition, Alfa Aesar provides an elemental analysis of its stock to further guarantee the purity. The source material was stored in a glovebox filled with a Grade 5 (99.999%) argon atmosphere and was only removed before weighing and arc-melting. Alloys compositions are typically given in atomic percentages instead of weight percentages. The mass needed of the source material for element i in the alloy, its mass m_i is given by Eq. 2.1:

$$m_i = \frac{x_i M_i}{\sum_j^N x_j M_j} m_{ingot} \tag{2.1}$$

where x_i and M_i are the atomic percent and the molar mass of the i-th element, N is the number of elements composing the alloy, and m_{ingot} is the total desired mass of the master ingot. In practice, m_{ingot} is usually set to one gram for simplicity, since a one-gram ingot can typically yield anywhere from 12 to 17 samples for ESL processing. A Mettler Toledo AB54/FACT mass balance, with a precision of ±0.1mg, was used to weigh the elemental source material. Some materials, such as the 99.97% purity crystal Zr bar, were too difficult to cut using bolt cutters, so the crystal bar was sliced into thin sections using a Techcut 4 saw with a diamond wafering blade. The slice was subsequently cleaned in three steps—first with xylenes, then acetone, and finally methanol— using a Branson 2510 ultrasonic cleaner to remove dust, coolant, and residue from the previous washing from the surface of the slice. The source materials were manipulated on fresh, clean tissue wipes and only using tweezers and bolt cutters that had been wiped clean with acetone and methanol to further reduce the introduction of contamination into the ingot. This is seen in Fig. 2.1.

Figure 2.1: Zirconium cut from a 99.97% pure (nominal 2% hafnium) crystal bar (left) and platinum cut from a 99.997% pure wire (right). Large pieces are generally preferred to minimize the surface exposed to the atmosphere and to ensure all pieces are melted together.

To minimize contamination from the manufacture of other samples, the water-cooled copper hearth of the arc-melter was first sanded with 600 grit sandpaper and wiped repeatedly with acetone and methanol. The tungsten tip was filed before use to remove any deposition from other elements, which could be vaporized and introduced into the ingot during arc-melting. Once the required masses for each element had been cut from bar stock, the material was placed on the freshly cleaned hearth. The material was stacked such that the element with the highest melting temperature is placed on top of the pile, nearest the tungsten electrode, which ensured all material would melt when struck with the arc. The chamber was evacuated to $1 - 3.5\text{x}10^{-5}$ Torr, which typically took 15 to 30 minutes, and back-filled with a low-pressure atmosphere of high-purity (99.999%) argon. This pumping and refilling process was repeated three to five times to reduce the oxygen present within the chamber. After the final cycle, the chamber was filled with argon to a pressure of approximately 600 Torr.

Figure 2.2: (Left) A top-down view of the copper hearth of the arc-melting facility. The vacuum feedthrough and the tungsten tip are positioned in the center of the hearth. At the 10 o'-clock position is a $Ti_{50}Zr_{50}$ getter, while at the 2 o'-clock position is the elemental zirconium crystal bar and platinum wire. (Right) The finished ingot of $Zr_{80}Pt_{20}$ after arc melting.

A Miller Synchrowave 250DX arc-welding power source was connected via a vacuum feedthrough to the tungsten tip. The arc-melting facility is pictured in Fig. 2.2. The arc was initially struck over the copper hearth and then moved to a $Ti_{50}Zr_{50}$ getter, which was melted and held in its liquid state for approximately 60 seconds to reduce the oxygen concentration. The arc was then moved to the ingot material and held until the element with the highest melting point turned into a liquid. After the material had coalesced into a spherical ingot, the arc was circled around the ingot to further mix the elements together. This process typically took no more than 15 seconds since prolonged exposure to the arc could result in significant mass-loss (and a compositional shift) in the final ingot. After melting and mixing the ingot, the arc was extinguished and the tungsten tip was used to flip the ingot over to further stir the elements together. The process was then repeated two more times to ensure the ingot was well-mixed. The final mass of the ingot was measured to determine any mass loss. If mass loss was observed, the ingot composition was recalculated assuming the loss was due to a single, preferentially evaporating element. Typically, this element had the highest vapor pressure (such as copper or aluminum) of all the components in the alloy. After recalculating the composition, if a shift of more than 0.5% atomic percent was found, the ingot was rejected.

For studies within the BESL, a sample mass of approximately 45-75 mg, corresponding to a sample 2 – 2.5 mm in diameter, was desired. The ingot was crushed into large (20-60mg) pieces and re-melted into spheres using the previously discussed arc-melting procedure. Crushing the ingot into a fine metallic powder (pieces approximately 5mg or smaller) typically resulted in contaminated samples that are not ideal for supercooling experiments. However, the ESL samples were melted only once and for no more than two seconds, since the samples were assumed to have the same composition as the master ingot and did not require further mixing. A photo of ESL samples after arc-melting is shown in Fig 2.3.

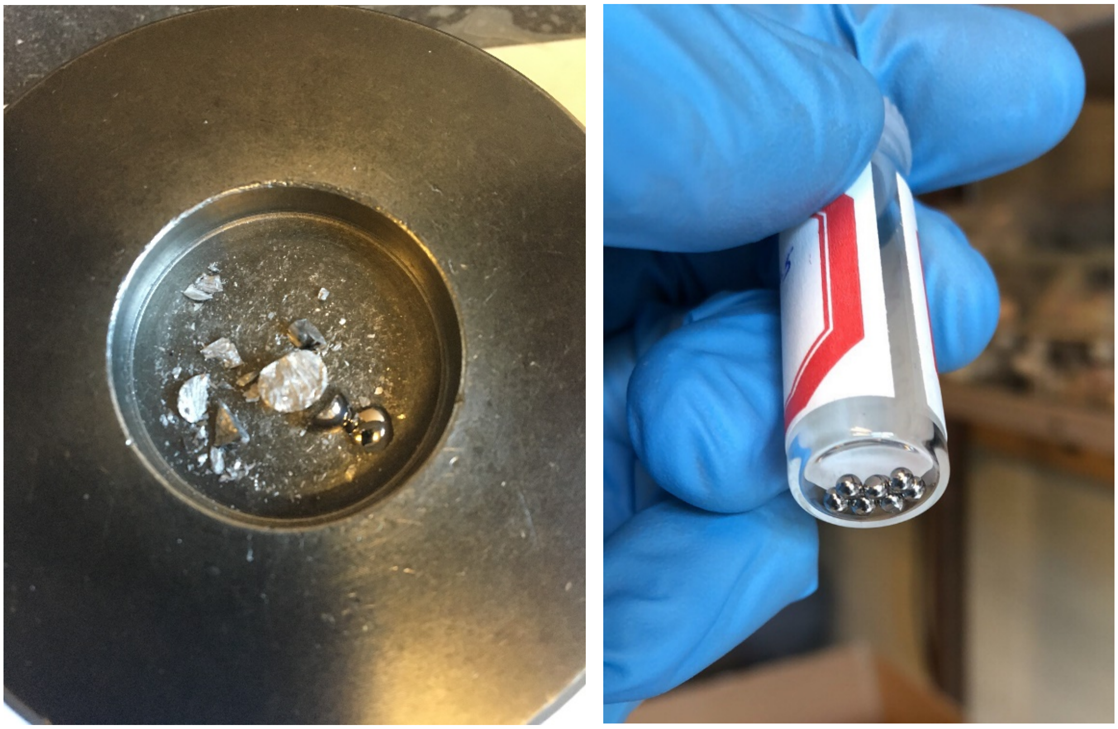

Figure 2.3: (Left) A one-gram ingot crushed into smaller pieces for manufacturing ESL samples. Larger chunks are preferred to minimize the introduction of contamination. (Right) ESL-sized samples after arc-melting them into spheres roughly 2mm in diameter. Seven samples were made from approximately half of the corresponding master ingot. The remaining half of the ingot was kept inside the glovebox under argon for later use.

A similar procedure was followed for the preparation of samples for the ISS. However, due to constraints on the amount of dust produced by samples, the surface area and "sphericity" of these samples must be well-documented. Further detail on the particularities of manufacturing samples for the ISS can be found in Dr. Chris Pueblo's thesis [1].

2.2 Containerless Processing Techniques

2.2.1 Electrostatic Levitation

The BESL facility at Washington University enabled containerless processing of metallic liquids in a high-vacuum (1.8 – 8.5 x 10^{-8} Torr) environment. This pressure was typically achieved by pumping on the ESL chamber for a minimum of 1.5 days, although longer evacuation times were sometimes needed in especially humid weather. The high-vacuum was achieved using both Osaka Vacuum TG420M and Pfeiffer Vacuum Hi-Pace 80 turbo pumps, each backed by a Leybold Scrollvac SC15D scroll pump. The ESL room was climate controlled and dehumidifiers were used to ensure the coldest environment and lowest humidity possible to maximize the efficiency of the scroll and turbo pumps.

To levitate the sample, the BESL used three sets of orthogonal electrodes (two for each x, y, and z Cartesian coordinate) to generate three potential differences. Two sets of horizontal electrodes, made of stainless steel, were used to control the lateral (x, y) position of the sample. The final set of electrodes, made of copper, controlled the vertical z position of the sample. Each set of electrodes consisted of one grounded electrode and one electrode at high potential connected via a vacuum feedthrough to one of three high-voltage amplifiers. The two amplifiers for each set of horizontal electrodes could vary the potential difference between ± 3 kV, while the amplifier for the vertical electrodes could vary the potential difference from 0 to -20 kV. Unlike the flat horizontal electrodes, the vertical electrodes consisted of a curved bottom and a hemispherical top. The curvature chosen for the vertical electrodes was demonstrated previously to improve the lateral stability without a major cost to vertical stability [2,3], as compared to flat top and bottom electrodes. The electrodes and a levitating sample are shown in Fig. 2.4.

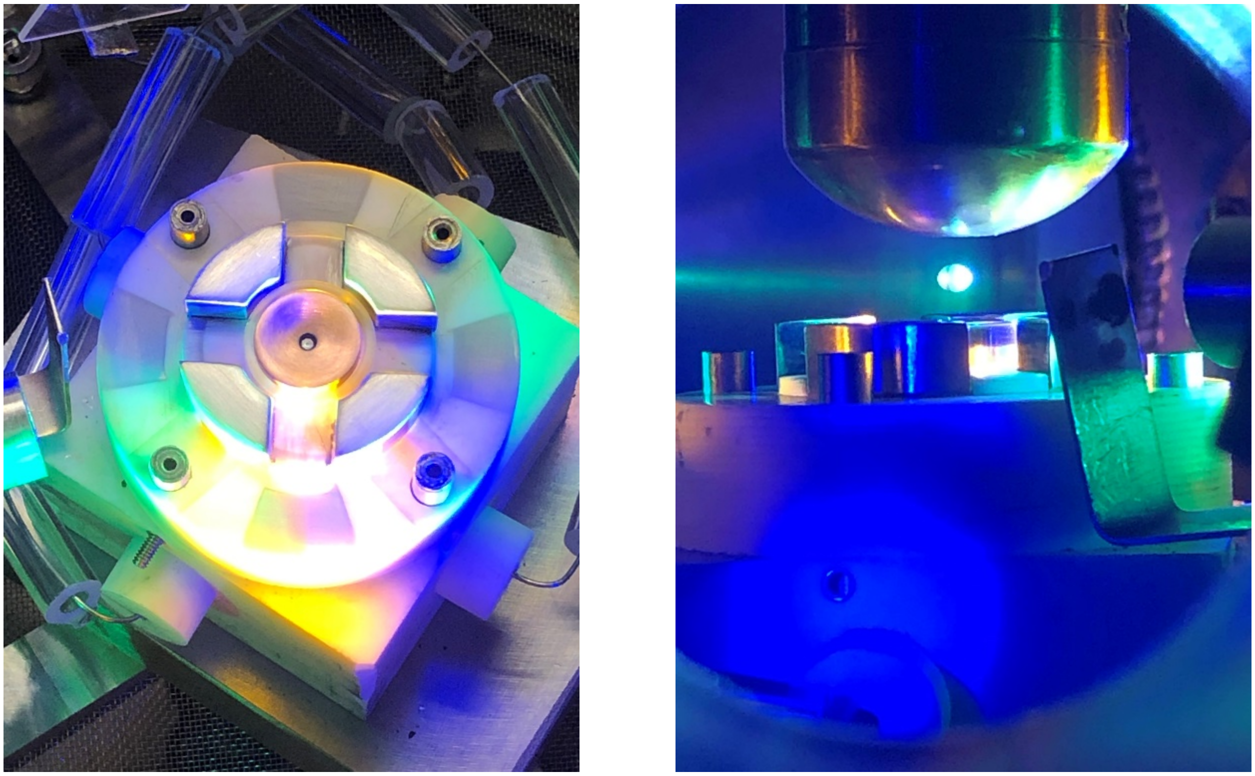

Figure 2.4: (Left) A photo of the bottom electrode after cleaning. Note that the copper bottom electrode is slightly curved, like a cup. The dot in the middle of the bottom electrode is the sample post, which can be raised up to the top electrode to load a sample. (Right) A levitated sample of aluminum, roughly 3mm in diameter for scale, viewed through an open port near the Blue LED on the ESL. The bent metal bar on the right is the shutter for the vacuum ultraviolet lamp. Note also the curvature of the top electrode; the gap between the top and bottom electrode is approximately 9mm.

A set of high-intensity light emitting diodes (LEDs) and position sensitive detectors (PSDs) located opposite of the LEDs allowed the position of the levitated sample to be tracked. The LEDs, operating at 455 nm in the *x*-direction and 530 nm in the *y* and *z*-directions, projected a shadow of the sample into their corresponding PSDs. Bandpass filters in front of each PSD ensured that only light corresponding to the correct LED was measured, greatly reducing crosstalk and interference from other light sources. The signal from the PSD was passed to a target PC running a MATLAB-based active feedback algorithm, which manipulated the voltages sent to the electrodes by the corresponding amplifier to both stabilize the sample position and adjust it to a desired location [4].

Active feedback and constant modulation of the voltages were required since the electrodes created a 3-dimensional saddle point for the sample. This technique is described in more detail elsewhere [4,5]. In practice, this system resulted in a sample stability to within a minimum of 10 μm.

To melt levitated samples, a fiber-coupled nLight Pearl P2-050-0980-3-R diode laser, operating at 980nm with a 50W continuous maximum power output was used. As the temperature of the sample increased and it passed through various phase transitions, impurities on the surface and gas within the grain boundaries of the crystal phase were evaporated from the sample. This process decreased the surface charge of the sample and could result in instability or loss of the sample. Previous processing methods involved using the sample post to raise the sample into the heating laser to melt it into a sphere. While this did smooth out any flat surfaces left over from arc-melting and further reduced sample impurities, it also potentially introduced contamination at the point of contact between the sample and the post. Therefore, for all the ESL-based nucleation experiments described in this thesis, the sample was loaded and launched without processing on the post to minimize contamination. While this sometime resulted in sample instability due to non-spherical geometries and loss of gas and other impurities, it ensured cleaner samples were examined. A high-intensity vacuum ultraviolet (VUV) lamp was used to recharge the sample via the photoelectric effect to help stabilize the sample during its initial heating and melting. Once a sufficiently high temperature was achieved, most impurities had evaporated and thermionic emission was sufficient to recharge the samples. After multiple heating and cooling cycles, the sample typically achieves its maximum stability.

A technique called "gain-switching" was used to more reliably levitate and process samples within the ESL, thereby greatly improving the success rate for each sample. Dr. Dante Quirinale at the Spallation Neutron Source (SNS) at Oak Ridge National Laboratory (ORNL) suggested this technique. It was based on his experience using both an ESL that was based on the design of the WU-BESL, which is located at AmesLab in Iowa State University, and the Neutron Electrostatic Levitator (NESL) built by this group and located permanently at ORNL. To "gain-switch" means to modify the gains for the x, y, and z voltages before levitating the sample and, once the sample has been launched, to quickly reduce them to a specified value. In practice, this means setting the gain for the relevant PSD voltage (labeled in MATLAB as the "Green X", "Green Y", and "Blue X" parameters) to a value roughly 2.5 to 3 times its starting value (typically changing the gain from -0.0029 to -0.01 or -0.012) and then lowering the gain to around half of this value (-0.006) once the sample is levitated. The higher gains typically allowed for a smoother launch, much like a plane taking off from a runway. Previous sample launch techniques were more like throwing a ball into the air and attempting to catch it with a mid-air jump—doable, but inherently unreliable, especially for smaller, high density samples. The reasons why gain-switching resulted in more reliable launches and processing are not well understood, but it is speculated that the original gain values in the algorithm were not well determined, possibly resulting in an algorithm that is overly responsive. More discussion of this phenomenon can be found in the Ph.D. thesis of Dr. Gustav Rustan from Iowa State University [6].

A Process Sensors Metis MI18 MB8 single-color pyrometer operating at a wavelength of 1.89µm was used to measure the sample temperature in the range from 160 °C to 800 °C. A Process Sensors Metis MQ22 two-color ratio pyrometer, operating at wavelengths of 1.4µm and 1.64µm, was used to measure sample temperatures above 600 °C and up to 2300°C. An initial set of emissivity values was used to determine the approximate temperatures during processing. A known thermal signature specific to the alloy was used to calibrate the ratio pyrometer, which provides the ratio of the emissivity at two different wavelengths. In practice this was a solidus or liquidus temperature measured by other techniques or obtained from published literature. If the sample supercooling bypassed the range accessible by the ratio pyrometer, then the temperature data from the low-temperature pyrometer was matched to that from the high-temperature pyrometer within their overlapping temperature range. The details regarding this process and the relative uncertainties in temperature calibration can be found elsewhere [1,7]. A photo of the ESL and supporting equipment rack is shown in Fig. 2.5. A cross-section schematic of the main ESL vacuum chamber, instruments, and sensors is shown in Fig. 2.6.

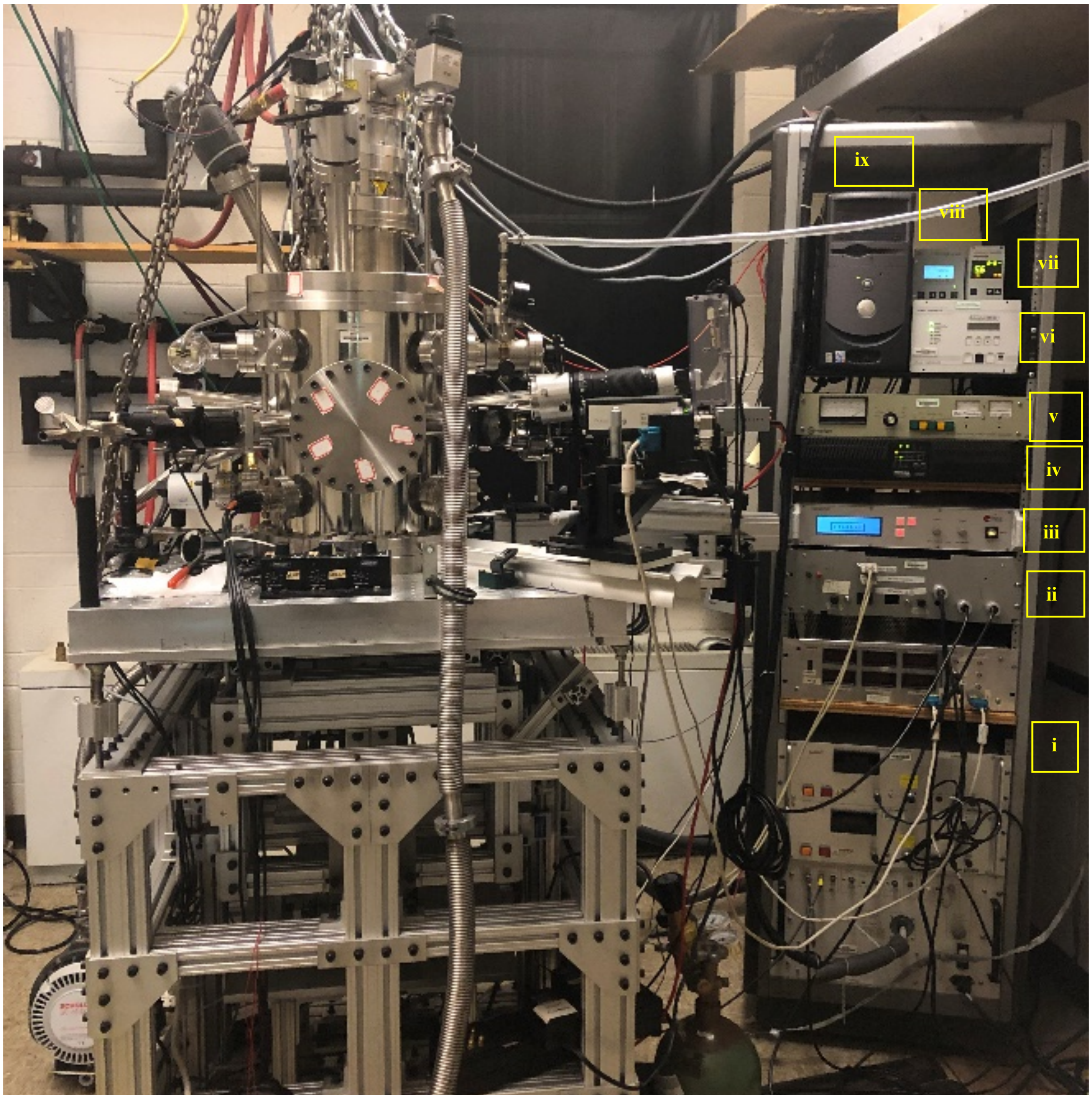

Figure 2.5: A photo of the ESL facility at Washington University. The chamber rests on a table that can be raised or lowered to align the levitated sample with the incident X-ray beam during scattering experiments. The rack on the right houses (from bottom to top) (i) the high voltage amplifier for the z, y, and x voltages, (ii) a readout of the PSDs to check for alignment, (iii) the VUV control panel, (iv) a backup battery for the Osaka turbo pump, (v) a Varian ion gauge controller, (vi), controllers for both the (vi) Osaka and (viii) Pfeiffer turbo pumps, (vii) a readout for the cold-cathode gauge, and (ix) the levitation algorithm control PC.

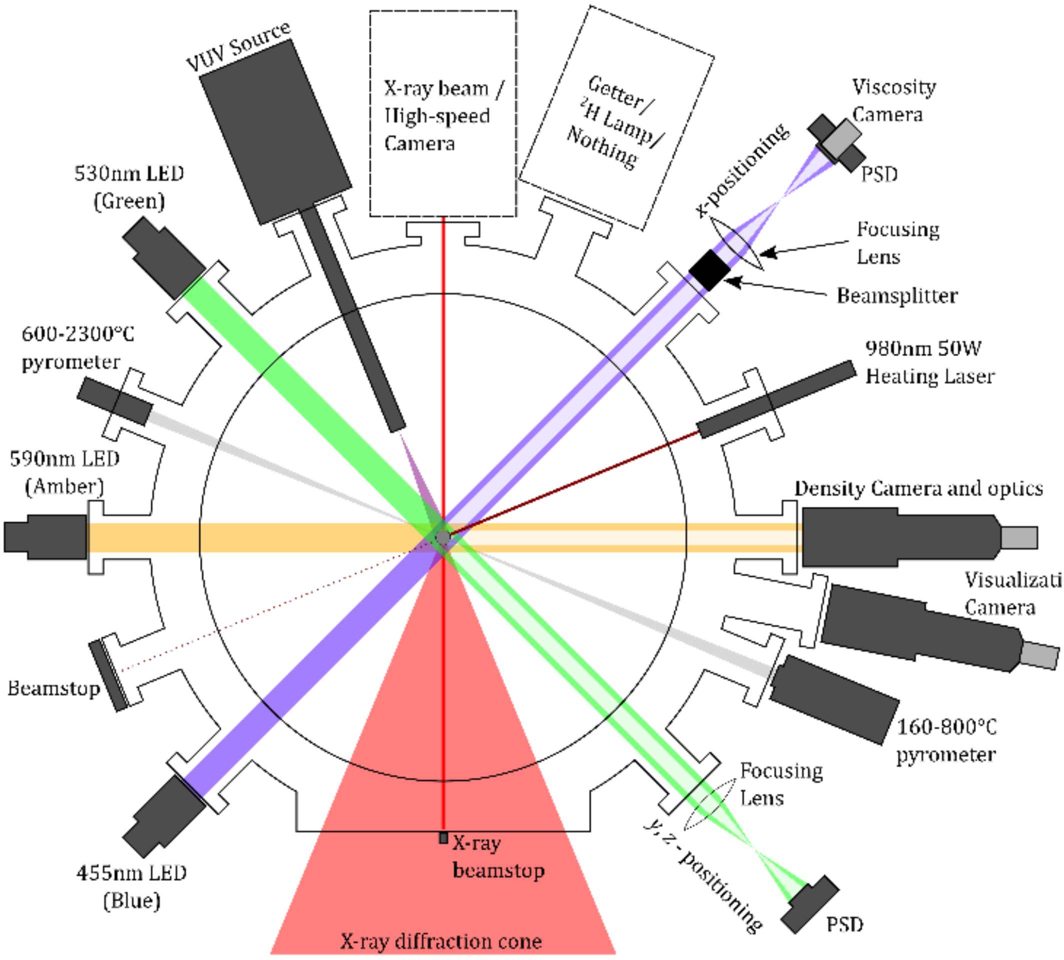

Figure 2.6: A cross section of the ESL chamber. The LEDs cast a shadow on the sample, represented here as a lighter hue, into the PSD. For X-ray studies, a beam stop is placed in-line with the incident X-ray beam and the high-speed camera is removed. Image reprinted from [8] with permission from Dr. Robert Ashcraft.

2.2.2 Electromagnetic Levitation

The Electromagnetic Levitation (EML) facility on-board the International Space Station (ISS) was used to perform containerless processing of samples in a microgravity environment. In principle, either ESL or EML techniques can be used to levitate samples in space. However, on Earth, EML has a distinct disadvantage when compared to ESL. Due to the force of gravity, stronger magnetic fields are required to levitate the sample in EML, which in turn heats the sample and limits the temperature region that can be explored. In ESL, heating and levitation are decoupled, making it the preferred method for studying supercooled metallic liquids under terrestrial conditions. However, in microgravity, EML offers some advantages when compared to ESL, namely the ability to measure resistivity directly as an impedance and to potentially measure the specific heat without errors due to the unknown emissivity. Further detail on resistivity and specific heat measurement techniques may be found elsewhere [9]; this thesis does not cover measurements of resistivity and specific heat. Thermophysical property data, like viscosity and growth velocity, can be obtained in both EML and ESL.

To levitate samples in the EML, a high frequency rf current was passed through a set of water-cooled copper coils to produce a magnetic field, which induced eddy currents in the sample within the coils. The interaction between the imposed magnetic field and resulting eddy currents allowed for control of the sample position. Since the eddy currents were confined to within a small thickness near the sample surface, the sample was heated resistively. Because of the microgravity conditions, the fields required to levitate a sample were much smaller than those required on earth. Therefore, heating and levitation were somewhat more decoupled in this facility, enabling a broader temperature range to be probed. The decoupling was further enhanced by using separate quadrupole and dipole fields to control sample positioning and heating (see next paragraph). A more in-depth description including photos, a schematic overview of the entire EML facility, a description of the modules and payload, and the projected life-cycle for the EML, can be found elsewhere [10].

In the EML on the ISS, a quadrupole magnetic field operating at 140 kHz controlled the positioning field, while a dipole magnetic field operating at 380 kHz controlled the heating of the sample. The quadrupole positioning field was not very efficient at heating the sample, while the dipole field did not contribute much to sample levitation. A cartoon representation of these coils is represented in Fig. 2.6, which has been adapted from Lohofer with permission from AIP Publishing [11]. A two-color pyrometer, operating at 1.45 µm and 1.8 µm, with a sampling rate of 100Hz and a spot size of 0.8mm, was used to measure the sample temperature, much like in the ESL. In principle, the pyrometer can measure temperatures from 300 to 2100 °C; however, in practice, the pyrometers are more effective starting at 600 °C. Emissivity corrections were performed in a similar way to those outlined earlier.

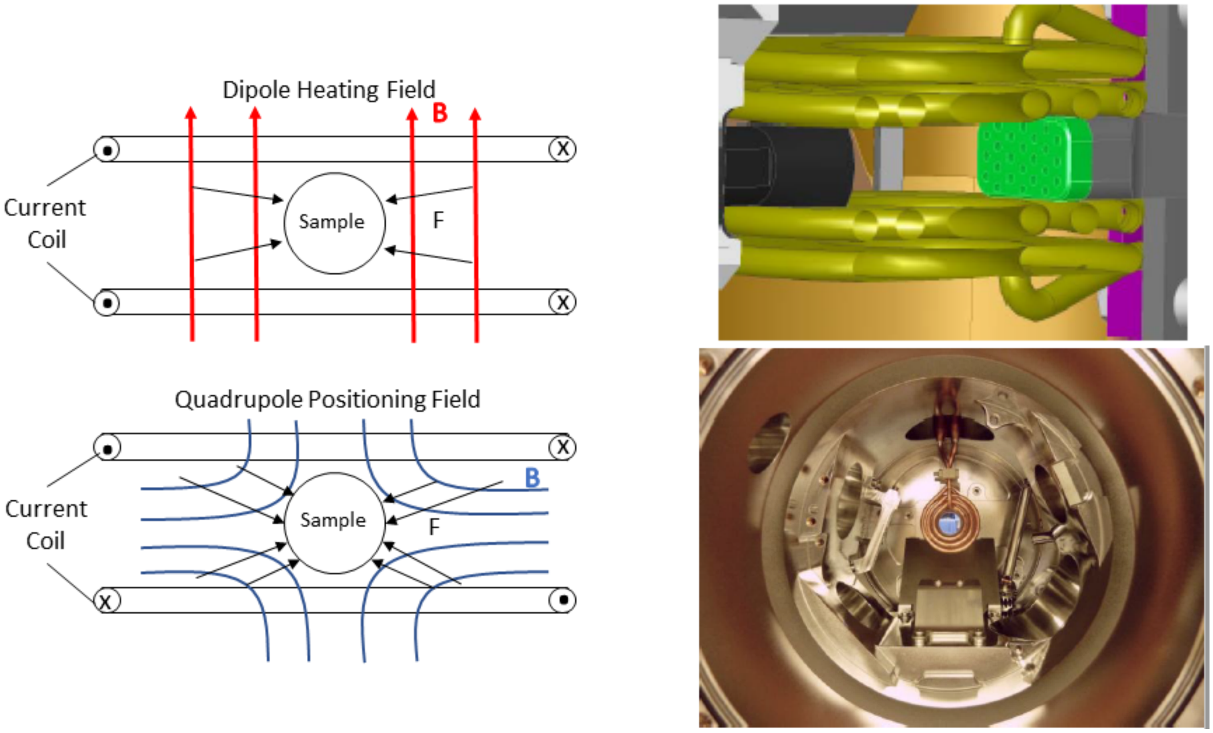

Figure 2.7: (Left) A schematic representation of the heating and positioning coils with the resulting electromagnetic fields superimposed. In the simplest EML facility, only a single coil is used, which performs both heating and positioning. Image adapted from Lohofer [11] with permission from AIP Publishing. (Top right) A rendering of the EML coil (yellow), with gas flow regulated by the green nozzle. (Bottom right) Actual image of the coil and sample environment within the EML. The sample is positioned in the middle of the copper coil. Right images courtesy of the DLR [12].

2.3 Thermophysical Property Measurements

Arguably one of the greatest strengths of ESL processing is the ability to use non-contact measurement techniques to determine thermophysical properties of the liquid samples. In principle, these techniques are well-known and have been extensively outlined elsewhere. A brief summary is outlined below.

2.3.1 Density Measurements

The shadow technique [13] was used to measure the density of the liquid sample. Before measurements were made, the sample was repeatedly heated and cooled to maximize the supercooling (also known as sample conditioning). After reaching the maximum supercooling, the amber (590 nm) LED was used to illuminate the sample. A Pixelink PLB74IG CMOS camera recorded its shadow at 25 frames per second (fps) as the sample cooled radiatively from its liquid phase to recalescence. To ensure good contrast between the sample edge and the surrounding environment the amber LED was typically set to maximum intensity and the exposure time of the Pixelink camera was set to approximately 1 ms. During radiative cooling the liquid droplet is assumed to be symmetric about the vertical axis (z) and an edge detection algorithm written in LabVIEW was used to determine the radius of the sample as a function of z. The pixels were then integrated to determine the total area of the shadow. Known references, in this case being Grade 3 tungsten carbide spheres with a well-known diameter of $3/32 \pm 2 \times 10^{-5}$ inches, were used to convert from pixel area to actual area. The volume was determined by integrating around the z axis. The density was obtained by dividing the calculated volume by the measured mass. Video data from multiple cooling cycles were averaged to obtain the density as a function of temperature.

Further descriptions of this technique, including a description of the Bradshaw edge-finding algorithm and relative uncertainties, may be found elsewhere [14,15].

2.3.2 Viscosity Measurements

The oscillating drop technique was used to measure the viscosity of the liquid samples. In 1881, Lamb derived the formula describing the decay of the n^{th} surface harmonic of a sphere as:

$$\tau_n = \frac{\rho a^2}{\eta(n-1)(2n+1)} \tag{2.2}$$

where ρ is the density, a is the radius of the sphere, n is the mode of oscillation, and η is the viscosity [16]. By overlapping a sinusoidal oscillation onto the vertical voltage signal, the $n = 2$ "breathing-mode" harmonic could be excited. Subsequently removing this oscillation caused the liquid to behave like an underdamped harmonic oscillator, with a decay constant related to its viscosity, η.

Just as for the density studies, before taking measurements, the sample was conditioned until deep supercooling was observed. The induced oscillations and decay of the sample were recorded by splitting 50% of the collimated light from the blue LED into another Pixelink PL-B74IG CMOS camera operating at 1500fps. The recorded oscillations and decay in sample surface area were fit to an equation of the form:

$$S(t) = A\sin(2\pi f_0 t + \varphi)\exp\left(-\frac{t}{\tau}\right) \tag{2.3}$$

where A is the initial amplitude of the oscillation, f_0 is the frequency, φ is the phase shift, and τ is the decay time, as described earlier. The temperature was gradually changed and the sinusoidal driving frequency was manually adjusted until the breathing-mode resonance was found. Once the resonance was found, automated measurements could be made, allowing multiple data points to be acquired in a short period of time across a range of temperatures. Further discussion of this technique, especially involving the reduction of viscosity video and analysis of data, can be found elsewhere [1,2,14]. Once the data were reduced, they were fit using several different viscosity equations [17], principally the KKZNT model [18–20]. The fit parameters were extracted for use in the curve fitting program discussed later.

2.4 X-ray Diffraction Measurements

Another advantage of ESL processing is the ability to make containerless diffraction measurements of liquids. The removal of a container eliminates a major source of noise in the data, which allows for a more accurate probing of the liquid structure. This section briefly details Wide-Angle X-ray Scattering (WAXS) measurements made at the Advanced Photon Source (APS), beamline 6-ID-D (located at Argonne National Lab, ANL) during the BESL2016 run. The data analysis techniques used are also briefly discussed.

Before a scattering run at the APS, the ESL and all supporting components were dismantled, packaged into crates, and transported up to ANL. Many samples were studied, including bulk-cast metallic glasses, pure elements, and other alloys of interest. To maximize the data acquisition time, three 8-hour shifts were run during the time between June 13th, 2016 and July 5th, 2016. Each shift contained a minimum of three people, allowing one person to control sample levitation and heating, a second person to control the X-ray shutter, and a third person to run the data acquisition programs for the detector. Due to the high flux (~ 10^{11} photons/sec) of high-energy X-rays (131.737 keV, $\lambda = 0.0941149$Å) the scattering measurements could be performed very quickly with sufficient statistics to obtain accurate structural information. In contrast, inelastic neutron scattering measurements performed at the Spallation Neutron Source (SNS) using the Neutron Electrostatic Levitation (NESL) at Oak Ridge National Lab can take upwards of 2 hours to gather sufficient statistics [8]. Further information about the BESL2016 run is detailed in Dr. Robert Ashcraft's thesis [8].

Upon arrival at the APS, the ESL was re-constructed and aligned vertically and laterally with the X-ray beam via the movable stage. The front and rear ports were replaced with beryllium windows to allow the incident X-rays and scattered X-rays to both enter and leave the chamber. Beryllium windows were chosen because of their smaller scattering cross section, which increased the intensity on the sample and reduced unnecessary background scattering.

A GE Revolution 41-RT amorphous Si flat panel area detector was used to detect the scattered X-rays from samples. The area detector could operate with a sampling rate of 1 – 2Hz and with a resolution of 2048 x 2048 pixels, where each pixel was a 200 μm square. The working distance, tilt angle, and rotation angle between the sample and the detector was calibrated by fitting the diffraction rings from polycrystalline Si NIST standards levitated in the same position as the sample. A beam stop, as represented earlier in Fig. 2.6, was installed outside the beryllium window located downstream from the sample to protect the detector from exposure to the incident X-ray beam. However, because the X-ray beam was nominally the same size as the studied samples, misalignment of the sample with the beam could produce anisotropic scattering intensity. A bad pixel map was also applied to the data to minimize errors associated with malfunctioning pixels on the detector.

The scattering intensity data were analyzed using an in-house LabVIEW software program written by Dr. James Bendert [2,21] and further modified by Dr. Mark Johnson [22]. The goal was to obtain the static structure factor, *S(q)*, and the pair-distribution function, *g(r)*, for the liquids and crystals studied. A brief overview of the analysis of X-ray scattering data is discussed below; further detail is available elsewhere [2,22–24].

Before measuring the X-ray scattering from a sample, a dark frame measurement made. The X-ray shutter was closed and the detector signal recorded (I_{dark}), which allowed the inherent noise of the detector to be acquired. Additionally, an empty chamber measurement was made to determine the amount of secondary scattering from the ESL chamber (I_{empty}). Afterwards, the X-ray scattering intensity from the sample was measured (I_{sample}) and the intensity was corrected by subtracting the measured background (Eq. 2.4):

$$I_{corrected} = \Gamma\left(I_{sample} - I_{background}\right) \tag{2.4}$$

where Γ is the gain map of the detector, $I_{background} = I_{dark} - (I_{empty} - I_{empty,dark})$, and $I_{empty,dark}$ is the measured intensity with no sample in the beam and the X-ray shutter closed. As the liquids were isotropic, homogeneous, and azimuthally symmetric, an average was taken over the azimuthal angle φ to reduce the error in the diffraction measurements. The averaged corrected intensity was then converted to momentum transfer, q, via:

$$\boldsymbol{q} = \boldsymbol{k}_i - \boldsymbol{k}_f; |\boldsymbol{q}| = \frac{4\pi \sin\theta}{\lambda} \tag{2.5}$$

where $\boldsymbol{k}_i$ and $\boldsymbol{k}_f$ are the incident and scattered photons vectors, λ is the incident X-ray wavelength and θ is the scattered angle. As illustrated in Fig. 2.8, the measured intensity is in polar coordinates; however, the intensity must be corrected to solid angle units to arrive at the coherent scattering cross section, which will allow for *S(q)* and *g(r)* to be determined. The tilt correction, performed by calibrating the detector with a silicon standard, also maps the polar coordinates to the respective solid angle coordinates.

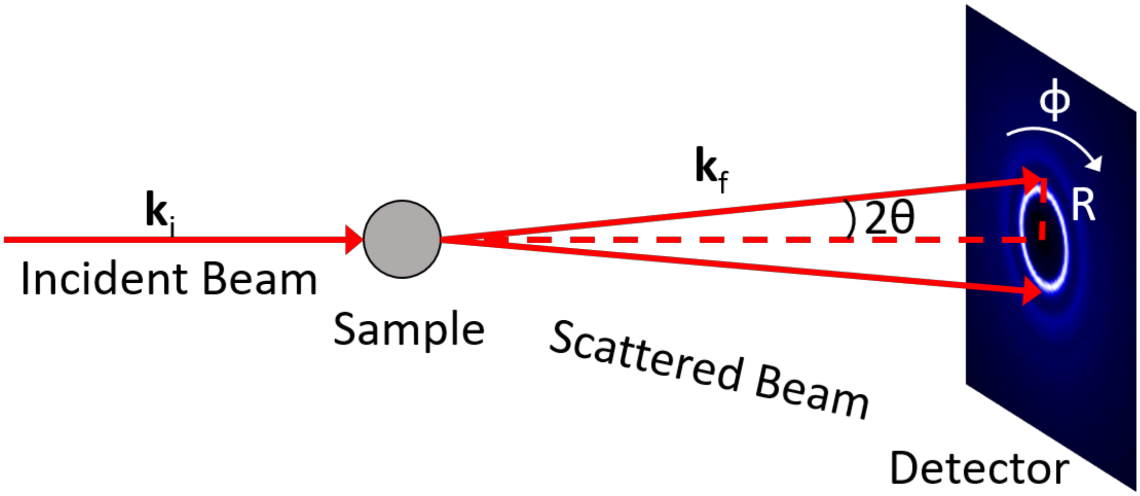

Figure 2.8: A cartoon representation of the transmission geometry for scattering experiments. Overlaid on the right is scattering data acquired during BESL2016 for $Zr_{75.5}Pd_{24.5}$.

Several other corrections must be made to the measured intensity. To account for polarization of the X-rays scattered from the sample, a polarization correction function *P*, containing both the angle of polarization of the incident beam and the fraction of polarization at that angle, was applied to the measured intensity. To account for the attenuation by the sample—also known as the self-absorption, *V/V'*—another correction accounting for the radius of the incident beam, the sample attenuation coefficient, and the sample size, was also applied. Self-scattering of the sample was considered by calculating the ratio of the secondary scattering to the primary scattering, I_2/I_1, which is related to the atomic numbers of the elements composing the alloy. Other corrections, such as the Compton scattering (n^{inc}), oblique incidence (*O*), sample fluorescence (*F*), and geometric corrections accounting for the difference between polar and solid angle units (*dA/dΩ*) were applied as well. The coherent scattering cross section can be calculated by integrating the corrected intensity and accounting for the corrections detailed above:

$$\frac{d\sigma_c}{d\Omega} = N \oint d\phi \frac{I_{corrected} \times \frac{dA}{d\Omega}}{\frac{V'}{V} OP \times \left(1 + \frac{I_2}{I_1}\right)} - n^{inc} - F \tag{2.6}$$

These correction factors are discussed in detail elsewhere [2,22]. Once the scattering cross section has been calculated, the structure factor *S(q)* is obtained from:

$$S(q) = \frac{\frac{d\sigma}{d\Omega} + \langle f(q)\rangle^2 - \langle f(q)^2\rangle}{\langle f(q)\rangle^2} \tag{2.7}$$

where *f(q)* is the atomic form factor and $\langle f(q)\rangle$ is the average atomic form factor over all atomic species, which are outlined elsewhere [25]. The pair distribution function can then be obtained via a Fourier transform of *S(q)*:

$$g(r) = 1 + \frac{1}{2\pi^2 r \rho_0} \int_0^\infty q(S(q) - 1) \sin(qr)\, dq \tag{2.8}$$

Dr. Mark Johnson wrote an in-house LabVIEW program to correct for excess curvature in *S(q)* that prevented it from oscillating smoothly around a value of one at high-q. Further descriptions of those corrections are discussed elsewhere [22].

2.5 Nucleation Measurements in ESL and EML

2.5.1 Maximum supercooling studies in ESL

To generate a statistical distribution of supercooling measurements for use with the Skripov method, several hundred thermal cycles were performed. Samples were loaded into a stainless-steel carousel, which was an improvement over the previously used brass carousel. With the brass carousel, a minimum pressure of approximately 2-4x10^{-7} Torr was achievable due to the emission of zinc from brass in high-vacuum. With the stainless-steel carousel, and the removal of all brass components from the chamber, a minimum pressure of 10^{-8} Torr was easily achievable. This pressure was chosen to minimize oxygen contamination in the sample. It was found that performing these experiments at higher pressures (10^{-7} Torr) resulted in a decay in the supercooling, indicating contamination, as will be outlined later in Section 2.6.

The samples were levitated and heated above the liquidus temperature as many times as possible—at least 200 times for a single sample—to generate a distribution of maximum supercooling temperatures. In practice, the first 25-50 cycles of the run were ignored due to sample conditioning, whereby contamination at the surface and gas in the grain boundaries was gradually evaporated. Once a consistently achievable maximum supercooling was reached, at least 200 cycles were performed. The target heating temperature was typically 150 °C above the liquidus temperature once the sample had been properly conditioned. Depending on the sample, its cooling rate, and how deeply it supercooled, gathering enough supercooling data could take between 2.5 to 6 hours. While Skripov proposed 100 cycles would be sufficient for his technique [26], more data were taken to ensure the best statistics possible, especially since significant time was devoted to the initial slow heating of the sample. Care was taken to ensure samples with higher vapor pressures, like Cu or Pd based alloys, were not heated more than necessary to prevent mass loss and compositional shift in the alloy.

A laser power was chosen to minimize both cycle time and sample distortion. If the heating laser is not aimed perfectly at the center of the sample, then the radiation pressure will cause the sample to spin like a frictionless bearing. Over the course of every supercooling experiment, the originally nearly spherical samples were observed to stretch out slightly into ellipsoids. As an example, pure zirconium was the first sample studied as a proof of concept for this technique. Zirconium requires almost the entire 50W of laser power to melt. It was observed that, after roughly 75 cycles, the once spherical sample transformed into an ellipsoid with a significant semi-major axis to semi-minor axis ratio, much like a football. It was found that the sample could no longer be heated and supercooled reliably in this shape, likely due to both misalignment with the laser and the large thermal gradient in the sample. The zirconium case represents the extreme; every sample studied in this dissertation did not demonstrate such significant distortion that its supercooling behavior was impacted.

If the maximum supercooling for a sample decreased during the experiment, or if there was concern about sample evaporation and compositional shift, another sample from the same master ingot was loaded and processed. The supercooling measurements from multiple samples could be normalized together to account for small variations in their volume, as will be demonstrated later in the case of $Ti_{39.5}Zr_{39.5}Ni_{21}$ [27]. This enabled a larger distribution of measurements to be studied, while simultaneously ensuring every cycle was repeatable and free of contamination and other artifacts.

2.5.2 Nucleation measurements using the Electromagnetic Levitation facility on-board the International Space Station

The primary reason for studying nucleation in a microgravity environment is to understand the role of diffusion on nucleation. Under terrestrial conditions, liquids undergo gravitational stirring, thus masking characteristic diffusion effects. However, even on the EML-ISS, a small positioner voltage is required to maintain the sample position, which induces a small amount of stirring. In addition, when the EML payload was launched to the ISS, some distortion occurred to the rf-coil, requiring higher positioner voltages than expected to be used to maintain sample position. However, even though stirring cannot be eliminated, the EML can still be used to control stirring in the liquid based on the chosen positioner and heater parameters. Future studies on the EML will gradually increase the amount of stirring to identify the effects of diffusion on nucleation. While the idealized case cannot be achieved, an approximately “minimally-stirred” case is feasible, which can then be compared to the “highly-stirred” case.

Nucleation measurements can be performed under high vacuum conditions (10^{-7} Torr) or in high-purity gas environments. Due to potential contamination in the gas, which can introduce heterogeneous nucleation sites in the sample, high vacuum conditions are preferred for nucleation measurements. However, processing under high vacuum conditions also leads to more deposition onto the coil, limiting its lifetime. As such, some nucleation studies in high purity argon and helium atmospheres were performed. While nucleation in a gas environment is likely heterogeneous, the kinetic processes are the same as for homogeneous nucleation. It is possible that diffusion effects on the nucleation rate for minimally and maximally stirred cycles can still be observed.

In the ISS experiments, the sample was quickly heated to a target temperature, typically 200 °C above the liquidus temperature. Then, the heater current was reduced to zero and the positioning voltage was reduced to a designated minimum value, which allowed the liquid to cool until it crystallized. In some cases, the heater voltage remained on at a small value. While this does slow the cooling rate down, the experiments and analysis discussed later have shown that the cooling rate does not necessarily impact the maximum achievable supercooling for clean samples.

2.6 Non-linear, least-squares fitting of supercooling data

As discussed earlier, the probability density function derived by Skripov [26] can be applied via a non-linear, least-squares fitting routine to the distribution of supercooling measurements. The routine of choice is the Levenberg-Marquart [28,29] algorithm, which is implemented within Python's "scipy.optimize curve_fit" routine. The general purpose of the algorithm is to iteratively reduce the sum of the squares of the error between the function being fit and the measured data. While other publications in the literature do not discuss the specifics of the fitting routine [30–32], the general consensus is to use the probability density function derived in Chapter 1 (Eq. 1.39). The procedure followed is to (i) let A^* and W^* be the fit parameters, (ii) assume a standard approximation for the temperature dependence of the driving free energy, and (iii) assume a temperature dependence of the interfacial free energy.

The Python fitting algorithm was checked for both mathematical and computational accuracy using published data on supercooled zirconium (Klein *et. al.* [33]). Following Klein *et. al.*, a linear temperature dependence was assumed for σ and the Spaepen-Thompson approximation [34] for the driving free energy was used. The value of A^* and W^* obtained from the fitting algorithm were 10^{42} $(m^3s)^{-1}$ and 74 k_BT respectively, within error the values reported by Klein *et. al.*, 10^{42} $(m^3s)^{-1}$ and 75 k_BT [33]. In addition, the algorithm gave a fit distribution curve (Fig. 2.9) that was in agreement with that obtained by Klein *et. al.*

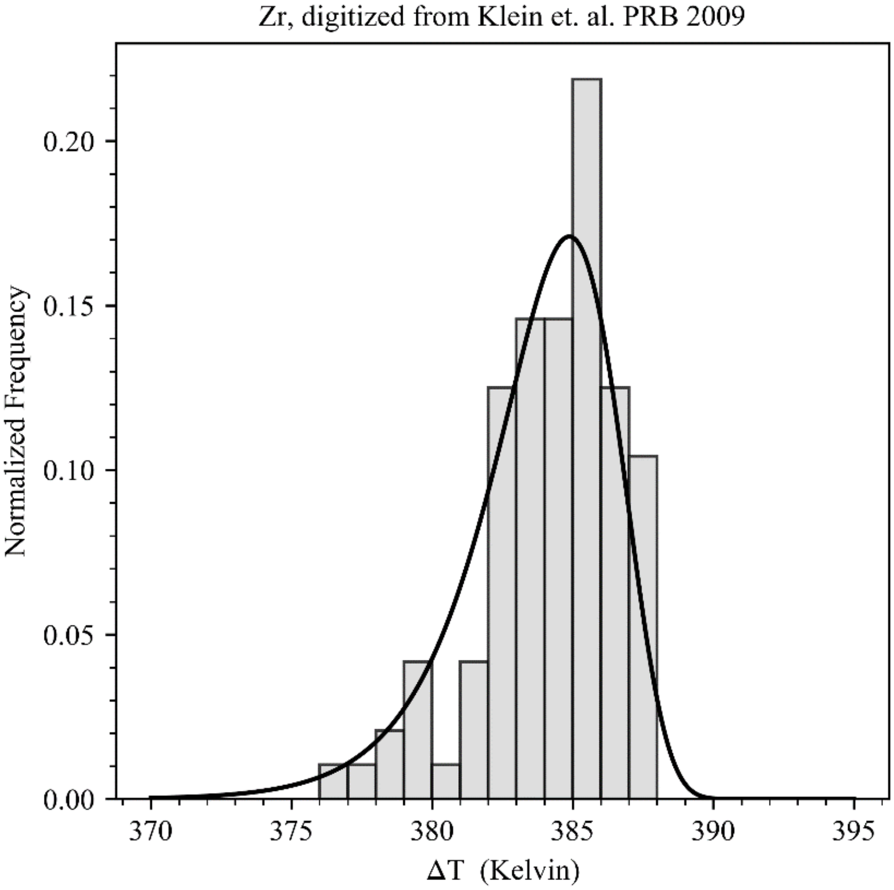

Figure 2.9: A reproduced distribution of Zr supercooling temperatures with the fitted probability density function calculated using the in-house curve fitting Python program. Comparing with [33] shows that the curve fitting program produces similar results and a similar best-fit curve as reported in the literature.

As a further check, the temperature achieved during each supercooling cycle was examined as a function of the cycle number, which is a proxy for time since the cycles were obtained consecutively. The first 25 to 50 cycles of the experiment were excluded from the analysis since the measured supercooling generally improved during these cycles until reaching the maximum value. As already mentioned, the effects of this conditioning have been observed and documented in other ESL studies [14]. Once the sample reached the maximum supercooling, the remaining cycles were scrutinized for deviations from the mean by fitting a line to the distribution of supercoolings and examining the R-value of the fit. If the sample became contaminated during processing, either by poor vacuum conditions or by dropping onto the bottom electrode while liquid, subsequent cycles would show a decrease in the amount of supercooling, giving a time-dependent supercooling and resulting in a larger R-value (nominally 0.15 or greater). This led to a less-sharply peaked supercooling distribution and resulted in fitted nucleation parameters that are more representative of heterogeneous nucleation. Ideally, the supercooling behavior should not change at all during the entirety of the experiment, which results in a R-value close to zero and a narrow, sharply peaked supercooling distribution. However, even a R-value close to zero must be checked for statistical significance by calculating the p-value and comparing it against a pre-determined significance level, typically 0.05. Since the dataset typically contained more than 200 measurements, even small R-values could result in a statistically significant relationship between supercooling and cycle number ($p < 0.05$). These points are illustrated in Fig. 2.10 using supercooling data from $Ti_{40}Zr_{30}Ni_{30}$, which will be discussed in further detail in Chapter 4. The two distributions shown correspond to the actual data (Fig. 2.10.b) and to the case where a small decay was applied to artificially induce a relationship between supercooling and cycle number (Fig. 2.10.c). The artificial decay in (c) resulted in a larger R-value and a calculated p-value < 0.0001, indicating a statistically significant relationship. In contrast, the original data in (b) yields a calculated p-value = 0.35, which is larger than the preset significance level of 0.05 and suggests no significant statistical relationship between the two quantities. For the case where the decay was applied, the resulting probability density curve was shifted to the left and was less sharply peaked

(Fig. 2.10.a). While introduced artificially for illustration, a similar decay was observed in the proof-of-concept studies on pure zirconium, likely due to poor vacuum conditions caused by the presence of brass within the ESL chamber.

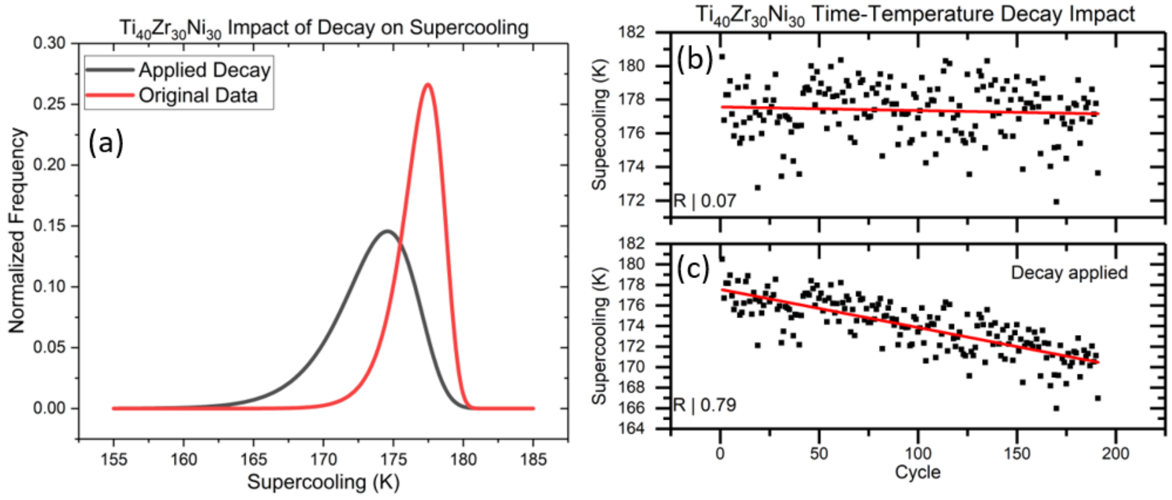

Figure 2.10: (a) A representation of the impact of contamination on the probability density function and (b,c) the time-temperature data, with (b) being original data and (c) having an artificial decay applied. For this reason, the data were checked to ensure reproducibility; otherwise, the experiment is repeated with cleaner samples and a better sample processing environment.

Since Eq. 1.39 represents a probability density function, the histogram of supercooling measurements must be normalized so that the total probability equals one. As shown in the dissertation of Dr. Melissa Wert [35], a bin-width of 1.0 K was used to minimize the error in the calculated nucleation parameters. This was found by performing a curve fitting routine on two unique zirconium supercooling datasets with very similar distributions and nucleation parameters. It was found that performing curve fitting routines with bin-widths larger or smaller than 1.0 K resulted in systematically larger differences between the nucleation parameters of the two sets. As such, a bin width of 1.0 K was chosen to ensure fair comparison of parameters and minimize systematic differences between datasets. Also, as nucleation obeys Poisson statistics, the standard error was defined as the square root of the normalized frequency for the respective bin. This meant data further from the mean of the distribution was less important in the fitting. As a result, the contribution of one or a few scattered data points far away from the mean of the distribution were typically ignored or heavily discounted by the algorithm due to their higher relative error. This follows the procedure outlined in the thesis of Dr. Melissa Wert from Vanderbilt University [35]. Choosing a bin-width of 1.0 K sometimes resulted in bins with zero counts; a filter was applied to remove these bins from the fit. Since these bins typically occurred in the left-hand tail of the distribution far from the mean, they did not significantly impact the accuracy of the fit.

Numerical overflows often occurred when fitting to the regular form of the supercooling distribution, which either delayed or outright prevented convergence of the fit. The natural logarithm of the probability density was instead fit to the distribution of supercooling using the definition of the steady-state nucleation rate (Eq. 1.21):

$$\ln(\omega) = \ln\left(\frac{A^* V}{\dot{T}}\right) - \frac{W^*}{k_B T} - \frac{V}{\dot{T}} \int_{T_u}^{T_l} A^* \exp\left(-\frac{W^*}{k_B T}\right) dT \tag{2.9}$$

where A^* is the nucleation pre-term normalized by the viscosity, V is the volume nucleated, $\dot{T}$ is the cooling rate, W^* is the critical work of cluster formation, T_u is the maximum supercooling temperature achieved, T_l is the liquidus temperature, and k_B is Boltzmann's constant. It is important to note that the integral must be performed at every supercooling temperature measured. Equation 2.9 contains three parts; the probability density was obtained by taking the exponential of the sum of these parts. Finally, following Skripov, a constant cooling rate was assumed (i.e., temperature is linearly related to time). While the accuracy of the assumption can be argued, it significantly simplified the calculation of the probability density. Future work could explore the effects of a nonlinear cooling rate on the fits to the supercooling distribution.

2.7 References

1. Pueblo, C. E. Ground and Flight Based Studies of Nucleation and Thermophysical Properties in Metallic Glass Forming Systems. (Washington University In St. Louis, 2016).

2. Bendert, J. C. Thermophysical and Structural Measurements of Liquid Metallic Alloys Using Electrostatic Levitation. (Washington University in St. Louis, 2013).

3. Mauro, N. A. & Kelton, K. F. A highly modular beamline electrostatic levitation facility, optimized for in situ high-energy x-ray scattering studies of equilibrium and supercooled liquids. *Rev. Sci. Instrum.* **82**, 035114 (2011).

4. Meister, T., Werner, H., Lohoefer, G., Herlach, D. M. & Unbehauen, H. Gain-scheduled control of an electrostatic levitator. *Control Eng. Pract.* **11**, 117–128 (2003).

5. Mauro, N. A. Structural and Thermophysical Property Studies of Metallic Liquids and Glasses Using the Beamline Electrostatic Levitation Technique. (Washington University In St. Louis, 2011).

6. Rustan, G. E. Electrostatic levitation studies of supercooled liquids and metastable solid phases. (Iowa State University, 2014).

7. Bendert, J. C., Pueblo, C. E., Veligati, S., Mauro, N. A. & Kelton, K. F. Temperature

calibration for optical pyrometry in containerless systems using differential scanning calorimetry: Application to Cu100−xZrx(x = 45–50). *Int. J. Thermophys.* **35**, 1687–1696 (2014).

8. Ashcraft, R. A. Linking Structure and Dynamics in Metallic Liquids: A Combined Experimental and Molecular Dynamics Approach. (Washington University in St. Louis, 2018).

9. Wunderlich, R. K. & Fecht, H. J. Modulated electromagnetic induction calorimetry of reactive metallic liquids. *Meas. Sci. Technol.* **16**, 402–416 (2005).

10. Seidel, A., Soellner, W. & Stenzel, C. EML - An electromagnetic levitator for the International Space Station. *J. Phys. Conf. Ser.* **327**, (2011).

11. Lohöfer, G. High-resolution inductive measurement of electrical resistivity and density of electromagnetically levitated liquid metal droplets. *Rev. Sci. Instrum.* **89**, (2018).

12. DLR. https://129.247.113.56:8080/hypertest/projects/.

13. Chung, S. K., Thiessen, D. B. & Rhim, W. K. A noncontact measurement technique for the density and thermal expansion coefficient of solid and liquid materials. *Rev. Sci. Instrum.* **67**, 3175–3181 (1996).

14. Bendert, J. C. & Kelton, K. F. Containerless measurements of density and viscosity for a Cu48Zr52 liquid. *Int. J. Thermophys.* **35**, 1677–1686 (2014).

15. Bradshaw, R. C., Schmidt, D. P., Rogers, J. R., Kelton, K. F. & Hyers, R. W. Machine vision for high-precision volume measurement applied to levitated containerless material

processing. *Rev. Sci. Instrum.* **76**, 1–8 (2005).

16. Lamb, H. On the Oscillations of a Viscous Spheroid. *Proc. London Math. Soc.* **s1-13**, 51–70 (1881).

17. Blodgett, M. E., Egami, T., Nussinov, Z. & Kelton, K. F. Proposal for universality in the viscosity of metallic liquids. *Sci. Rep.* **5**, 1–8 (2015).

18. Kivelson, D., Kivelson, S. A., Zhao, X., Nussinov, Z. & Tarjus, G. A thermodynamic theory of supercooled liquids. *Phys. A Stat. Mech. its Appl.* **219**, 27–38 (1995).

19. Nussinov, Z. Avoided phase transitions and glassy dynamics in geometrically frustrated systems and non-Abelian theories. *Phys. Rev. B - Condens. Matter Mater. Phys.* **69**, (2004).

20. Tarjus, G., Kivelson, S. A., Nussinov, Z. & Viot, P. The frustration-based approach of supercooled liquids and the glass transition: A review and critical assessment. *J. Phys. Condens. Matter* **17**, (2005).

21. Bendert, J. C., Mauro, N. A. & Kelton, K. F. Pair distribution function analysis of X-ray diffraction from amorphous spheres in an asymmetric transmission geometry: Application to a Zr 58.5Cu15.6Ni12.8Al10.3Nb 2.8 glass. *J. Appl. Crystallogr.* **46**, 999–1007 (2013).

22. Johnson, M. L. Structural Evolution, Chemical Order, and Crystallization of Metallic Liquids and Glasses. (Washington University in St. Louis, 2015).

23. Egami, T. & Billinge, S. J. L. *Underneath the Bragg peaks: structural analysis of complex materials*. **16**, (Newnes, 2012).

24. Vogt, A. J. Structural Studies and Chemical Ordering in Metallic Liquids and Glasses Using Electrostatic Levitation. (Washington University in St. Louis, 2014).

25. Waasmaier, D. & Kirfel, A. New analytical scattering-factor functions for free atoms and ions. *Acta Crystallogr. Sect. A* **51**, 416–431 (1995).

26. Skripov, V. P. Homogeneous Nucleation in Melts and Amorphous Films. *Curr. Top. Mater. Sci.* **2**, 328–378 (1977).

27. Sellers, M. E., Van Hoesen, D. C., Gangopadhyay, A. K. & Kelton, K. F. Maximum supercooling studies in $Ti_{39.5} Zr_{39.5} Ni_{21}$, $Ti_{40} Zr_{30} Ni_{30}$, and $Zr_{80} Pt_{20}$ liquids—Connecting liquid structure and the nucleation barrier. *J. Chem. Phys.* **150**, 204510 (2019).

28. Levenberg, K. A method for the solution of certain non-linear problems in least squares. *Q. Appl. Math.* **2**, 164–168 (1944).

29. Marquardt, D. W. An algorithm for least-squares estimation of nonlinear parameters. *J. Soc. Ind. Appl. Math.* **11**, 431–441 (1963).

30. Morton, C. W., Hofmeister, W. H., Bayuzick, R. J., Rulison, A. J. & Watkins, J. L. The kinetics of solid nucleation in zirconium. *Acta Mater.* **46**, 6033–6039 (1998).

31. Hofmeister, W. H., Morton, C. W. & Bayuzick, R. J. Monte Carlo testing of the statistical analysis of nucleation data. *Acta Mater.* **46**, 1903–1908 (1998).

32. Wert, M. J., Hofmeister, W. H. & Bayuzick, R. J. Effect of dilute amounts of oxygen solute on nucleation of zirconium. *J. Appl. Phys.* **93**, 3643–3651 (2003).

33. Klein, S., Holland-Moritz, D. & Herlach, D. M. Crystal nucleation in undercooled liquid

zirconium. *Phys. Rev. B* **80**, 2–5 (2009).

34. Thompson, C. V & Spaepen, F. On the Approximation of the Free Energy Change on Crystallization. *Acta Metall.* **27**, 1855 (1979).

35. Wert, M. J. Investigation of Effects of Dilute Oxygen Solute on Nucleation of Zirconium. (Vanderbilt University, 2002).

Chapter 3: Nucleation and Stirring Measurements on-board the International Space Station

The data presented in this chapter were collected from the German Aerospace Center (Deutsches Zentrum für Luft- und Raumfahrt; DLR) *in Cologne Germany by Mark Sellers, Daniel Van Hoesen, Anup Gangopadhyay, and Julianna Schmitz. Data reduction was performed by both Mark Sellers and Daniel Van Hoesen while stirring calculations were performed by Gwendolyn Bracker and Robert Hyers at the University of Massachusetts, Amherst.*

3.1 Introduction

In most experimental studies of supercooled liquids, it is assumed diffusion rates are sufficiently fast such that only the interfacial attachment rate needs to be considered. As such, the steady-state solution for both the Classical Nucleation Theory (CNT) and Diffuse Interface Theory (DIT) should reasonably describe the nucleation kinetics between the liquid and crystal phases. However, a diffusion-influenced nucleation rate has been predicted [1]. With the removal of gravitational and Marangoni convection in the liquid, the diffusion rate may become comparable to the interfacial attachment rate. Because the classical theory of nucleation is inherently interface-limited, it fails to fully describe nucleation that relies on slow, long-range diffusion effects, as demonstrated in studies of oxygen precipitation in silicon [2–4]. It may also be possible to detect diffusion-limited crystal nucleation in quiescent liquids. Further exploration of a theory coupling diffusion and interfacial attachment rates may provide more insight into nucleation.

To further probe the new “Coupled-Flux” theory of nucleation, studies of metallic alloys using the Electromagnetic Levitator (EML) on-board the International Space Station (ISS) were proposed. As reported in the proposal’s Science Requirement Document (SRD):

> “convection in the ground-based electrostatic levitation (ESL) experiments contaminates the diffusion profile near nucleation clusters…possible studies of diffusion-induced nucleation on earth are restricted by convective flow.” [5]

In ESL processed liquids under terrestrial conditions, gravitational and Marangoni-induced convection contribute to stirring [5–7]. Gravitational convection is an unavoidable fact for ground-based studies of liquids. Marangoni-induced convection occurs due to surface tension gradients in the liquid induced by temperature variations across the sample [6]. In ESL, samples are usually heated with a single axial laser, generating large thermal gradients within the liquid due to the sample’s finite thermal conductivity. In practice, these gradients can be reduced by a tetrahedral arrangement of heating lasers to more uniformly heat samples [8]; however, this is beyond the scope of this research. Regardless, the calculated flow velocity of gravitational and Marangoni convection were found to be a factor of two larger than the maximum diffusion flow velocity [5]. To study these diffusion effects, gravitational and Marangoni convection must be reduced by modifying the sample processing environment.

In ground-based EML studies, stirring due to the electromagnetic force is introduced, in addition to the already existing Marangoni and gravitational contributions [7]. However, since samples are more uniformly heated in EML, the overall impact of Marangoni convection is reduced. Processing on earth requires overcoming the sample’s gravitational attraction, which can maintain the sample above its liquidus temperature and prohibit deep probing of the supercooled liquid. However, processing in microgravity environments with EML allows smaller heating and positioning currents to be used in the experiments, which enables deeper supercooling to be achieved. Supercooling is further enhanced by using separate dipole and quadrupole fields for heating and positioning the sample. The smaller currents used in microgravity and more uniform heating within EML also reduce the stirring contributions of Marangoni, gravitational, and electromagnetic convection. With these improved processing conditions, computational fluid dynamic models of liquids undergoing EML processing have shown that the calculated flow velocity from stirring can be nearly two orders of magnitude smaller than the predicted diffusion flow velocity [5]. As such, if diffusion effects are important in nucleation, they should be observable within the EML.

The data were analyzed and interpreted within several of the theories outlined earlier, but the main purpose of the ISS experiments is to "measure, in the absence of gravitationally-induced flow, the effects of alloy composition on nucleation and to compare with predictions from the Coupled-Flux model for nucleation [5]." Since the CNT applies to cases where the rate-limiting step is interfacial attachment to the cluster, a deviation between its predictions and those from the Coupled-Flux theory is expected. Analysis of the results from ground-based ESL maximum supercooling experiments performed using a statistical treatment of the classical theory [9] have shown that the nucleation parameters A^* and W^* negligibly change with maximum supercooling temperature. Therefore, a significant temperature dependence in nucleation parameters under different stirring conditions may serve as a signal of departure from the classical theory and as a signature for the effects predicted by the Coupled-Flux theory.

To more fully explore the impact of long-range diffusion on nucleation, the Coupled-Flux theory was proposed, which considers both interfacial cluster attachment rates and diffusion rates around the neighborhood of the cluster [10–12]. This is represented in Fig. 3.1, which has been reproduced from [10] with permission from Elsevier.

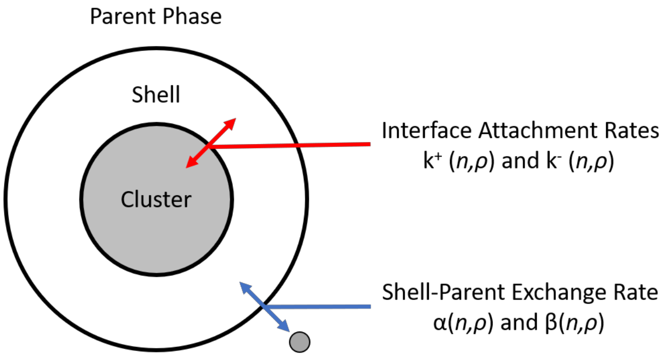

Figure 3.1: A schematic illustration of the Coupled-Flux model for nucleation, showing the interfacial attachment rates in red, the shell-parent exchange rates in blue, and the location of the cluster, shell, and parent phase. Reproduced with permission from Elsevier from [10].

In general, clusters that are smaller than the critical size are biased towards dissolving [1]. Because of this, the Coupled-Flux model predicts that the local composition around a sub-critical cluster can be higher in the species nucleating than in the parent phase. Clusters larger than the critical size are biased towards growth, which causes the concentration of the species nucleating to be depleted in the neighborhood of the nucleating cluster. In diffusion-limited systems, the processes in the Coupled-Flux model can significantly slow down the nucleation and growth of a new phase. In cases where diffusion is not the rate limiting step, such as in highly stirred liquids, the Coupled-Flux theory recovers the predictions of the CNT [13].

The calculations performed within the classical theory can be interpreted by the Coupled-Flux theory as well. Russel and Kelton [10,12] have shown that the steady-state nucleation rate equation from the Coupled-Flux theory has the same general form as that of the classical theory. Kelton further showed that a simple scaling of the classical theory by the ratio of the minimal forward diffusion and growth rates at n^* can result in a good approximation of the steady-state nucleation rate predicted by the Coupled-Flux theory, as outlined in Eq. 3.1. In general:

$$I_{CF}^{ST} \approx \frac{\alpha(n^*,0)}{k^+(n^*,1)} I_{class}^{ST} \tag{3.1}$$

where I_{CF}^{ST} is the steady-state nucleation rate for the Coupled-Flux theory, I_{class}^{ST} is the corresponding steady-state nucleation rate for the classical theory, $\alpha(n^*, 0)$ is the rate at which one atom or molecule diffuses into the nearest neighbor shell (since α is a function of $\rho - 1$, where ρ is defined below) of a cluster of size n^* from the surrounding material, and $k^+(n^*,1)$ is the forward rate of attachment of one atom from the shell onto the cluster of size n^* [10,12]. From [13], the rates have the following forms (Eq. 3.2a, 3.2b):

$$\alpha(n,\rho-1) = \xi\rho\frac{D}{\lambda^2}\left(\frac{\rho_n^m-\rho+1}{\rho}\right)^{1/2}\left(\frac{N_0}{N_s-N_0}\right)^{1/2} \tag{3.2a}$$

$$k^+(n,\rho) = \rho\frac{6D'}{\lambda^2}\exp\left(-\frac{\delta W_n}{2k_BT}\right)G(n,\rho) \tag{3.2b}$$

where D is the diffusion coefficient in the parent phase, D' is an effective diffusion rate governing interfacial attachment, N_0 is the number of molecules, N_s is the number of sites, $\bar{v}$ is the molecular volume, λ is the jump distance (on the order of an Angstrom), $\delta W(n^*)$ is the difference in the work of cluster formation between a cluster of size n^* and n^*+1, ρ is the number of solute molecules, $G(n,\rho)$ is a correction factor accounting for entropy changes in the shell and parent phase as particles attach to the cluster, and ξ is a constant accounting for atoms not immediately equilibrating to the randomly dispersed parent phase after leaving the shell. ξ scales with dilution and has the form (Eq. 3.3):

$$\xi = \frac{(4\pi)^{2/3}}{2}(3\bar{v})^{1/3}\lambda^2N_0^{1/2} \tag{3.3}$$

Reasonable choices of parameters in Eq. 3.2a, 3.2b, and 3.3 such as taking N_0 to be on the order of Avogadro's number, N_s is a multiple of N_0, and $\delta W(n^*)$ is 0, in addition to already published results [10], suggest that the difference in steady-state nucleation rate between the CNT and Coupled-Flux theory is on the order of 5 to 10 orders of magnitude. Scaling by α allows the slower kinetics to be factored into the nucleation rate because it contains terms relating to diffusion and concentration. While the Coupled-Flux model was first developed for the case of precipitation from a dilute system, it should apply in all cases where diffusion becomes dominant, although the deviation from the predictions of the classical theory may be significantly smaller.

To quantify whether diffusion impacted the observed nucleation events, the shear rate must be determined from computational fluid dynamics simulations. These calculations were performed by our collaborators Gwendolyn Bracker and Bob Hyers at the University of Massachusetts, Amherst. The details of the simulation will follow in the methods section below. In practice, a predicted shear rate between 0.05 and 0.5 sec^{-1} is required to prevent critical nuclei and their diffusion fields from colliding within the liquid [5]. Under these conditions, it can be expected that the experiment probed the diffusion-limited nucleation regime in a quiescent liquid. Otherwise, particle collision or impingement of diffusion profiles inferred from higher shear rates may imply nucleation dominated by stirring.

3.2 Methods

Spherical samples with a diameter 6 – 6.5 mm of $Cu_{50}Zr_{50}$ and $Zr_{57}Nb_5Cu_{15.4}Ni_{12.6}Al_{10}$ (Vit106) were prepared according to the procedures outlined in Chapter 2. These samples were packaged and shipped to the European Space Agency (ESA) to be launched to the International Space Station and loaded into the batch-specific carousel.

Nucleation and stirring experiments in the EML can be performed in vacuum or in gas, either high-purity argon or helium; however, the best sample processing conditions are observed in high-vacuum, as even the highest purity gas can potentially contaminate the liquid samples. In a typical cycle, the positioner voltage was set to some value between 2.49 and 6.66 V, while the heater was typically set to a value around 5.00 V to heat the sample to a target temperature (usually T_l + 200 to 300 K). Upon reaching that temperature, the heater and positioner were set to minimum values to allow the sample to cool. The maximum supercooling temperature achieved before crystallization was recorded. The heater and positioner parameters at the onset of crystallization were also recorded. For some of the cycles shown below, the heater remained at a low value for the duration of the cooling process, which increased the stirring in the sample.

More recent nucleation studies on-board the ISS have slowly increased the positioner and heater currents to induce higher amounts of stirring. It should be noted that the EML is not performing at full capacity due to off-axis distortions in the coil during the launch of the facility to the ISS. As such, larger positioner and heater values are required to position and heat samples. Thus, the maximally quiescent conditions likely cannot be achieved. However, by systematically modifying the heater and positioner voltages, information about the impact of stirring on nucleation can be extracted. When only the position current is on as the liquid cools, stirring is minimized. However, when the heater and positioner are active during cooling, the liquid experiences more turbulent flow. A representation of these two cycles is shown in Fig. 3.2, where time, temperature, positioner current, and heater current are shown on the same plot.

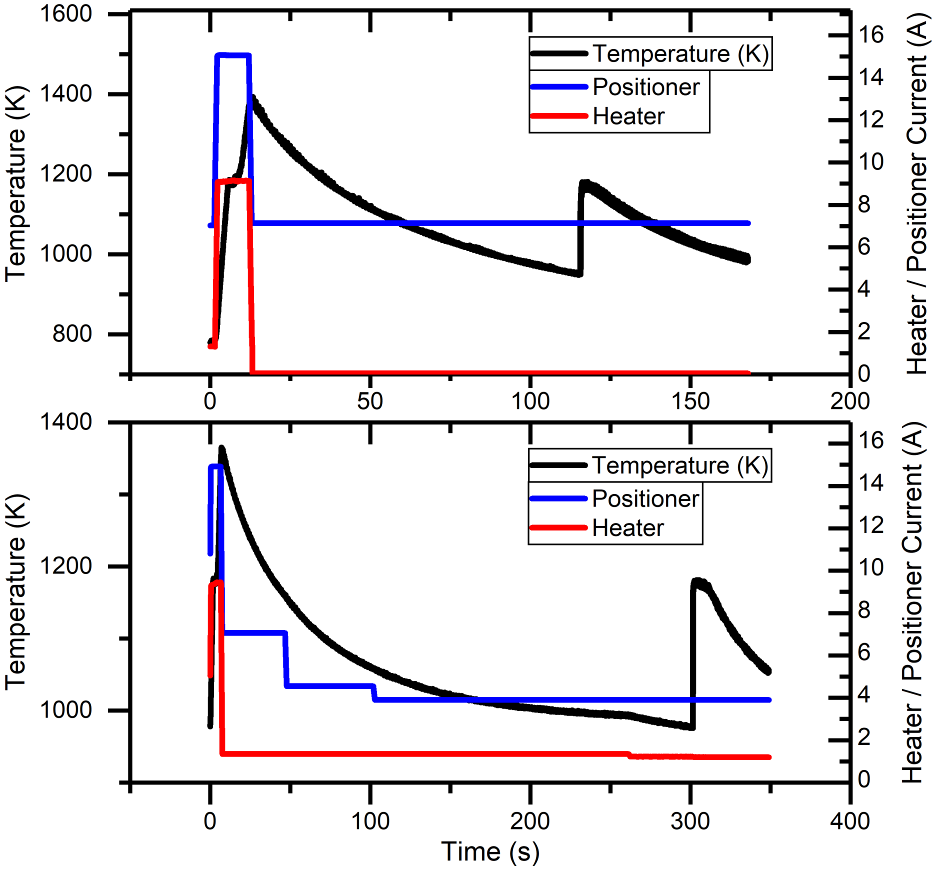

Figure 3.2: A representation of two cycles performed on $Cu_{50}Zr_{50}$. The top plot is a cycle where only the positioner was active during cooling, while the bottom plot is a cycle where the heater and positioner are both active during cooling. Simulations have shown that the data represented in the bottom plot result in more stirring of the liquid.

To model the flow inside these samples, simulations of stirring were performed by Gwendolyn Bracker of the Robert Hyers group at the University of Massachusetts, Amherst. The model setup is detailed in reports of the results of the simulations:

> “Models were run in ANSYS Fluent to calculate the velocity and shear-strain rate of the flow in the samples during cooling to the recalescence temperature for a variety of different experimental conditions. For each simulation, the electromagnetic force field was calculated based on the applied current, coil geometry, sample size, and sample conductivity. Computational fluid dynamics (CFD) simulations were used with the properties of the melt to calculate parameters of the flow.” [14]

Further information on the ANSYS Software may be found in the User Guide [15]. For these simulations, viscosity and density data were obtained from ground-based ESL thermophysical property measurements. The temperature, coil settings, and electrical resistivity data were acquired from the EML on-board the ISS. In general, when only the positioner was active during cooling, two loose vortices are observed in a hemispherical region of the sample. When the heater is turned on and left on during the cooling, four tight vortices are observed in the same hemispherical region. These points are illustrated in Fig. 3.3, which is a cartoon representation of the stirring calculation results performed on the entire liquid droplet.

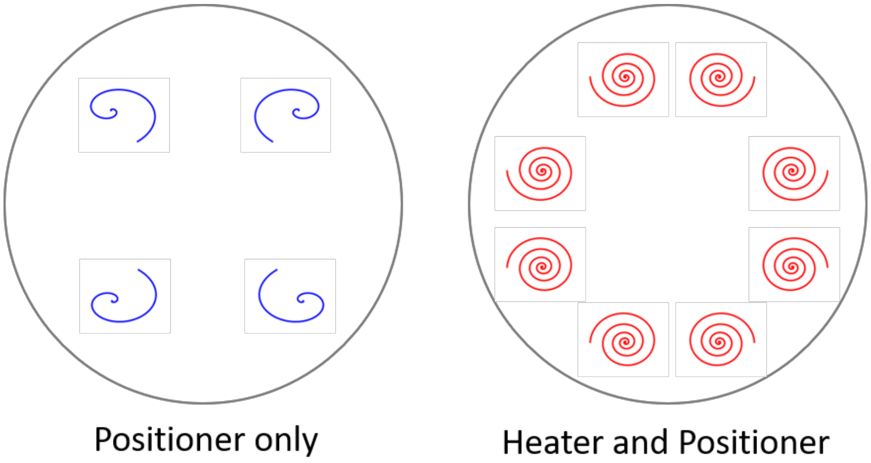

Figure 3.3: A cartoon representation of the results from the stirring calculations performed by Gwendolyn Bracker and Bob Hyers. Note that fewer and looser vortices are typically observed when only the positioner is active during sample cooling. When the heater is active, as seen on the right, more and tighter vortices are observed.

3.3 Analysis

The data were analyzed using the CNT and the DIT. By assuming that a single nucleation event will crystalize the entire liquid, we can define the following relation (Eq. 3.4):

$$I^{ST}vt = 1 \qquad (3.4)$$

where I^{ST} is the steady-state nucleation rate, v is the volume nucleated, and t is the time to nucleate. To account for the different cooling rates, a basic relation was defined as $t = T_u/\dot{T}$, where T_u is the maximum supercooling temperature and $\dot{T}$ is the cooling rate near the recalescence event. The cooling rate was measured close to the crystallization event by fitting a line to the time-temperature data. By substituting this relation into Eq. 3.4, together with the steady-state nucleation rate equation, the Turnbull approximation for the driving free energy, and assuming the nucleation pre-factor A^* to be 10^{39} $(\mathrm{m}^3\mathrm{s})^{-1}$ (the criterion proposed by Turnbull for homogeneous nucleation [16]) and the definition of W^*, the interfacial free energy σ can be written as (Eq. 3.5):

$$\sqrt[3]{\left(\frac{3k_BT_u}{16\pi}\right)\Delta g^2 \ln\left(\frac{A^*vT_u}{\dot{T}}\right)} = \sigma \qquad (3.5)$$

where N_A is Avogadro's Number, k_B is Boltzmann's Constant, Δg is the Gibbs free energy difference per unit volume ($\Delta\mu/\bar{v}$, where $\Delta\mu$ is the change in chemical potential per atom and $\bar{v}$ is the atomic volume), and σ is the interfacial free energy. The Turnbull approximation [17] ($\Delta G = \Delta H_f \Delta T/T_l$) was assumed as the definition of $\Delta\mu$. To explore the dependence of σ on $\dot{T}$, the other quantities in Eq. 3.5 were held constant. Figure 3.5 is a representative plot of σ versus $\dot{T}$ for some of the important cooling rates observed in these experiments. As seen in Fig. 3.4, the impact of cooling rate on σ decreases as the cooling rate increases. For larger and larger cooling rates, ranging from 20 K/s to 100 K/s, σ decreases by less than 0.001 J/m^2, indicating that the cooling rate has a minimal impact. In vacuum measurements, the measured cooling rates typically fall within the 1 K/s to 3 K/s range, which yields approximately a 0.5% decrease in σ. Similarly, changing the assumed value for A^* only changes the relative magnitude calculated for σ, it does not impact the overall temperature dependence. Other factors, such as the sample volume, maximum supercooling, and enthalpy of fusion have a stronger impact on the calculation of σ.

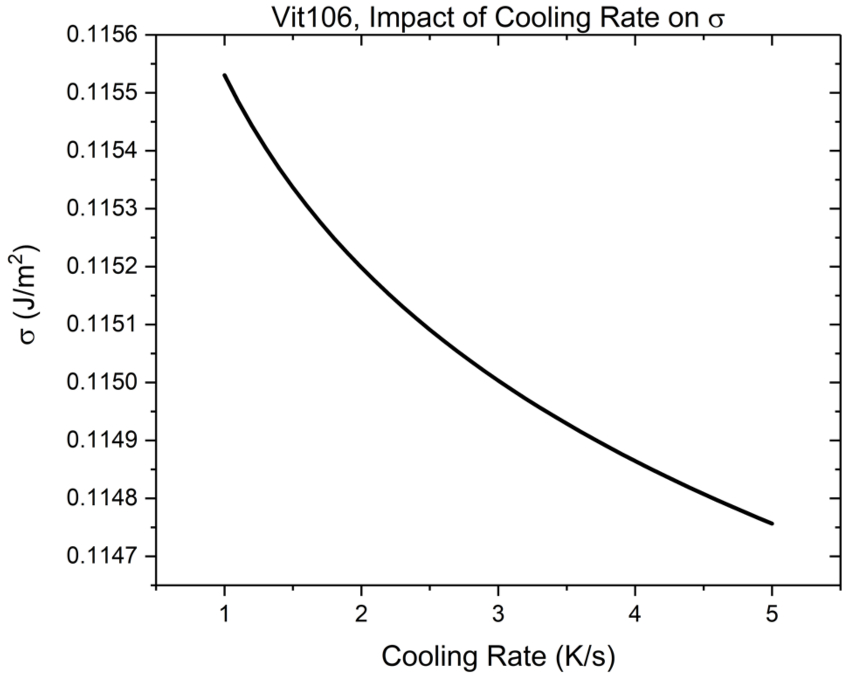

Figure 3.4: The calculated dependence between σ and cooling rate. As seen in the plot, the impact of cooling rate on σ is minimal. As cooling rate increases, the variation in σ becomes almost negligible.

As discussed earlier, the Coupled-Flux theory predicts a smaller magnitude of A^* for diffusion-limited nucleation. While there is no direct prediction of the impact of stirring on σ from the Coupled-Flux theory, it is still a pertinent nucleation parameter to investigate. Regardless, a calculation of σ will allow for reasonable values to be used in the calculation of A^* and to further investigate its dependence on the maximum supercooling and stirring. Choosing a different value of σ only changes the order of magnitude of A^*, it was not observed to change the temperature dependence or the scale of discrepancies outlined below. Using Eq. 3.4, the dependence of A^* on T_u (Eq. 3.6) is:

$$\frac{\dot{T}}{vT_u}\exp\left(\frac{16\pi}{3k_BT_u}\frac{\sigma^3}{\Delta g^2}\right) = A^* \tag{3.6}$$

The dependence of δ on the maximum supercooling can be evaluated from the definition of W^* from the DIT and Eq. 3.4. Much like Eq. 3.5, δ can be written as (Eq. 3.7):

$$\sqrt[3]{\left(\frac{k_BT_u}{\kappa\Delta g_0\psi(\eta)}\right)\ln\left(\frac{A^*vT_u}{\dot{T}}\right)} = \delta \tag{3.7}$$

where $\kappa = 4\pi/3$, $\Delta g_0 = \Delta h_0 - T\Delta s_0$, $\psi(\eta) = 2(1+q)\eta^{-3} - (3+2q)\eta^{-2} + \eta^{-1}$, $q = (1-\eta)^{-1/2}$, and $\eta = \Delta g_0/\Delta h_0$. The Turnbull Approximation was used for the definition of Δg_0. As described earlier, the definition of A^* in the Diffuse Interface Theory is the same as in the classical theory.

3.4 Results

Measurements on $Cu_{50}Zr_{50}$ were performed under high vacuum conditions across two nights. To account for day-to-day variation in maximum supercooling in the sample, the data from different days were analyzed separately. This is partly due to standard operating procedures for the EML since it must be refilled with an atmosphere of helium during the day when not in use. On Day 1, four cycles were performed with the heater set to a value of 1.25 A during cooling. The heater was turned off for the remaining four cycles while the positioner was varied slightly. On Day 2, the heater was not used, but the positioner was varied from a value of 3.88 to 6.66 volts. As can be seen in Fig. 3.5, the value of σ changes as a function of temperature, with larger maximum supercooling temperatures yielding a smaller value of σ. While the observed trends in

σ may be due to other effects and not kinetics, the calculation was useful to arrive at a reasonable value to calculate A^*. For $Cu_{50}Zr_{50}$, $\sigma = 0.132$ J/m^2 was chosen.

The data shown in Fig. 3.5 are tabulated at the end of this section in Table 3.1 and 3.2 for Day 1 and Day 2, respectively. Calculated stirring parameters from Bracker [18,19], such as the maximum flow velocity (v_{mf}) and shear-rate, along with voltage settings active during cooling are included to further quantify the flow within the liquids close to recalescence.

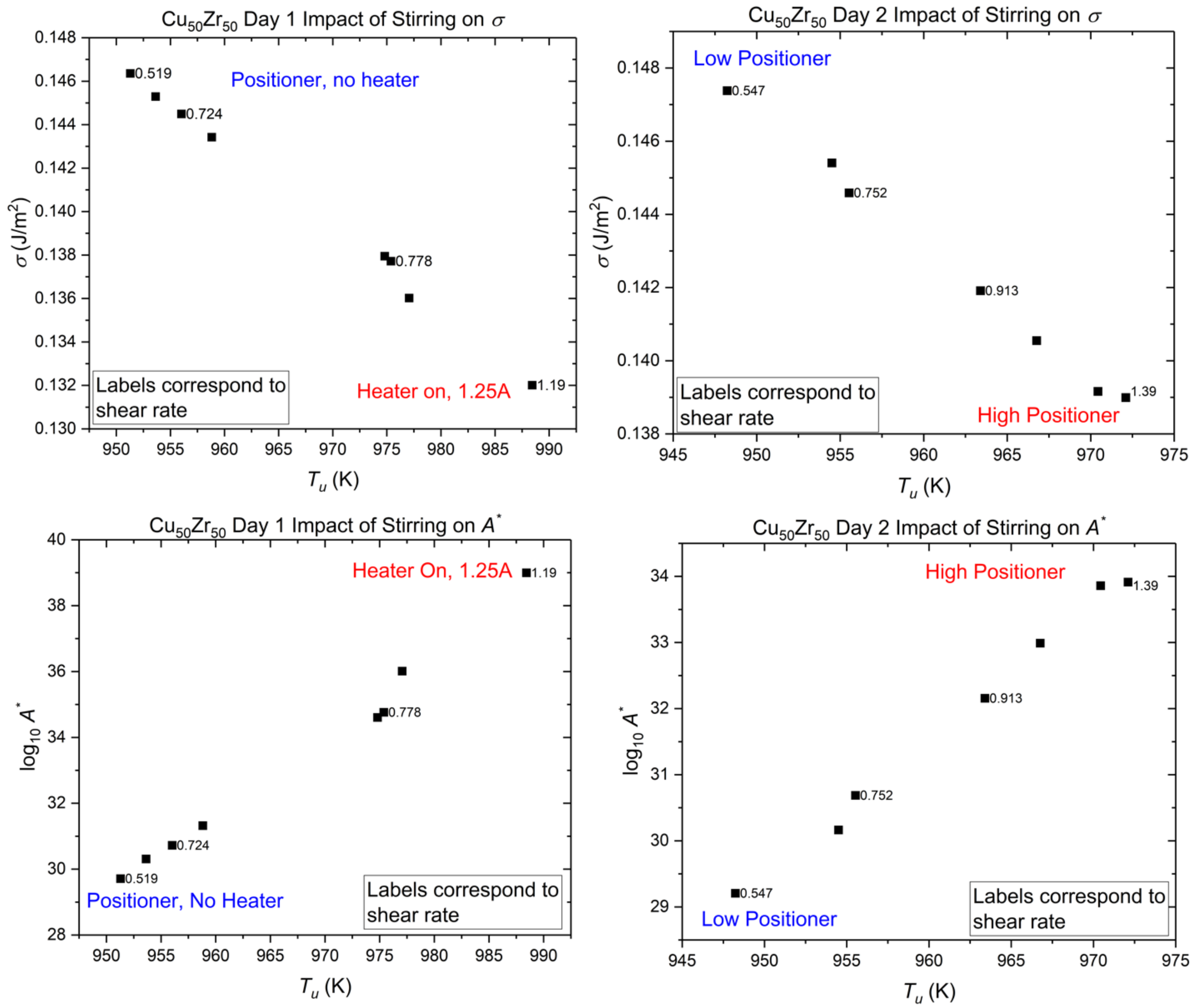

Figure 3.5: Plots of σ and A^* as a function of maximum supercooling temperature (T_u) for $Cu_{50}Zr_{50}$ cycles performed in high vacuum conditions across two different days. The plots are separated by day due to the refilling of the EML with helium when not in use.

A similar set of data was acquired and analyzed from Vitreloy 106. However, an atmosphere of high-purity helium was used and the data from one night of measurements were analyzed. During these experiments, the positioner voltage was set to a fixed value while the heater was either left on at 1.25A during cooling or turned off. Like $Cu_{50}Zr_{50}$, the value of σ is smaller when the heater is kept on during cooling, compared to cycles where only the positioner is left on, as seen in Fig. 3.6. A value of $\sigma = 0.103$ J/m^2 was used to calculate the value of A^*. The data shown in Fig. 3.6 are tabulated at the end of the section in Table 3.3 with parameters from Bracker [20].

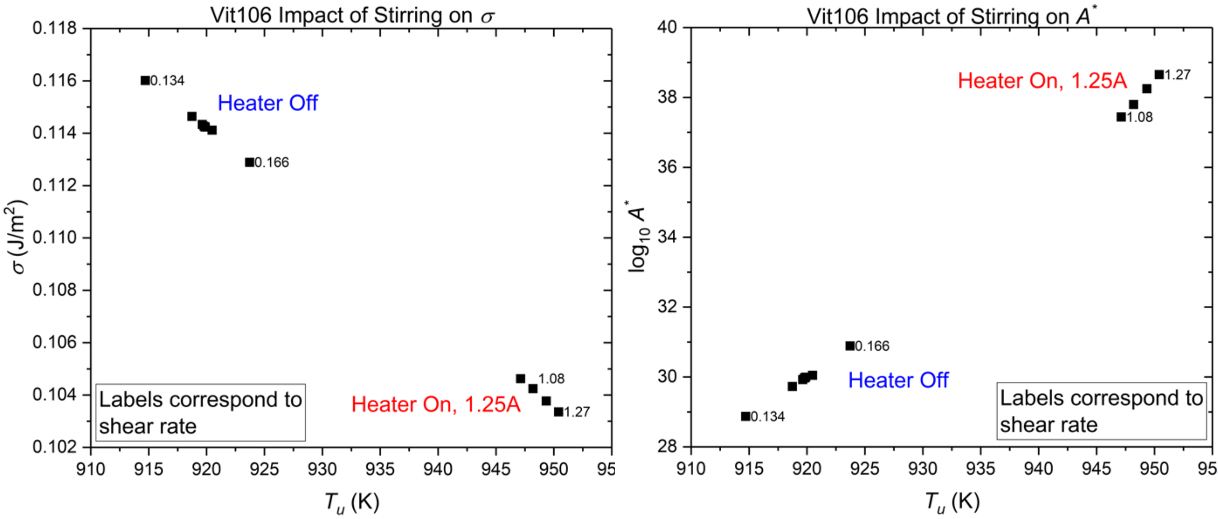

Figure 3.6: Plots of σ and A^* as a function of maximum supercooling temperature (T_u) for Vit106. These cycles were performed in a high-purity helium atmosphere, which drastically increased the cooling rate. Thus, these results should be even less affected by any cooling rate effects.

Since σ does not contain information about the kinetics of nucleation and the overall observed decrease is likely due to kinetic effects, the data were reanalyzed using the DIT through Eq. 3.7. Interestingly, turning the heater on resulted in a reduction of the value of δ, much like what was found from the CNT. This could suggest stirring brings atoms closer to the liquid-crystal interface and reduces the overall difference in entropy and enthalpy curves between these two phases, further implying a kinetic effect. It may also indicate that the DIT, while accounting for a more diffuse interface between the liquid and crystal, may not fully describe the kinetics of the system when diffusion becomes a dominant effect. The data are shown in Fig. 3.7.

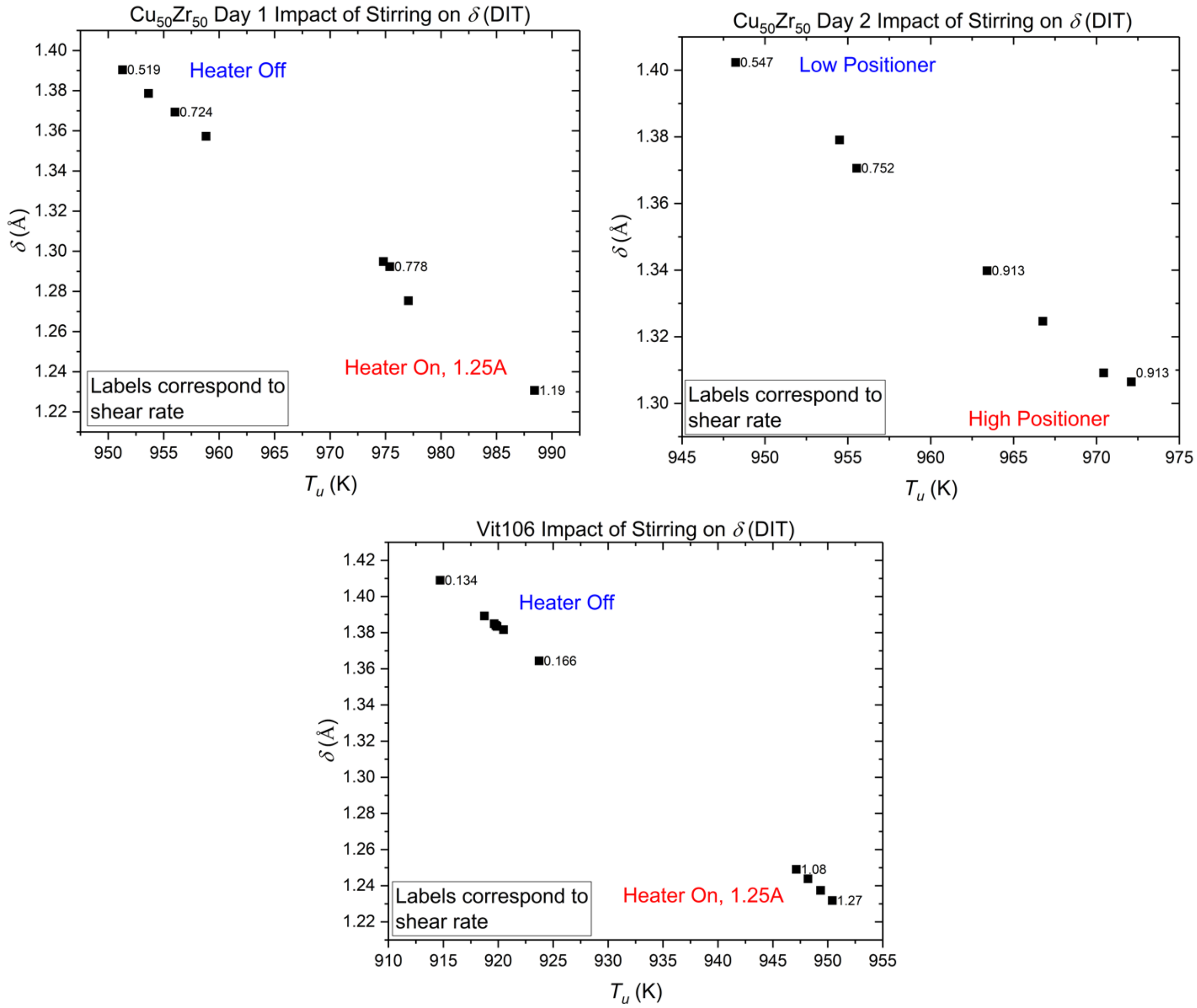

Figure 3.7: Re-analysis of data from Cu$_{50}$Zr$_{50}$ and Vit106 using the DIT. The calculation on A^* was not performed again, as the CNT and DIT have the same form.

TABLE 3.1. Calculated nucleation and stirring parameters for $Cu_{50}Zr_{50}$ at the maximum supercooling temperature for Day 1.

Cycle	Heater On? [a]	T_u (K)	A^* $(m^3s)^{-1}$ [b]	σ (J/m^2) [c]	δ (Å) [d]	v_{mf} (m/s) [e]	Shear-Rate (s^{-1}) [f]
9	Yes	975	5.75×10^{34}	0.138	1.29	4.09×10^{-4}	0.778
10	Yes	988	9.89×10^{38}	0.132	1.23	5.87×10^{-4}	1.19
16	No	956	5.27×10^{30}	0.144	1.37	2.99×10^{-4}	0.724
18	No	951	5.12×10^{29}	0.146	1.39	2.14×10^{-4}	0.519

[a] Indicates if the heater was active during the cooling of the sample.
[b] Calculated value of A^* from Eq. 3.6 at the maximum supercooling T_u and assuming $\sigma = 0.132$ J/m^2.
[c] The value of σ calculated from Eq. 3.5 assuming $A^*=10^{39}$ $(m^3s)^{-1}$, and calculated at T_u.
[d] The value of δ calculated at T_u from Eq. 3.7, assuming $A^*=10^{39}$ $(m^3s)^{-1}$ and calculated T_u.
[e] The maximum flow velocity from Bracker [19] calculated from simulations at T_u.
[f] The shear-rate from Bracker [19] calculated from simulations at T_u.

TABLE 3.2. Calculated nucleation and stirring parameters for $Cu_{50}Zr_{50}$ at the maximum supercooling temperature for Day 2.

Cycle	Positioner (V) [a]	T_u (K)	A^* $(m^3s)^{-1}$ [b]	σ (J/m^2) [c]	δ (Å) [d]	v_{mf} (m/s) [e]	Shear-Rate (s^{-1}) [f]
3	6.66	963	1.42×10^{32}	0.142	1.34	3.34×10^{-4}	0.913
4	6.66	970	7.21×10^{33}	0.139	1.30	5.09×10^{-4}	1.39
28	3.88	948	1.60×10^{29}	0.147	1.40	2.41×10^{-4}	0.547
29	3.88	955	4.84×10^{30}	0.145	1.37	3.31×10^{-4}	0.752

[a] The value of the positioner voltage at recalescence. The heater was not active during cooling this day.
[b] Calculated value of A^* from Eq. 3.6 at the maximum supercooling T_u and assuming $\sigma = 0.132$ J/m^2.
[c] The value of σ calculated from Eq. 3.5 assuming $A^*=10^{39}$ $(m^3s)^{-1}$, and calculated at T_u.
[d] The value of δ calculated at T_u from Eq. 3.7, assuming $A^*=10^{39}$ $(m^3s)^{-1}$ and calculated T_u.
[e] The maximum flow velocity from Bracker [18,19] calculated from simulations at T_u.
[f] The shear-rate from Bracker [18,19] calculated from simulations at T_u.

TABLE 3.3. Calculated nucleation and stirring parameters for Vit106 at the maximum supercooling temperature.

Cycle	Heater On? [a]	T_u (K)	A^* $(m^3s)^{-1}$ [b]	σ (J/m^2) [c]	δ (Å) [d]	v_{mf} (m/s) [e]	Shear-Rate (s^{-1}) [f]
72	No	914	7.39×10^{28}	0.116	1.41	7.36×10^{-5}	0.134
78	No	923	7.69×10^{30}	0.113	1.36	8.99×10^{-5}	0.166
81	Yes	947	2.76×10^{37}	0.105	1.25	6.52×10^{-4}	1.08
84	Yes	950	4.48×10^{38}	0.103	1.23	7.15×10^{-4}	1.27

[a] Indicates if the heater was active during the cooling of the sample.
[b] Calculated value of A^* from Eq. 3.6 at the maximum supercooling T_u and assuming $\sigma = 0.103$ J/m^2.
[c] The value of σ calculated from Eq. 3.5 assuming $A^*=10^{39}$ $(m^3s)^{-1}$, and calculated at T_u.
[d] The value of δ calculated at T_u from Eq. 3.7, assuming $A^*=10^{39}$ $(m^3s)^{-1}$ and calculated T_u.
[e] The maximum flow velocity from Bracker [20] calculated from simulations at T_u.
[f] The shear-rate from Bracker [20] calculated from simulations at T_u.

3.5 Discussion

The observed difference in the magnitude of A^* between the minimally stirred and highly stirred cycles appears to agree with the scaling between CNT and Coupled-Flux described in Eq. 3.1. The value of A^* from the minimally stirred cycles, where only the positioner was used during cooling, appear to be smaller than the highly stirred cycles by anywhere from 5 to 10 orders of magnitude. On the Day 2 measurements of $Cu_{50}Zr_{50}$, since only the positioner was used, a smaller difference in the magnitude of A^* is observed between minimally and maximally stirred cycles. However, despite the smaller difference in the magnitude of A^*, the overall range in values is still in-line with predictions from Eq. 3.1. Thus, it is possible diffusion-limited nucleation was observed in the positioner-only cycles. The same can be said about the Vit106 cycles, despite their performance in helium. Even if helium introduced heterogeneous nucleation sites, which may be responsible for the smaller maximum supercooling observed in Fig. 3.6, the addition or removal of stirring should have an observable effect on the nucleation kinetics. The only likely impact heterogeneous nucleation may have on the data is a systematic reduction in the maximum supercooling for all cycles performed during that night.

Ground-based studies explored the impact of cooling rate on the maximum supercooling achieved by several samples of $Ti_{40}Zr_{30}Ni_{30}$. For these experiments, a sample of $Ti_{40}Zr_{30}Ni_{30}$ was levitated in ESL, melted, and allowed to cool freely until crystallization. This process was repeated approximately 150 times. Another sample of $Ti_{40}Zr_{30}Ni_{30}$ was levitated and melted, but the heating laser was left on and reduced to a small value for the duration of the cooling cycle. As seen in Fig. 3.8, no significant impact on maximum supercooling was detected. Another sample of $Ti_{40}Zr_{30}Ni_{30}$ was studied for the statistical analysis outlined elsewhere [9] and its distribution of supercoolings, which were gathered from a freely cooling sample, do not show any deviation from the other distributions. Only a minor shift in the fitted curve of $Ti_{40}Zr_{30}Ni_{30}$ supercooling measurements was found and the maximum of subsequent free cools on sample m6376 lies directly between the two curves; this could indicate sample-to-sample variation was the cause of the discrepancy and not different cooling rates. It also implies that minimally and maximally stirred cycles in ground-based ESL studies likely cannot reach the diffusion-limited nucleation regime, as suggested in the SRD [5]. The differences in maximum supercooling seen from the EML studies above are on the order of 10-30 Kelvin, while ground-based ESL supercooling measurements saw only a 1-2 Kelvin difference despite the slower cooling rate. Therefore, the differences in cooling rate are likely not completely responsible for the different nucleation parameters presented in Section 3.4.

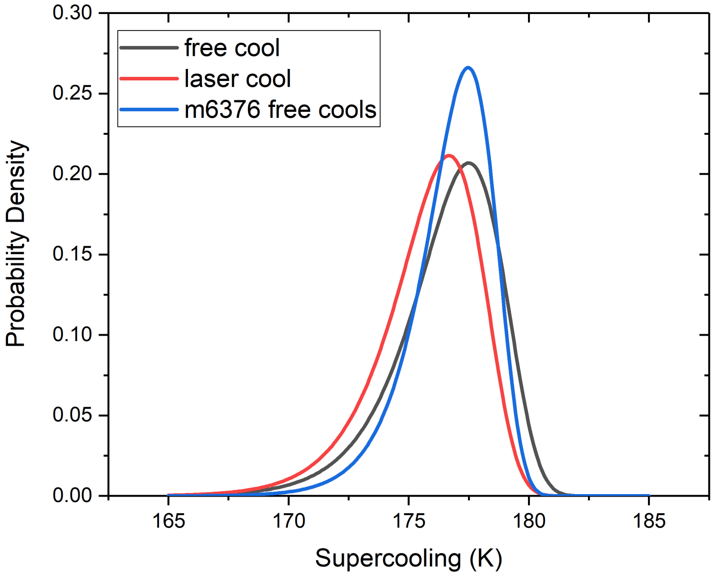

Figure 3.8: Three fitted probability density curves for three different samples of $Ti_{40}Zr_{30}Ni_{30}$. Note that the maximum of the m6376 free cool curve lies in between the free cool and laser cool curves of the other two samples, indicating that cooling rate likely had a minimal impact on the maximum achievable supercooling.

The minimally stirred cycles for $Cu_{50}Zr_{50}$, such as Cycle 18, 28, and 29, are already pushing or slightly exceeding the upper shear rate limit (0.5 sec^{-1}) for diffusion-limited nucleation. Despite this, the data from the minimally stirred $Cu_{50}Zr_{50}$ cycles may still suggest diffusion-limited kinetics, or that the kinetic contribution due to stirring is nearly equal to that of diffusion. This may be seen in the calculated maximum flow velocity from Bracker [18,19]. Using the viscosity of $Cu_{50}Zr_{50}$ at the maximum supercooling temperature, the diffusion velocity can be predicted from a simple relation $v = D/L$, where D is the Stokes-Einstein diffusion relation and a value of the diffusion length L is approximately 10nm [5]. As reported in the SRD, "[t]o observe the effects of diffusion on nucleation, [the diffusion velocity] must be larger than any stirring effects" [5]. The predicted diffusion velocity is $4.8\text{x}10^{-4}$ m/s, using 1.40 Pa·s at 950 K for $Cu_{50}Zr_{50}$. The diffusion velocity is larger than the maximum flow velocity for Cycle 18, 28, and 29. Therefore, the flow in these cycles may be slow enough to allow for diffusion to influence nucleation; otherwise, a larger maximum flow velocity would likely mask out any kinetic contribution from diffusion. However, these values are close enough that small stirring contributions from the EML may be included.

Simulations of Vit106 cycles appear to reinforce inferences acquired from $Cu_{50}Zr_{50}$ data. Cycle 72 and 78 show a shear rate well within the outlined parameters for diffusion-limited nucleation. These two cycles show the deepest supercooling and slowest maximum flow velocity, coinciding with no heater active during cooling. Meanwhile, Cycle 81 and 84, which had the heater active during cooling, show a calculated shear rate that easily exceeds the limit of diffusion-limited nucleation. Using the viscosity reported for Vit106 (3.54 Pa·s at 915 K) and following the calculations performed in the SRD [5] suggest that the predicted diffusion velocity for Vit106 is $1.9\text{x}10^{-4}$ m/s. The maximum flow calculated for Cycle 72 and 78 is significantly smaller than the maximum diffusion velocity, further suggesting diffusion-limited nucleation was observed. Meanwhile, the maximum flow velocity for Cycle 81 and 84 is significantly larger, further suggesting that stirring influenced nucleation.

However, the predicted shear range for diffusion-limited nucleation was calculated for $Ti_{39.5}Zr_{39.5}Ni_{21}$ and there may be systematic variation from that range based on alloy composition. As an example, consider the differences in viscosity—a thermophysical property related to kinetics—between $Ti_{39.5}Zr_{39.5}Ni_{21}$ and Vit106. The viscosity at the maximum supercooling temperature for $Ti_{39.5}Zr_{39.5}Ni_{21}$ (0.26 Pa·s at 950K) is almost 14 times smaller than the viscosity of Vit106. Therefore, the maximum diffusion velocity is larger for $Ti_{39.5}Zr_{39.5}Ni_{21}$ at $3.1\text{x}10^{-3}$ m/s, since the viscosity is inversely related to D. Four cycles on Vit106 not shown above—1, 8, 60, and 68—were examined with CFD, with Cycle 1 and Cycle 8 being performed in vacuum and Cycle 60 and Cycle 68 being performed in helium. The calculated shear rates range from 0.03 to 0.27 sec^{-1} [20], with Cycle 60 yielding the largest shear rate. The smaller shear rates typically emerged from cycles where only the positioner was active during cooling and was between 2.5 and 6 volts. The larger shear rate, while still within the predicted diffusion-limited regime, resulted from a cycle where the heater was active during cooling and set to a value of 1.25 volts. The predicted maximum diffusion velocity for Cycle 60, using Bracker's parameters (8.37 Pa·s at 875 K) [20], is $7.7\text{x}10^{-5}$ m/s, while the maximum flow velocity was calculated to be $1.54\text{x}10^{-4}$ m/s. Despite the shear-rate falling within the previously outlined range for diffusion-limited nucleation, the maximum flow velocity is larger than the diffusion velocity, which could imply a stirring contribution. The other cycles performed that night, where only the minimum positioner voltage was used during cooling, achieved a maximum supercooling anywhere from 20 to 50 degrees deeper than Cycle 60 and a shear rate 7 times smaller. In addition, their maximum flow velocities were always smaller than the predicted maximum diffusion velocity, suggesting that diffusion likely impacted the nucleation.

The heater clearly makes an impact on the maximum supercooling and in the calculated shear rate, possibly due to more stirring relative to positioner-only cycles. Published magnetohydrodynamics simulations by Xiao *et. al.* using data from the EML-ISS further support this point by showing the heater can induce stronger flow within the droplet [21]. Xiao *et. al.* found that the shear rate in modeled Fe-19Cr-21Ni (atomic %) at 1500K (T_l – 200K) was almost 400 times larger for a cycle with an applied heater voltage of 5.70 volts versus a cycle with a heater voltage of 0.01 volts. In practice, such a large heater voltage is not feasible for experimental studies. However, even with a more reasonable heater setting of 1.0 volts, the models from Xiao *et. al.* show a shear rate at 1500K between 50 and 100 times larger than the shear rate from a cycle with a heater voltage of 0.01. The range of shear rates in Tables 3.1 through 3.3 do not show such extreme differences; however, a difference in shear rate between two and ten times is observable between cycles with the heater active during cooling and those without it.

The magnitude of observed supercooling also decreases with increased stirring. With high levels of stirring, stronger convection currents may bring atoms into the shell and expedite cluster growth. Thus, the more rapid kinetics in highly stirred liquids may limit the amount of time the metallic liquid can cool before a critical nucleus is formed. In contrast, diffusion-limited nucleation will slow down the kinetics and force the cluster to wait for atoms to move into the shell. The slower kinetics, and thus slower growth of the cluster, may allow the metallic liquid to cool more deeply before the nuclei grows large enough to initiate crystallization.

There is no theoretical prediction on the impact on the interfacial free energy in diffusion-limited nucleation. However, as described by Kelton and Greer [13], “the depletion of the original phase immediately surrounding the cluster will locally shift the driving free energy and hence the critical size.” The interfacial free energy only applies to the interaction between the cluster and shell; however, the interfacial free energy is related to the cluster size. A shift in the driving free energy would change the critical cluster size needed to form a viable nuclei [22–24]. This may be related to the overall deeper supercooling observed in more quiescent liquids when compared to highly stirred liquids. However, since there is no theoretical prediction of this effect, the observed trends may simply be due to circumstance.

The results from the DIT appear to support the interpretation of the data within the Coupled-Flux theory. In the diffusion-limited case, the cluster and the surrounding parent phase will have a higher difference between the enthalpy and entropy curves due to the different solute concentration around the cluster. However, when stirring is introduced, the solute concentration may be modulated to more closely mirror the composition of the cluster, thereby reducing δ. However, this interpretation relies on key concepts from the Coupled-Flux theory, indicating that the DIT on its own is likely insufficient to describe the nucleation kinetics here. While the DIT does account for a more diffuse interface between the crystal and parent phase, it does not account for the effects of compositional change around the cluster during diffusion-limited nucleation.

3.6 Conclusion

The results from studies of $Cu_{50}Zr_{50}$ and Vit106 using the EML on-board the ISS were reported and discussed using the CNT, DIT, and Coupled-Flux theories. Calculations performed on $Cu_{50}Zr_{50}$ and Vit106 suggest that nucleation may be limited by diffusion during cycles where only the positioner was active. When the heater was active during cooling, a sharp change in the calculated nucleation parameters was observed, likely due to the introduction of stirring. Due to time constraints with launching samples into orbit, sharing the facility with other investigators, and unforeseen problems occurring with the EML, only two samples were shown in this chapter. Future studies are planned on several other samples to more fully explore the initial results presented in this chapter.

3.7 References

1. Kelton, K. F. Crystal Nucleation in Liquids and Glasses. *Solid State Phys. - Adv. Res. Appl.* **45**, 75–177 (1991).

2. Kelton, K. F. *et al.* Oxygen precipitation in silicon: Experimental studies and theoretical investigations within the classical theory of nucleation. *J. Appl. Phys.* **85**, 8097–8111 (1999).

3. Wei, P. F., Kelton, K. F. & Falster, R. Coupled-flux nucleation modeling of oxygen precipitation in silicon. *J. Appl. Phys.* **88**, 5062–5070 (2000).

4. Kelton, K. F. Diffusion-influenced nucleation: A case study of oxygen precipitation in silicon. in *Philosophical Transactions of the Royal Society A: Mathematical, Physical and Engineering Sciences* **361**, 429–446 (2003).

5. Kelton, K. F., Gangopadhyay, A. K., Hyers, R. & Holland-Moritz, D. Studies of Nucleation and Growth, Specific Heat and Viscosity of Undercooled Melts of Quasicrystals and Polytetrahedral-Phase-Forming Alloys. *Science Requirements Document (SRD), QUASI-RQMT-0001* (2002).

6. Marangoni, C. On the expansion of a drop of liquid floating on the surface of another

liquid. *Tipographia dei Frat. Fusi, Pavia* (1865).

7. Hyers, R. W. Fluid flow effects in levitated droplets. *Meas. Sci. Technol.* **16**, 394–401 (2005).

8. Schroers, J. *et al.* Enhanced temperature uniformity by tetrahedral laser heating. *Rev. Sci. Instrum.* **75**, 4523–4527 (2004).

9. Sellers, M. E., Van Hoesen, D. C., Gangopadhyay, A. K. & Kelton, K. F. Maximum supercooling studies in $Ti_{39.5}Zr_{39.5}Ni_{21}$, $Ti_{40}Zr_{30}Ni_{30}$, and $Zr_{80}Pt_{20}$ liquids—Connecting liquid structure and the nucleation barrier. *J. Chem. Phys.* **150**, 204510 (2019).

10. Kelton, K. F. Time-Dependent Nucleation in Partitioning Transformations. *Acta Mater.* **48**, 1967–1980 (2000).

11. Kelton, K. F. Kinetic model for nucleation in partitioning systems. *J. Non. Cryst. Solids* **274**, 147–154 (2000).

12. Russell, K. C. Linked flux analysis of nucleation in condensed phases. *Acta Metall.* **16**, 761–769 (1968).

13. Kelton, K. & Greer, A. L. *Nucleation in condensed matter: applications in materials and biology*. **15**, (Elsevier, 2010).

14. Bracker, G. P. & Hyers, R. W. *Calculated Results for Flow Characterization of Ti39.5Zr39.5Ni21 during EML Experiments in Reduced Gravity*. (2019).

15. ANSYS Inc. *ANSYS Fluent Tutorial Guide*. **18.0**, (2017).

16. Turnbull, D. Formation of crystal nuclei in liquid metals. *J. Appl. Phys.* **21**, 1022–1028

(1950).

17. Turnbull, D. Kinetics of Solidification of Supercooled Liquid Mercury Droplets. *J. Chem. Phys.* **20**, 411–424 (1952).

18. Bracker, G. P. & Hyers, R. W. *Calculated Flow Results for Cu 50 Zr 50 Experiments in the ISS-EML Facility*. (2019).

19. Bracker, G. P. & Hyers, R. W. *Additional Calculated Flow Results for Cu 50 Zr 50 Experiments in the ISS-EML Facility*. (2020).

20. Bracker, G. P. & Hyers, R. W. *Calculated Flow Characterization for ISS-EML Experiments on Vit106*. (2020).

21. Xiao, X., Lee, J., Hyers, R. W. & Matson, D. M. Numerical representations for flow velocity and shear rate inside electromagnetically levitated droplets in microgravity. *npj Microgravity* **5**, 1–7 (2019).

22. Bai, X. M. & Li, M. Calculation of solid-liquid interfacial free energy: A classical nucleation theory based approach. *J. Chem. Phys.* **124**, (2006).

23. Tolman, R. C. The effect of droplet size on surface tension. *J. Chem. Phys.* **17**, 333–337 (1949).

24. Wu, D. T., Gránásy, L. & Spaepen, F. Nucleation and the solid-liquid interfacial free energy. *MRS Bull.* **29**, 945–950 (2004).

Chapter 4: Maximum Supercooling Studies in $Ti_{39.5}Zr_{39.5}Ni_{21}$, $Ti_{40}Zr_{30}Ni_{30}$, and $Zr_{80}Pt_{20}$ Liquids – Connecting Liquid Structure and the Nucleation Barrier

Portions of this chapter were originally published in the Journal of Chemical Physics, 150, 204510 (2019). It is reproduced here with permission from AIP Publishing with minor revisions to include a discussion and analysis of data within the Diffuse Interface Theory of Nucleation.

Almost three quarters of a century ago, Charles Frank proposed that the deep supercooling observed in metallic liquids is due to icosahedral short-range order (ISRO), which is incompatible with the long-range order of crystal phases. Some evidence in support of this hypothesis has been published previously. However, those studies were based on a small population of maximum supercooling measurements before the onset of crystallization. Here, the results of a systematic statistical study of several hundred maximum supercooling measurements on $Ti_{39.5}Zr_{39.5}Ni_{21}$, $Ti_{40}Zr_{30}Ni_{30}$, and $Zr_{80}Pt_{20}$ liquids are presented. Previous X-Ray and neutron scattering studies have shown that the structures of these liquid alloys contain significant amounts of ISRO. The results presented here show a small work of critical cluster formation ($W^* = 31 - 40\ k_BT$) from the analysis of the supercooling data for the $Ti_{39.5}Zr_{39.5}Ni_{21}$ liquid, which crystallizes to a metastable icosahedral quasicrystal. A much larger value ($W^* = 54 - 79\ k_BT$ and $W^* = 60 - 99\ k_BT$) was obtained for the $Ti_{40}Zr_{30}Ni_{30}$ and $Zr_{80}Pt_{20}$ liquids respectively, which do not crystallize to an icosahedral quasicrystal. Taken together, these results significantly strengthen the validity of Frank's hypothesis.

4.1 Introduction

Fahrenheit first noticed the tendency for liquids to exist in the liquid phase below the equilibrium melting temperature [1], also known as supercooling, which indicated the existence of a barrier to the phase transition. This barrier is now recognized as an essential ingredient to crystal nucleation—the formation of the first ordered regions in the liquid. The process of nucleation is typically understood within the framework of Classical Nucleation Theory (CNT), where the nucleation barrier arises from a competition between the thermodynamic driving free energy and the energy cost for creating an interface between the nucleating phase and the liquid. The CNT was developed by Gibbs [2], Volmer & Weber [3], and Becker & Döring [4] for gas condensation and was later extended to describe crystal nucleation in a liquid by Turnbull and Fisher [5]. Within CNT, the steady-state rate for forming crystal nuclei is expressed in terms of the atomic mobility at the crystal-liquid interface (contained in the pre-term A^*), the work required to form the initial critical cluster W^*, and the temperature T, as outlined in Eq. 4.1.

$$I^{ST} = \frac{24Dn^{*\frac{2}{3}}N_A}{\lambda^2}\left(\frac{|\Delta\mu|}{6\pi k_B T n^*}\right)^{\frac{1}{2}} \exp\left(-\frac{W^*}{k_B T}\right) = A^* \exp\left(-\frac{W^*}{k_B T}\right) \tag{4.1}$$

Here, λ is the atomic jump distance, D is the diffusion coefficient, n^* is the number of atoms in the critical nucleus, N_A is Avogadro's number, $\Delta\mu$ is the change in chemical potential per atom, and k_B is the Boltzmann constant. From CNT, the work to form the critical nucleus, W^*, for a spherical nucleus is given in Eq. 4.2:

$$W^* = \frac{16\pi}{3}\frac{\sigma^3}{\Delta g^2} \tag{4.2}$$

where Δg is the Gibbs free energy difference per unit volume ($\Delta g = \Delta\mu/\bar{v}$, where $\bar{v}$ is the atomic volume) and σ is the interfacial free energy. Turnbull and Fisher assumed that the attachment mobility at the interface was related to the diffusion coefficient in the liquid, *D*. This is generally obtained from the viscosity, η, assuming the Stokes-Einstein relation ($D = k_B T/6\pi\eta a$), where a is a length that corresponds approximately to the atomic diameter.

An extension of CNT was developed independently by both Spaepen [6] and Gránásy to account for extended (or diffuse) interfaces [7,8], as first-principles calculations implied that the CNT failed to accurately describe ordering at the interface. Gránásy parameterized the cross-interfacial enthalpy and entropy distributions, arriving at a definition of the critical work of cluster formation (Eq. 4.3):

$$W^* = -\kappa\delta^3\Delta g_0\psi(\eta) \tag{4.3}$$

where $\kappa = 4\pi/3$, $\Delta g_0 = \Delta h_0 - T\Delta s_0$, $\psi(\eta) = 2(1+q)\eta^{-3} - (3+2q)\eta^{-2} + \eta^{-1}$, $q = (1-\eta)^{-1/2}$, $\eta = \Delta g_0/\Delta h_0$, Δh_0 and Δs_0 are the enthalpy and entropy differences between the parent and new phase, and δ is the interfacial thickness defined by the difference in location between the enthalpy and entropy surfaces ($\delta = R_S - R_H$). Following the kinetic approach, the nucleation rate can be calculated as $I^{ST} = I_0 \exp(-W^*/k_B T)$, arriving at the same steady-state form as CNT.

Since CNT was originally developed for gas condensation, it does not explicitly consider the short- and medium-range order within the liquid. Frank proposed that the presence of such order, specifically icosahedral short-range order (ISRO), gives rise to the nucleation barrier in metallic liquids [9]. However, such a barrier is not limited to ISRO, any type of order that is incompatible with the long-range order in the underlying crystal phase may give rise to the nucleation barrier. Previous experimental studies have confirmed the presence of ISRO in metallic liquids [10] which was further corroborated by linking ISRO to the nucleation barrier in a $Ti_{39.5}Zr_{39.5}Ni_{21}$ supercooled liquid [11,12], providing strong support for Frank's hypothesis. However, the analysis of the supercooling data in the framework of CNT in the previous study of Ti-Zr-Ni liquids [13] was based on a small number of maximum supercooling cycles. Since nucleation is a stochastic process, as explained in section III, a quantitative analysis requires the collection of a large population of maximum supercooling temperatures. Such extensive studies are presented here for the $Ti_{39.5}Zr_{39.5}Ni_{21}$, $Ti_{40}Zr_{30}Ni_{30}$, and $Zr_{80}Pt_{20}$ liquids. These alloys were chosen because the $Ti_{39.5}Zr_{39.5}Ni_{21}$ liquid has strong ISRO and crystallizes first to a metastable quasicrystal phase [11–13]. The $Ti_{40}Zr_{30}Ni_{30}$ liquid contains distorted ISRO [13] and crystallizes to the C14 Laves phase [12] and the $Zr_{80}Pt_{20}$ liquid contains moderate ISRO and crystallizes to a phase mixture of Zr_5Pt_3 and βZr [14–16]. In agreement with Frank's hypothesis, W^* is found to be much larger for the nucleation of the ordered phases from the $Ti_{40}Zr_{30}Ni_{30}$ and $Zr_{80}Pt_{20}$ liquids than it is for nucleating the quasicrystal phase from the $Ti_{39.5}Zr_{39.5}Ni_{21}$ liquid.

4.2 Methods

Master ingots were prepared by arc-melting high purity Zr (Smart Elements, Vienna, 99.97 at.%), Ni (Alfa Aesar 99.999 at.%), Ti (Alfa Aesar 99.999 at.%), and Pt (Alfa Aesar 99.997 at.%) on a water-cooled Cu hearth in a high purity (99.999 at.%) Ar atmosphere. A $Ti_{50}Zr_{50}$ getter located close to the sample was melted for 60 seconds prior to melting the sample to further reduce residual oxygen inside the chamber. The master ingots were melted and flipped three times to ensure chemical homogeneity, with each melting cycle lasting approximately 15 seconds to reduce mass loss due to evaporation and any residual oxygen contamination. Upon verification of negligible mass-loss (less than 0.1%), the master ingots were broken and portions were re-melted to obtain small spherical samples approximately 2.5mm in diameter, with masses ranging from 45mg to 75mg.

Nucleation can either be homogeneous or heterogeneous. Homogeneous nucleation is of most interest for these studies since it is characteristic of the thermodynamic and kinetic factors of the liquid and nucleating phases, while heterogeneous nucleation is catalyzed at specific sites, particularly by containers or sample impurities. Since metallic liquids are sensitive to oxygen and prone to heterogeneous nucleation, the studies were conducted in the high-vacuum and containerless processing environment of the Washington University Beamline Electrostatic Levitator (WU-BESL) [17,18]. The $Ti_{39.5}Zr_{39.5}Ni_{21}$ samples were processed at pressures ranging from 4.5×10^{-8} Torr to 8×10^{-8} Torr, the $Ti_{40}Zr_{30}Ni_{30}$ samples were processed at 5.7×10^{-8} Torr, and the $Zr_{80}Pt_{20}$ samples were processed at 8×10^{-8} Torr. The spherical sample was first levitated and then melted using a high-intensity 980nm 50-Watt diode laser. A Process Sensors Metis MI18 MB8 single-color pyrometer, operating at a wavelength of 1.89μm, was used to measure the sample temperature in the 160 °C to 800 °C range. A Process Sensors Metis MQ22 two-color ratio pyrometer, operating at wavelengths of 1.4μm and 1.64μm, was used to measure sample temperatures above 600 °C. The melting plateau at 820 °C for $Ti_{39.5}Zr_{39.5}Ni_{21}$, 868 °C for $Ti_{40}Zr_{30}Ni_{30}$, and 1177 °C for $Zr_{80}Pt_{20}$ served as references for the calibration of the pyrometers. The temperature measurement error was corrected by assuming a constant emissivity ratio in the pyrometers; further discussion of this technique is outlined elsewhere [19]. The shear viscosity was also obtained for the liquids through the oscillating drop technique by modulating the vertical voltage to induce an oscillation in the liquid and measuring the decay time upon removing the perturbation. A detailed discussion of the density and viscosity measurement techniques can be found elsewhere [15,20].

4.3 Analysis and Results

Solid spherical samples were levitated, melted, and heated to several hundred degrees above the liquidus temperature to achieve maximum supercooling. The laser was then turned off and the sample cooled by radiative loss. The nucleation and growth of the crystal phase was marked by a rapid rise in the sample's temperature due to the release of the heat of fusion during crystallization, a process termed recalescence. The temperature profile during a typical heating and cooling cycle of a $Ti_{39.5}Zr_{39.5}Ni_{21}$ sample is illustrated in Fig. 4.1.

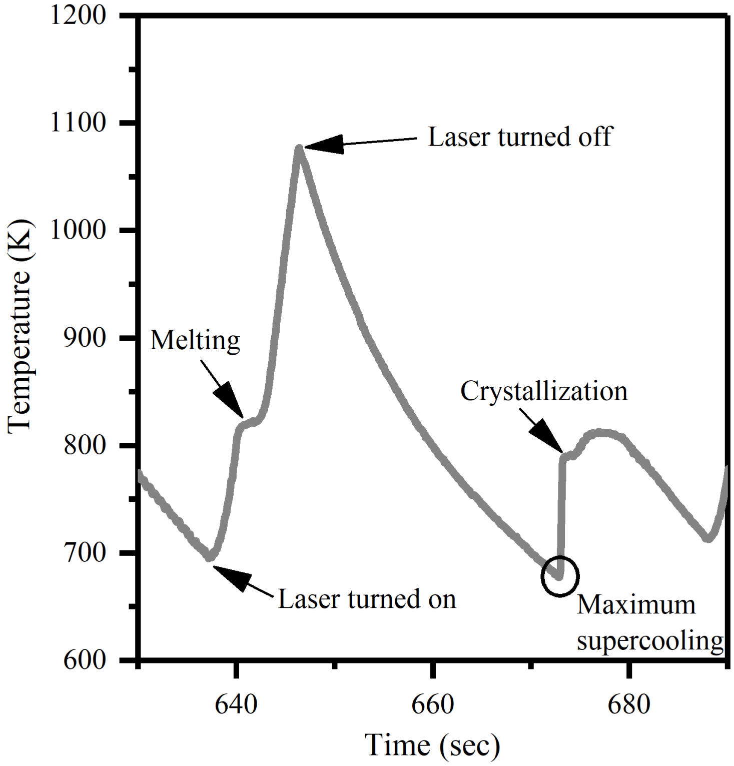

Figure 4.1: A representative heating and cooling cycle for $Ti_{39.5}Zr_{39.5}Ni_{21}$. In this liquid, two recalescence events are observed. The first corresponds to the transformation of the liquid to a metastable icosahedral quasicrystal phase and the second to the stable phase mixture of C14 polytetrahedral Laves phase and solid solution [12].

Such thermal cycles were repeated many times in both liquid alloys to generate a distribution of maximum supercooling temperatures (T_u). The first 25 cycles were excluded from the analysis because the supercooling temperatures gradually improved and stabilized around the maximum supercooling temperature with repeated processing. When consistent supercooling behavior was observed, at least 100 cycles were run and T_u was measured.

To make sure that the sample quality did not change after many thermal cycles due to thermal evaporation or contamination from the residual oxygen in the BESL chamber, a consistency check was made. As seen in Fig. 4.2, the maximum supercooling was plotted against cycle number—a proxy for time, as each cycle happened sequentially—to check for any deterioration in supercooling. The supercooling is the difference between the liquidus temperature (T_l) and the maximum supercooling temperature (T_u), i.e. $\Delta T = T_l - T_u$. Since the icosahedral quasicrystal was the primary crystallizing phase in $Ti_{39.5}Zr_{39.5}Ni_{21}$, the supercooling for each cycle was calculated with respect to the metastable liquidus temperature of this phase (790 °C). For $Ti_{40}Zr_{30}Ni_{30}$ and $Zr_{80}Pt_{20}$, the equilibrium liquidus temperatures (892 °C and 1177 °C, respectively) were used. A linear regression analysis was performed and the R value showed no significant evidence of a dependence of supercooling on cycle number ($p > 0.05$). The supercooling values are scattered evenly around the linear fit, providing evidence that the supercooling was limited by the inherent randomness of homogeneous nucleation. The introduction of contamination into the sample, such as residual oxygen in the chamber or a change in composition due to evaporation, would lead to a significant change in supercooling with time, producing a higher R value, suggesting a heterogeneous nucleation mechanism.

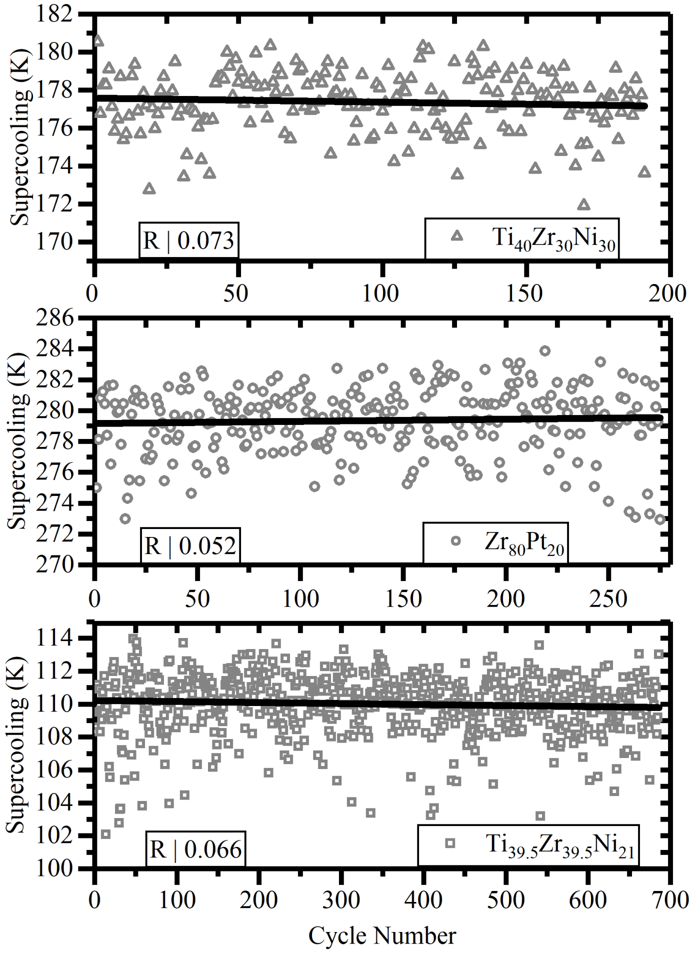

Figure 4.2: Maximum supercooling as a function of cycle number. No significant dependence between supercooling and cycle number is observed, indicating that the nucleation was reproducible.

The pre-factor and work of cluster formation for nucleation were obtained from these data using a statistical treatment developed by Skripov [21]. Since each nucleation event is random and occurs independently of the previous one, within a certain range of supercooling temperatures and with an average value, Poisson statistics can be used to describe the nucleation events. The general form of the probability density of nucleation events shown in Eq. 4.4 is:

$$\omega(T) = \frac{I^{ST}V}{\dot{T}} \exp\left(-\frac{V}{\dot{T}}\int_{T_u}^{T_l} I^{ST}\,dT\right) \tag{4.4}$$

where I^{ST} is the steady-state nucleation rate $I^{ST} = A^{*}\exp(-W^{*}/k_{B}T)$, A^{*} is the classical nucleation pre-term divided by the viscosity as indicated in Eq. 4.1, V is the volume of the droplet, and $\dot{T}$ is the cooling rate, *dT/dt*.

To fit the distribution of supercooling temperatures to Eq. 4.4 and extract A^{*}, W^{*}, and σ, the driving free energy is needed as an input parameter. It was calculated by two different methods, once using the Turnbull approximation (Eq. 4.5.1) and again assuming the Thompson-Spaepen [22] approximation (Eq. 4.5.2):

$$\Delta G = \frac{\Delta H_f \Delta T}{T_l} \tag{4.5.1}$$

$$\Delta G = \frac{\Delta H_f \Delta T}{T_l}\frac{2T}{T_l + T} \tag{4.5.2}$$

where ΔH_f is the enthalpy of fusion. The driving free energy per atom, $\Delta\mu$, is obtained by normalizing ΔG by N_A. The enthalpy of fusion was obtained from previously reported results for $Ti_{39.5}Zr_{39.5}Ni_{21}$ (ΔH_f = 8.48 kJ/mol) and $Ti_{40}Zr_{30}Ni_{30}$ (ΔH_f = 11.2 kJ/mol) [12], and estimated using Richard's Rule [23] for $Zr_{80}Pt_{20}$ (ΔH_f = 12.0 kJ/mol). The interfacial free-energy σ was also calculated twice, assuming it to be temperature independent (σ) or assuming a linear temperature dependence ($\sigma = \sigma_0 T$). Turnbull suggested that the linear temperature dependence arose from an overestimate of the entropy change at the crystal nucleus-liquid interface due to the assumption of a sharp interface in the classical theory of nucleation [24,25]. The results from theoretical models that are based on the assumption of a diffuse interface support this conclusion [6,7]. The viscosity was used as an input parameter. Equation 4.5 was then fit to the histogram of measured ΔT values with A^{*} and W^{*} as fit parameters, assuming the temperature dependences of the different approximation for $\Delta\mu$ and σ. Since the different temperature dependence assumptions for $\Delta\mu$ and

σ do not change the overall shape of the fitted curve, a representative plot for each alloy is reproduced in Fig. 4.3 and Fig. 4.4. Finally, σ was calculated from Eq. 4.2 and the corresponding driving free energy.

For DIT calculations, a similar procedure was followed. As the steady-state nucleation rate has the same form [7,8], it can be substituted into Eq. 4.4 with the definition of W^* from Eq. 4.3. The non-linear least-squares fitting routine was then performed again. The enthalpy and viscosity were used as input parameters. δ was calculated from the best-fit parameter to Eq. 4.3.

A total of 686 supercooling cycles were collected from six different $Ti_{39.5}Zr_{39.5}Ni_{21}$ samples, with masses ranging from 49.7mg to 57.5mg. The slight differences in sample volume were considered by normalizing for the different masses. A consistent supercooling temperature with an average value of 110°C (10.3% supercooling) was observed (Fig. 4.3) for all six samples studied; the width of the distribution is approximately 11°C. It is important to note that the distribution is asymmetric, dropping faster on the deeper supercooling side. This is typically considered to be a characteristic of homogeneous nucleation [26,27]. The average supercooling temperature was used to obtain the values for A^*, W^* and σ as listed in Table 4.1.

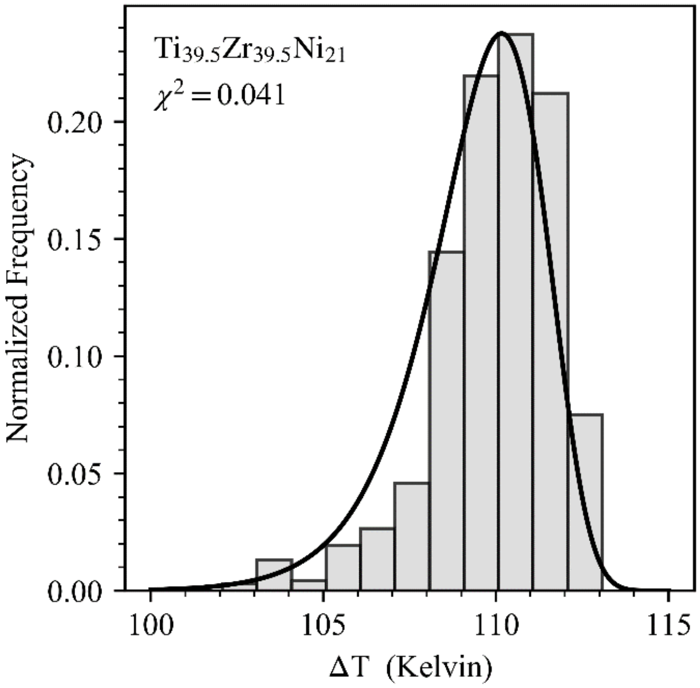

Figure 4.3: The histogram of maximum supercooling measurements for $Ti_{39.5}Zr_{39.5}Ni_{21}$. The average supercooling was 110 °C (10.3%). The curve is the fitted probability density (Eq. 4.3), with a p-value > 0.999, indicating a good fit.

TABLE 4.1. Calculated nucleation parameters for $Ti_{39.5}Zr_{39.5}Ni_{21}$ at the average supercooling for different approximations of ΔG and the assumed temperature dependence of σ.

Approximation [a]	A^* $(m^3s)^{-1}$	W^*/k_BT	σ (J/m^2) [b]	σ_0 (J/m^2K) [c]
Turnbull, $\sigma = constant$	$2.74\text{x}10^{25}$	37.18	0.057	
Turnbull, $\sigma \propto T$	$7.60\text{x}10^{22}$	31.29	0.054	$5.68\text{x}10^{-5}$
Thompson-Spaepen, $\sigma = constant$	$3.72\text{x}10^{26}$	39.79	0.057	
Thompson-Spaepen, $\sigma \propto T$	$2.02\text{x}10^{23}$	33.15	0.053	$5.58\text{x}10^{-5}$

[a] The approximation used for the driving free energy and assumption made about the dependence of σ on temperature.

[b] The value of σ, when assumed to be a constant, or calculated at T_u, the average supercooling temperature, when assumed to be linearly temperature dependent.

[c] The temperature coefficient (σ_0) for $\sigma = \sigma_o T$.

For $Ti_{40}Zr_{30}Ni_{30}$, the data from 191 nucleation cycles for a 63.8mg sample gave an average supercooling of 177 °C (15.2% supercooling), as shown in Fig. 4.4. The supercooling is slightly deeper and the distribution is narrower (8 °C) than observed for $Ti_{39.5}Zr_{39.5}Ni_{21}$. Like

$Ti_{39.5}Zr_{39.5}Ni_{21}$, the overall shape of the fit curve does not change with the approximation assumed for $\Delta\mu$ and σ. The fit parameters from the distribution curve and the extracted nucleation properties calculated at the average supercooling temperature using different approximations are listed in Table 4.2.

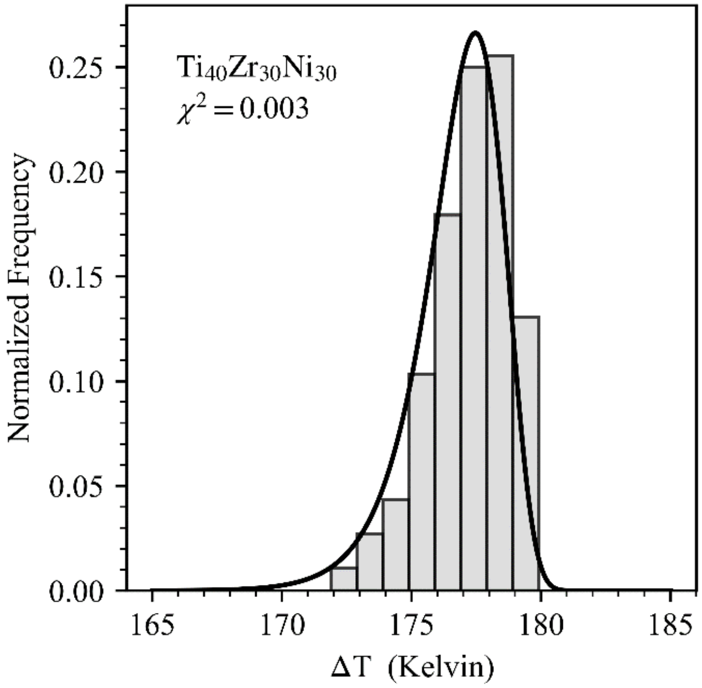

Figure 4.4: The histogram of maximum supercooling measurements for $Ti_{40}Zr_{30}Ni_{30}$. The average supercooling was 177 °C (15.2%). The curve is the fitted probability density (Eq. 4.3), with a p-value > 0.999, indicating a good fit.

TABLE 4.2. Calculated nucleation parameters for $Ti_{40}Zr_{30}Ni_{30}$ at the average supercooling for different approximations of ΔG and the assumed temperature dependence of σ.

Approximation [a]	A^* $(m^3s)^{-1}$	W^*/k_BT	σ (J/m^2) [b]	σ_0 (J/m^2K) [c]
Turnbull, σ = *constant*	4.85×10^{39}	70.54	0.114	
Turnbull, $\sigma \propto T$	4.39×10^{32}	54.32	0.104	1.05×10^{-4}
Thompson-Spaepen, σ = *constant*	2.28×10^{43}	79.00	0.111	
Thompson-Spaepen, $\sigma \propto T$	6.14×10^{34}	59.26	0.101	1.02×10^{-4}

[a] The approximation used for the driving free energy and assumption made about the dependence of σ on temperature.

[b] The value of σ, when assumed to be a constant, or calculated at T_u, the average supercooling temperature, when assumed to be linearly temperature dependent.

[c] The temperature coefficient (σ_0) for $\sigma = \sigma_o T$.

The data from 274 nucleation cycles for a 72.7mg sample of $Zr_{80}Pt_{20}$ gave an average supercooling of 279 °C (19.2% supercooling), as shown in Fig. 4.5. Compared with the measurements for $Ti_{39.5}Zr_{39.5}Ni_{21}$, the supercooling is almost two times larger and the distribution of supercooling temperatures is slightly narrower, with a width of approximately 10°C. Again, the overall shape of the fit curve does not change with the approximation assumed for $\Delta\mu$ and σ. The fit parameters from the distribution curve and the extracted nucleation properties calculated at the average supercooling temperature using different approximations are listed in Table 4.3.

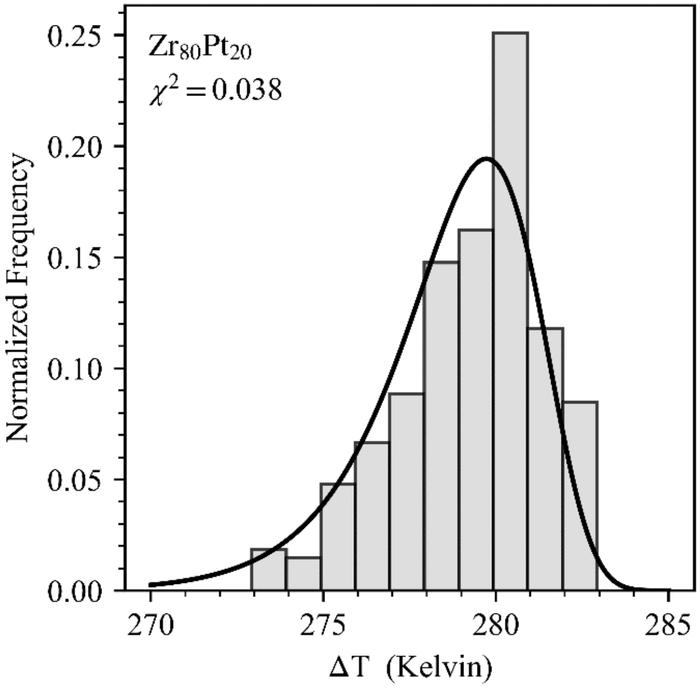

Figure 4.5: The histogram of maximum supercooling measurements for $Zr_{80}Pt_{20}$. The average supercooling was 279 °C (19.2%). The curve is the fitted probability density, with a p-value > 0.999, indicating a good fit.

TABLE 4.3. Calculated nucleation parameters for $Zr_{80}Pt_{20}$ at the average supercooling for different approximations of ΔG and the assumed temperature dependence of σ.

Approximation [a]	A^* $(m^3s)^{-1}$	W^*/k_BT	σ (J/m^2) [b]	σ_0 (J/m^2K) [c]
Turnbull, $\sigma = constant$	$8.76x10^{45}$	84.17	0.134	
Turnbull, $\sigma \propto T$	$2.19x10^{35}$	59.75	0.119	$1.02x10^{-4}$
Thompson-Spaepen, $\sigma = constant$	$2.44x10^{52}$	99.01	0.132	
Thompson-Spaepen, $\sigma \propto T$	$2.91x10^{38}$	66.95	0.116	$9.87x10^{-5}$

[a] The approximation used for the driving free energy and assumption made about the dependence of σ on temperature.

[b] The value of σ, when assumed to be a constant, or calculated at T_u, the average supercooling temperature, when assumed to be linearly temperature dependent.

[c] The temperature coefficient (σ_0) for $\sigma = \sigma_0 T$.

The results of the fitted probability distribution using the Diffuse Interface Theory are tabulated below in Table 4.4. As previously discussed, the shape of the fitted curve did not change with the theory or approximation used; as such, the histograms and fitted curves are not reproduced. The results are tabulated below for the three compositions studied and for the two approximations of ΔG outlined earlier (Eq. 4.5.1 and 4.5.2).

TABLE 4.4. Calculated nucleation parameters for all compositions using the Diffuse Interface Theory

Sample	Approximation [a]	A^* $(m^3s)^{-1}$	W^*/k_BT	δ (Å) [b]
$Ti_{39.5}Zr_{39.5}Ni_{21}$	Turnbull	$1.15x10^{24}$	30.4	0.76
$Ti_{39.5}Zr_{39.5}Ni_{21}$	Thompson-Spaepen	$1.50x10^{25}$	36.6	0.74
$Ti_{40}Zr_{30}Ni_{30}$	Turnbull	$5.68x10^{35}$	61.5	1.12
$Ti_{40}Zr_{30}Ni_{30}$	Thompson-Spaepen	$1.95x10^{39}$	69.6	1.10
$Zr_{80}Pt_{20}$	Turnbull	$6.81x10^{39}$	70.1	1.57
$Zr_{80}Pt_{20}$	Thompson-Spaepen	$7.44x10^{45}$	84.0	1.52

[a] The approximation used for the driving free energy.

[b] The value of δ calculated at the maximum supercooling temperature T_u.

4.4 Discussion

The general trend for σ for the alloy liquids is consistent with previous studies [28]. When σ is assumed to be temperature independent, it has values ranging from 0.1 to 0.4 J/m^2. When σ is assumed to be linearly dependent on temperature ($\sigma = \sigma_0 T$), σ_0 has a value near 10^{-5} J/m^2K. From the results of the present experiments, W^* and σ appear to be insensitive to the approximation (Turnbull or Thompson-Spaepen) used to estimate the driving free energy. This is also true when σ is taken as temperature-independent or linearly temperature dependent (Tables 4.1, 4.2, and 4.3). However, some difference in A^* is noticed under different approximations. The most important finding is that the maximum supercooling, W^*, and σ are approximately a factor of two larger for $Ti_{40}Zr_{30}Ni_{30}$ and $Zr_{80}Pt_{20}$ than $Ti_{39.5}Zr_{39.5}Ni_{21}$ for all of the different approximations for ΔG.

These results are consistent with Frank's hypothesis. As reported earlier [11,13], the supercooled $Ti_{39.5}Zr_{39.5}Ni_{21}$ liquid has significant local icosahedral order, which correlates with the nucleation of the metastable icosahedral quasicrystal in the first recalescence event (Figure 4.1). In the second recalescence, the metastable quasicrystal transforms into a phase mixture of the polytetrahedral C14 Laves and solid solution phases [12]. While the $Ti_{40}Zr_{30}Ni_{30}$ and $Zr_{80}Pt_{20}$ liquids also contain significant amounts of icosahedral and distorted-icosahedral order [13,15,29,30], the primary nucleating phases are the C14 Laves phase for the former and a simultaneous mixture of Zr_5Pt_3 and βZr [14–16] for the latter. Although both the C14 Laves [13] and the intermetallic Zr_5Pt_3 [15,16] phases contain some degree of tetrahedral and distorted icosahedral order, they are structurally more different from the liquid than the quasicrystal is to the $Ti_{39.5}Zr_{39.5}Ni_{21}$ liquid. Following Frank, this difference in structural order raises the energy barrier for nucleation, manifest as an increase in the interfacial free energy. Interestingly, the interfacial free energy for $Ti_{40}Zr_{30}Ni_{30}$ is larger than that for $Ti_{39.5}Zr_{39.5}Ni_{21}$, but smaller than that for $Zr_{80}Pt_{20}$. This could arise because the degree of icosahedral and distorted icosahedral order in the $Ti_{40}Zr_{30}Ni_{30}$ and $Zr_{80}Pt_{20}$ liquids is different and/or because the structures of the primary nucleating phases are different. The tetrahedral Laves phases are known to have a small nucleation barrier because the local tetrahedral order in the icosahedral structure of the liquid is similar to that in the Laves phase. However, due to the simultaneous nucleation of the solid solution phase and Zr_5Pt_3 [14] (deduced from *in-situ* synchrotron X-ray measurements [15]) other factors, both kinetic and thermodynamic, could also contribute [31,32]. These would also be manifest as a larger interfacial free energy for $Zr_{80}Pt_{20}$ compared to $Ti_{40}Zr_{30}Ni_{30}$. Clearly, however, the results for the $Ti_{39.5}Zr_{39.5}Ni_{21}$ and $Ti_{40}Zr_{30}Ni_{30}$ liquids show that a lower interfacial free energy correlates with a greater structural similarity between the liquid and the nucleating phase, which is consistent with Frank's hypothesis.

Using a different technique, Lee *et. al.* studied the nucleation of $Ti_{39.5}Zr_{39.5}Ni_{21}$ [12], and observed similar values for the maximum undercooling. Since then, the method for calculating sample density has improved [20] and the statistical method outlined in this paper requires fewer assumptions for I^{ST} and A^* to calculate σ. As a check, the method proposed by Lee *et. al.* was also used to calculate σ. The density was first corrected, the value for A^* obtained from fitting the undercooling distribution was used, the Turnbull approximation was assumed for the free energy, and a temperature-independent σ was assumed. The values obtained for W^*/k_BT and σ were 34.5 and 0.055 (J/m^2) respectively, which are in closer agreement with those results found from the statistical method used here. These values are smaller than those found in other alloy liquids, such as Zr-Ni [33]. This is reasonable because of the structural similarity between the liquid and primary nucleation phase in $Ti_{39.5}Zr_{39.5}Ni_{21}$. As discussed, the structures are more different in $Ti_{40}Zr_{30}Ni_{30}$, Zr-Ni, and $Zr_{80}Pt_{20}$. It should also be noted that a larger maximum supercooling was observed for $Ti_{40}Zr_{30}Ni_{30}$ in this study than in the previous reported results [12]. Using our improved measurements of the density, the calculated values for W^* and σ are larger than those reported by Lee *et. al*, likely indicating a cleaner processing environment in the present study.

The values for δ obtained by fitting the data assuming the Diffuse Interface Theory agree with the results calculated using the Classical Theory. The smallest value of δ corresponds to nucleation in the $Ti_{39.5}Zr_{39.5}Ni_{21}$ liquid, which implies a small difference between the enthalpy and entropy curves for the liquid and quasicrystal phases. Since the local order in supercooled $Ti_{39.5}Zr_{39.5}Ni_{21}$ is icosahedral, the small difference reflects a similar structural and chemical order in the quasicrystal phase. Interestingly, $Ti_{40}Zr_{30}Ni_{30}$ has a somewhat larger value for δ than $Ti_{39.5}Zr_{39.5}Ni_{21}$, yet not as large as the δ for $Zr_{80}Pt_{20}$. In Ti-Zr-Ni alloys, the C14 Laves phase is a common crystal structure that has some icosahedral-like motifs. Thus, local icosahedral order may slightly reduce the free energy difference between the two phases in $Ti_{40}Zr_{30}Ni_{30}$; however, the local icosahedral order in the supercooled $Ti_{40}Zr_{30}Ni_{30}$ contributes to a larger barrier to nucleation when compared against $Ti_{39.5}Zr_{39.5}Ni_{21}$. Therefore, the slightly larger δ implies a larger barrier to the nucleation of the crystal phase due to a larger difference between the enthalpy and entropy curves. Meanwhile, the large value for δ in $Zr_{80}Pt_{20}$ indicates a large difference between the enthalpy and entropy curves for the liquid and crystal. As described earlier, this could imply a significant difference in the local order between the liquid and crystal, increasing the barrier for rearranging the liquid atoms into the crystal lattice.

Finally, the different magnitudes of A^* need to be addressed. Based on previous studies of elemental metallic liquids performed by Turnbull, a value approximately 10^{39} $(m^3s)^{-1}$ for A^* was proposed as a benchmark for homogeneous nucleation; smaller values (10^{29} $(m^3s)^{-1}$) were considered indicative of heterogeneous nucleation [34]. More recent levitation studies of pure zirconium are also consistent with this criterion [26,27,35]. For both $Ti_{40}Zr_{30}Ni_{30}$ and $Zr_{80}Pt_{20}$ liquids, the magnitudes of A^* are consistent with homogeneous nucleation, although they are somewhat smaller when σ is taken to be linearly temperature dependent. As previously noted, Turnbull noted that A^* became smaller when a temperature-dependent σ was used, as observed in this study [25]. In contrast, the value of A^* for $Ti_{39.5}Zr_{39.5}Ni_{21}$ might appear to indicate heterogeneous nucleation, since it is 13 to 17 orders of magnitude smaller. This would be surprising for several reasons. As shown in Fig. 4.2, like the case for $Ti_{40}Zr_{30}Ni_{30}$ and $Zr_{80}Pt_{20}$, there was no hint of degradation of supercooling with time/cycling for $Ti_{39.5}Zr_{39.5}Ni_{21}$ during processing. The distribution of maximum supercooling temperatures is similarly asymmetric for all liquids. Finally, the samples were processed in similar high-vacuum conditions and created from the same high-purity elements. All of these observations suggest homogeneous nucleation. As pointed out in an earlier study [11], the nucleation of the i-phase in $Ti_{39.5}Zr_{39.5}Ni_{21}$ is favored in regions of the liquid that develop significant ISRO. The icosahedral-ordered regions in the liquid catalyze the nucleation of the icosahedral phase, much like the case of heterogeneous nucleation. The limited number of these favored regions in $Ti_{39.5}Zr_{39.5}Ni_{21}$ gives a smaller nucleation pre-factor than for the cases of $Ti_{40}Zr_{30}Ni_{30}$ and $Zr_{80}Pt_{20}$, which follow a more normal interpretation of homogeneous nucleation within the Classical Theory. More extensive studies in other alloy liquids are planned in the future to investigate this further.

4.5 Conclusions

A systematic statistical study of hundreds of maximum supercooling measurements for $Ti_{39.5}Zr_{39.5}Ni_{21}$, $Ti_{40}Zr_{30}Ni_{30}$, and $Zr_{80}Pt_{20}$ was performed and nucleation parameters were calculated using the Classical Nucleation Theory, Diffuse Interface Theory, and the Skripov method. The resulting nucleation parameters were found to provide additional support for Frank's hypothesis, since the smaller values for A^* and W^* found in $Ti_{39.5}Zr_{39.5}Ni_{21}$ are likely due to ISRO in the liquid facilitating nucleation of the metastable quasicrystal. Meanwhile, the larger values for A^* and W^* found in $Ti_{40}Zr_{30}Ni_{30}$ and $Zr_{80}Pt_{20}$ indicate that the structure of the liquid is different from that of the primary crystallizing phases, inhibiting their nucleation. Since the $Zr_{80}Pt_{20}$ simultaneously nucleates two crystal phases, in contrast with primary nucleation to a single phase in the Ti-Zr-Ni liquids, there could be other additional thermodynamic and/or kinetic contributions to nucleation that would be manifest as a larger value of the interfacial free energy in these measurements. In addition to their inherent interest for supporting Frank's hypothesis, these data will serve as a comparison for ongoing nucleation studies on the International Space Station, investigating the role of diffusion and convective stirring on nucleation, and to further understand nucleation in more complex metallic liquids.

4.6 Acknowledgments

This material is based upon work partially supported by the National Science Foundation Graduate Research Fellowship under Grant No. DGE-1745038 and by the National Aeronautics and Space Administration Grant No. NNX16AB52G. The authors would like to thank Chris Pueblo and Robert Ashcraft for providing density and viscosity data.

4.7 References

1. Fahrenheit, D. G. VIII. Experimenta & observationes de congelatione aquæ in vacuo factæ. *Philos. Trans. R. Soc. London* **33**, 78–84 (1724).

2. Gibbs, J. W. *Scientific Papers*. (Longmans, Green, and Co, 1906).

3. Volmer, M. & Weber, A. Keimbildung in übersättigten Gebilden. *Zeitschrift für Phys. Chemie* **119**, 277–301 (1926).

4. Becker, R. & Döring, W. Kinetische Behandlung der Keimbildung in übersättigten Dämpfen. *Ann. Phys.* **416**, 719–752 (1935).

5. Turnbull, D. & Fisher, J. C. Rate of nucleation in condensed systems. *J. Chem. Phys.* **17**, 71–73 (1949).

6. Spaepen, F. Homogeneous nucleation and the temperature dependence of the crystal-melt interfacial tension. in *Solid State Physics* (eds. Ehrenreich, H. & Turnbull, D.) **47**, 1–32 (Academic Press, 1994).

7. Gránásy, L. Diffuse interface theory of nucleation. *J. Non. Cryst. Solids* **162**, 301–303 (1993).

8. Gránásy, L. Nucleation theory for diffuse interfaces. *Mater. Sci. Eng. A* **178**, 121–124 (1994).

9. Frank, F. C. Supercooling of Liquids. *Proc. R. Soc. London.* **215**, 43–46 (1952).

10. Holland-Moritz, D., Schenk, T., Simonet, V., Bellissent, R. & Convert, P. Short-range order in undercooled melts forming quasicrystals and approximants. *J. Alloys Compd.* **342**, 77–81 (2002).

11. Kelton, K. F. *et al.* First X-Ray Scattering Studies on Electrostatically Levitated Metallic Liquids: Demonstrated Influence of Local Icosahedral Order on the Nucleation Barrier.

Phys. Rev. Lett. **90**, 195504 (2003).

12. Lee, G. W. *et al.* Link between liquid structure and the nucleation barrier for icosahedral quasicrystal, polytetrahedral, and simple crystalline phases in Ti-Zr-Ni alloys: Verification of Frank’s hypothesis. *Phys. Rev. B* **72**, 174107 (2005).

13. Lee, G. W. *et al.* Local structure of equilibrium and supercooled Ti-Zr-Ni liquids. *Phys. Rev. B* **77**, 1–8 (2008).

14. Okamoto, H. Pt-Zr (Platinum-Zirconium). *J. Phase Equilibria Diffus.* **29**, 385–385 (2008).

15. Johnson, M. L. *et al.* Measurements of structural and chemical order in Zr80 Pt20 and Zr77 Rh23 liquids. *Phys. Rev. B* **93**, 054203 (2016).

16. Mauro, N. A. *et al.* Short- and medium-range order in Zr80Pt20 liquids. *Phys. Rev. B* **83**, 184109 (2011).

17. Gangopadhyay, A. K. *et al.* Beamline electrostatic levitator for in situ high energy x-ray diffraction studies of levitated solids and liquids. *Rev. Sci. Instrum.* **76**, 073901 (2005).

18. Mauro, N. A. & Kelton, K. F. A highly modular beamline electrostatic levitation facility, optimized for in situ high-energy x-ray scattering studies of equilibrium and supercooled liquids. *Rev. Sci. Instrum.* **82**, 035114 (2011).

19. Bendert, J. C., Pueblo, C. E., Veligati, S., Mauro, N. A. & Kelton, K. F. Temperature calibration for optical pyrometry in containerless systems using differential scanning calorimetry: Application to Cu100−xZrx(x = 45–50). *Int. J. Thermophys.* **35**, 1687–1696 (2014).

20. Bendert, J. C. & Kelton, K. F. Containerless measurements of density and viscosity for a Cu48Zr52liquid. *Int. J. Thermophys.* **35**, 1677–1686 (2014).

21. Skripov, V. P. Homogeneous Nucleation in Melts and Amorphous Films. *Curr. Top. Mater. Sci.* **2**, 328–378 (1977).

22. Thompson, C. V & Spaepen, F. On the Approximation of the Free Energy Change on Crystallization. *Acta Metall.* **27**, 1855 (1979).

23. Kubaschewski, O. & Alcock, C. B. *Metallurgical Thermochemistry*. (Pergamon Press, 1979).

24. Turnbull, D. Physics of non-crystalline solids. in *Physics of Non-crystalline Solids. Proc Int Conf. Prins JA edition* 41–56 (North-Holland, Amsterdam, 1964).

25. Turnbull, D. Kinetics of Solidification of Supercooled Liquid Mercury Droplets. *J. Chem. Phys.* **20**, 411–424 (1952).

26. Klein, S., Holland-Moritz, D. & Herlach, D. M. Crystal nucleation in undercooled liquid zirconium. *Phys. Rev. B* **80**, 2–5 (2009).

27. Morton, C. W., Hofmeister, W. H., Bayuzick, R. J., Rulison, A. J. & Watkins, J. L. The kinetics of solid nucleation in zirconium. *Acta Mater.* **46**, 6033–6039 (1998).

28. Kelton, K. F. Crystal Nucleation in Liquids and Glasses. *Solid State Phys. - Adv. Res. Appl.* **45**, 75–177 (1991).

29. Saida, J. *et al.* Evaluation of the local environment for nanoscale quasicrystal formation in Zr80Pt20 glassy alloy using Voronoi analysis. *J. Phys. Condens. Matter* **21**, 375104

(2009).

30. Celtek, M. & Sengul, S. Thermodynamic and dynamical properties and structural evolution of binary Zr80Pt20metallic liquids and glasses: Molecular dynamics simulations. *J. Non. Cryst. Solids* **498**, 32–41 (2018).

31. Kelton, K. F. Time-Dependent Nucleation in Partitioning Transformations. *Acta Mater.* **48**, 1967–1980 (2000).

32. Thompson, C. V. & Spaepen, F. Homogeneous binary metallic melts in binary metallic melts. *Acta Metall.* **31**, 2021–2027 (1983).

33. Kobold, R., Kolbe, M., Hornfeck, W. & Herlach, D. M. Nucleation study for an undercooled melt of intermetallic NiZr. *J. Chem. Phys.* **148**, 114502 (2018).

34. Turnbull, D. Formation of crystal nuclei in liquid metals. *J. Appl. Phys.* **21**, 1022–1028 (1950).

35. Wert, M. J., Hofmeister, W. H. & Bayuzick, R. J. Effect of dilute amounts of oxygen solute on nucleation of zirconium. *J. Appl. Phys.* **93**, 3643–3651 (2003).

Chapter 5: Maximum Supercooling Studies in Zr-Pd and Cu-Zr Binary Alloy Families

5.1 Introduction

Frank's hypothesis establishes a connection between the nucleation barrier and local atomic order in the supercooled liquid. However, questions remain about how the nucleation of multiple phases impacts the nucleation barrier. The Classical Theory of Nucleation (CNT) does not explicitly consider the role of local order in the supercooled liquid on the nucleation barrier; however, a systematic study of several different compositions within the same alloy family may shed light on the role of multiple phase formation in nucleation. The Diffuse Interface Theory (DIT) can be used to provide insight into the entropy surface between the liquid and crystal phases.

As discussed earlier in Section 1.2, within the CNT the steady-state rate for forming crystal nuclei is expressed in terms of the atomic mobility at the crystal-liquid interface (contained in the pre-term A^*), the work required to form the initial critical cluster W^*, and the temperature T (Eq. 5.1).

$$I^{ST} = A^* \exp\left(-\frac{W^*}{k_B T}\right) \tag{5.1}$$

Within CNT, the work to form the critical nucleus, W^*, for a spherical nucleus is (Eq. 5.2):

$$W^* = \frac{16\pi}{3}\frac{\sigma^3}{\Delta g^2} \tag{5.2}$$

where Δg is the Gibbs free energy difference per unit volume ($\Delta g = \Delta\mu/\bar{v}$, where $\bar{v}$ is the atomic volume) and σ is the interfacial free energy. Turnbull and Fisher [1] assumed that the attachment mobility at the interface, contained within the pre-term A^*, was related to the diffusion coefficient in the liquid, D. This is generally obtained from the viscosity, η, assuming the Stokes-Einstein relation ($D = k_B T/6\pi\eta a$), where a is a length that corresponds approximately to the atomic diameter.

The critical radius r^*, typically in units of nanometers, is (Eq. 5.3):

$$r^* = \frac{2\sigma}{|\Delta g|} \tag{5.3}$$

However, CNT assumes a sharp interface between the liquid and crystal, which can fail to accurately describe ordering in the liquid at the interface of the nuclei. An extension of CNT was developed independently by both Spaepen [2] and Gránásy to account for extended (or diffuse) interfaces [3,4]. Within DIT, the critical work of cluster formation is (Eq. 5.4):

$$W^* = -\kappa\delta^3\Delta g_0\psi(\eta) \tag{5.4}$$

where $\kappa = 4\pi/3$, $\Delta g_0 = \Delta h_0 - T\Delta s_0$, $\psi(\eta) = 2(1+q)\eta^{-3} - (3+2q)\eta^{-2} + \eta^{-1}$, $q = (1-\eta)^{-1/2}$, $\eta = \Delta g_0/\Delta h_0$, Δh_0 and Δs_0 are the enthalpy and entropy differences between the parent and new phase, and δ is the interfacial thickness defined by the difference in location between the enthalpy and entropy surfaces ($\delta = R_S - R_H$). Within DIT, the critical radius is defined as (Eq. 5.5):

$$r^* = \delta(1+q)\eta^{-1} \tag{5.5}$$

The steady-state nucleation rate within DIT has the same form as Eq. 5.1.

The Cu-Zr and Zr-Pd binary alloy families were chosen partially based on previous studies. Cu-Zr is a well-studied system in both experimental and simulation settings and has been shown to be a bulk metallic-glass former [5]. Zr-Pd was chosen since Pd is in the same noble-metal family as Pt yet melts at significantly lower temperatures. This last point is key for future studies of this system using the Electromagnetic Levitation (EML) on-board the International Space Station (ISS), as the liquidus temperature for intermetallic Zr-Pt exceeds the maximum temperature threshold of the EML. Finally, the three different compositions within each family were chosen because intermetallic alloys typically nucleate a single phase, while eutectic and other compositions typically nucleate multiple phases. This can be seen in the phase diagrams for both Cu-Zr and Zr-Pd [6–10]. By comparing the nucleation parameters within each family and examining the overall trend, it may be possible to understand the impact of multiple phase formation and local order on nucleation.

5.2 Methods

Master ingots of $Zr_{50}Pd_{50}$, $Pd_{55}Zr_{45}$, $Zr_{75.5}Pd_{24.5}$, $Cu_{50}Zr_{50}$, $Cu_{55}Zr_{45}$, and $Cu_{64}Zr_{36}$ were prepared similarly to previously outlined methods and experiments. High purity Zr (Smart Elements, Vienna, 99.97 at.%), Pd (Alfa Aesar, 99.95 at.%), and Cu (Alfa Aesar, 99.999 at. %) were arc-melted together under a high purity Ar (99.999 at.%) atmosphere. The master ingots were melted and flipped three times with each melt cycle lasting approximately 15 seconds to ensure chemical homogeneity and minimize mass loss due to evaporation. The mass of the ingot after arc-melting was verified to ensure a negligible change (less than 0.1%) and subsequently broken into pieces, which were then remelted into spherical samples approximately 2.5mm in diameter.

The Washington University Beamline Electrostatic Levitator (WU-BESL) [11,12] was used to containerlessly process these samples under high vacuum conditions. $Zr_{50}Pd_{50}$ samples were processed at 7.0x10^{-8} Torr, $Pd_{55}Zr_{45}$ samples were processed at 6.8x10^{-8} Torr, and $Zr_{75.5}Pd_{24.5}$ samples were processed at 6.4x10^{-8} Torr. The $Cu_{50}Zr_{50}$ sample was processed at 8.0x10^{-8} Torr, $Cu_{55}Zr_{45}$ was processed at 6.4x10^{-8} Torr, and $Cu_{64}Zr_{36}$ was processed at 6.0x10^{-8} Torr. To calibrate the Process Sensors Metis MI18 MB8 single-color pyrometer and MQ22 two-color ratio pyrometer, the melting plateau of 1600 °C for $Zr_{50}Pd_{50}$, 1560 °C for $Pd_{55}Zr_{45}$, 1053 °C for $Zr_{75.5}Pd_{24.5}$, 904 °C for $Cu_{50}Zr_{50}$ and $Cu_{55}Zr_{45}$, and 933 °C for $Cu_{64}Zr_{36}$ were used. The density and viscosity were obtained by the shadow method and oscillating drop technique respectively, as outlined earlier [13–15].

5.3 Analysis

The solid spherical samples were levitated, melted, and heated above the liquidus temperature several times to achieve maximum supercooling. In some cases, like for $Zr_{50}Pd_{50}$, the liquid was heated no more than 50 to 100 degrees above the liquidus, since the high melting temperature assisted in sample conditioning but could also result in significant mass loss due to the high vapor pressure of palladium. This can be seen below in Fig. 5.1. For samples in the Cu-Zr family, the liquid was typically heated 100 to 150 degrees above the liquidus. Due to the prolonged experiments, it is important to prevent as much mass loss as possible since these alloys typically have high vapor pressures. The maximum supercooling achieved occurred immediately before recalescence, the characteristic jump in sample temperature that followed the release of the heat of fusion.

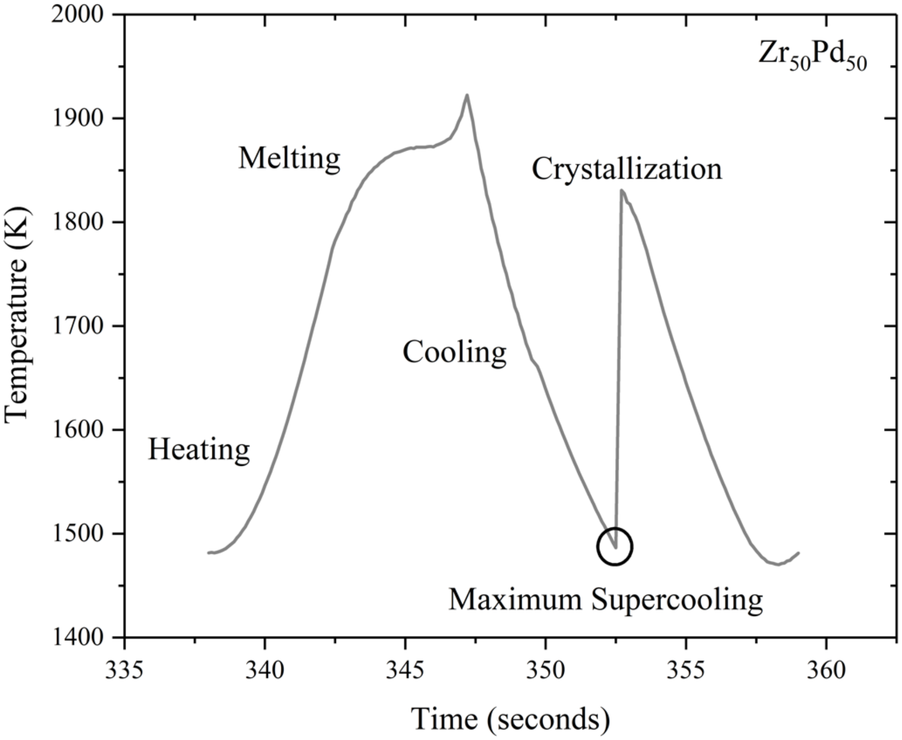

Figure 5.1: A representative heating and cooling cycle for Zr$_{50}$Pd$_{50}$. Note that, almost immediately after the sample has transformed from solid to liquid, the heating laser is turned off to prevent overheating of the sample and potential mass loss due to evaporation.

The first 25 to 50 cycles were excluded from analysis until a deep and consistent maximum supercooling temperature was achieved. As discussed earlier, this was due to sample conditioning, whereby impurities and gas trapped in the grain boundaries were gradually evaporated from the sample with each successive thermal cycle. In Fig. 5.2, the maximum supercooling is plotted against cycle number to check the consistency of each supercooling cycle. The R-value calculated from the linear regression showed no significant evidence of a dependence between supercooling and cycle number ($p > 0.05$). To calculate the maximum supercooling ($\Delta T = T_l - T_u$), the liquidus temperature must be known. For Zr$_{50}$Pd$_{50}$ and Pd$_{55}$Zr$_{45}$, the liquidus temperatures (1873 K and 1833K) were measured from the phase diagram for Pd-Zr [9,10] and verified from other published data [8]. For Zr$_{75.5}$Pd$_{24.5}$, an equilibrium liquidus temperature of 1326 K was determined from DTA measurements. For the Cu-Zr family, the 2012 phase diagram by Okamoto served as the first reference for the equilibrium liquidus temperatures [6], which were then verified from other published data. For $Cu_{50}Zr_{50}$, $Cu_{55}Zr_{45}$, and $Cu_{64}Zr_{36}$, the equilibrium liquidus temperatures were used (1208 K [6,7], 1193K [16], and 1250 K [17] respectively).

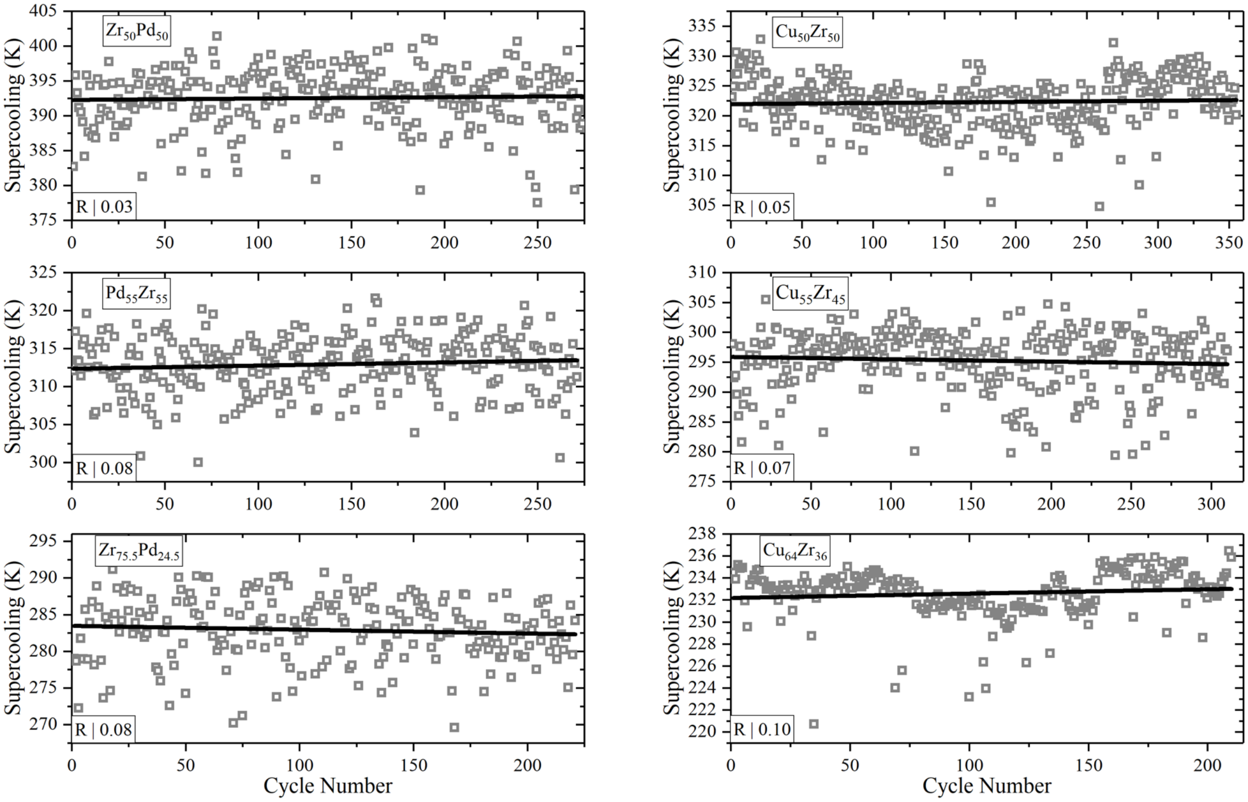

Figure 5.2: Maximum supercooling as a function of cycle number for both Zr-Pd (left) and Cu-Zr (right) binary alloy families. No significant dependence between supercooling and cycle number is observed, indicating the nucleation was reproducible for each sample studied; 1,641 measurements are represented.

The Skripov method [18] was used to obtain values for the nucleation pre-factor and work of cluster formation. The probability density is given below (Eq. 5.6):

$$\omega(T) = \frac{I^{ST}V}{\dot{T}} \exp\left(-\frac{V}{\dot{T}}\int_{T_u}^{T_l} I^{ST}\,dT\right) \tag{5.6}$$

where $I^{ST} = A^{*}\exp(-W^{*}/k_{B}T)$ is the steady-state nucleation rate, A^{*} is the classical nucleation pre-term divided by the viscosity, V is the volume of the droplet, and $\dot{T}$ is the cooling rate (dT/dt). Equation 5.6 was fit to the histogram of supercooling measurements by a non-linear, least squares fitting routine. The definitions of I^{ST} from both the CNT and DIT were used to calculate values for the pre-factor and work of cluster formation. This required the use of approximations for the driving free energy. As explained earlier in Section 1.2, the two approximations used were the Turnbull approximation [19] and Thompson-Spaepen [20] approximation:

$$\Delta G = \frac{\Delta H_{f}\Delta T}{T_{l}} \tag{5.7.1}$$

$$\Delta G = \frac{\Delta H_{f}\Delta T}{T_{l}}\frac{2T}{T_{l}+T} \tag{5.7.2}$$

where ΔH_f is the enthalpy of fusion. The driving free energy per atom, $\Delta\mu$, is obtained by normalizing ΔG by N_A. The enthalpy of fusion was obtained from previously reported results for $Cu_{50}Zr_{50}$ ($\Delta H_f = 7.51$ kJ/mol) [21] and $Cu_{64}Zr_{36}$ ($\Delta H_f = 9.96$ kJ/mol) [22]. The enthalpy of fusion for $Cu_{55}Zr_{45}$ was assumed to be very similar to that of $Cu_{50}Zr_{50}$, given their similar liquidus and solidus temperatures. For the Zr-Pd family, Richard's Rule [23] was used to estimate the enthalpy of fusion for $Zr_{50}Pd_{50}$ ($\Delta H_f = 15.0$ kJ/mol), $Pd_{55}Zr_{45}$ ($\Delta H_f = 14.7$ kJ/mol), and $Zr_{75.5}Pd_{24.5}$ ($\Delta H_f = 10.6$ kJ/mol). The viscosity was used as an input parameter after it had been fit with the KKZNT form [24]. The interfacial free energy σ was also calculated twice, assuming it to be temperature independent (σ) or assuming a linear temperature dependence ($\sigma = \sigma_0 T$). A^{*} and W^{*} were used as fit parameters, assuming the temperature dependence based on the choice of approximation for the driving free energy and interfacial free energy. From the fit parameters, σ and r^{*} may be calculated directly from Eq. 5.2 and 5.3. Within the DIT, δ and r^* were calculated from the fit parameters using Eq. 5.4 and 5.5.

X-ray scattering data on Cu-Zr and $Zr_{75.5}Pd_{24.5}$ were obtained from the BESL2013 and BESL2016 runs, as outlined elsewhere [25]. Other studies on $Zr_{50}Pd_{50}$ and $Pd_{55}Zr_{45}$ have explored the crystal structure of these compositions at various temperatures [8]. The X-ray data was reduced in the same way outlined in Chapter 2. Using published lattice parameters for Cu-Zr [7] and Zr-Pd [26] and using the reflection conditions for the respective space groups, [27] the Bragg scattering for each Miller plane was calculated and mapped onto the structure factor $S(q)$.

Finally, the mass of the sample after processing was checked to ensure minimal mass loss. For every sample studied here, the difference in mass before and after processing was typically 0.1% and no larger than 0.3%. As such, any compositional change was marginal and negligible.

5.4 Results

A total of 274 supercooling measurements were obtained for a 59.32mg sample of $Zr_{50}Pd_{50}$, with an average supercooling temperature of 393°C (21.0% supercooling). As seen in previous publications [28], the shape of the distribution is asymmetric, as proscribed by Poisson statistics. The sharp decrease in supercooling above the average is typically characteristic of homogeneous nucleation, as the maximum supercooling temperature was achieved [29,30]. The average supercooling was used to calculate the values in Table 5.1 below.

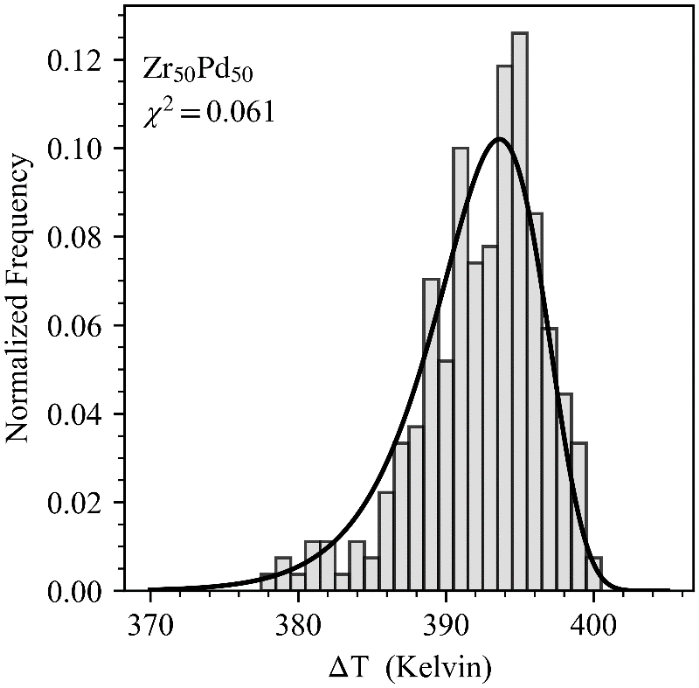

Figure 5.3: The histogram of maximum supercooling measurements for $Zr_{50}Pd_{50}$. The average supercooling was 393°C (21.0%). The curve is the fitted probability density with a p-value > 0.999, indicating a good fit.

TABLE 5.1. Calculated nucleation parameters for $Zr_{50}Pd_{50}$ at the average supercooling for different approximations of ΔG and the assumed temperature dependence of σ.

Approximation [a]	A^* $(m^3s)^{-1}$	W^*/k_BT	r^* (nm)	σ (J/m^2) [b]	σ_0 (J/m^2K) [c]
Turnbull, $\sigma = constant$	$4.30x10^{36}$	62.65	1.30	0.182	
Turnbull, $\sigma \propto T$	$1.08x10^{28}$	42.84	1.14	0.160	$1.08x10^{-4}$
Thompson-Spaepen, $\sigma = constant$	$1.68x10^{42}$	75.52	1.44	0.178	
Thompson-Spaepen, $\sigma \propto T$	$3.43x10^{30}$	48.60	1.24	0.154	$1.04x10^{-4}$

[a] The approximation used for the driving free energy and assumption made about the dependence of σ on temperature.

[b] The value of σ, when assumed to be a constant, or calculated at T_u, the average supercooling temperature, when assumed to be linearly temperature dependent.

[c] The temperature coefficient (σ_0) for $\sigma = \sigma_o T$.

A total of 271 supercooling measurements were obtained for a 52.52mg sample of $Pd_{55}Zr_{45}$, giving an average supercooling temperature of 313°C (17.1% supercooling). The average supercooling is smaller than that of $Zr_{50}Pd_{50}$ despite the proximity in composition and liquidus temperatures. The fit parameters from the distribution calculated at the average supercooling and the extracted nucleation values using the classical theory are listed below in Table 5.2.

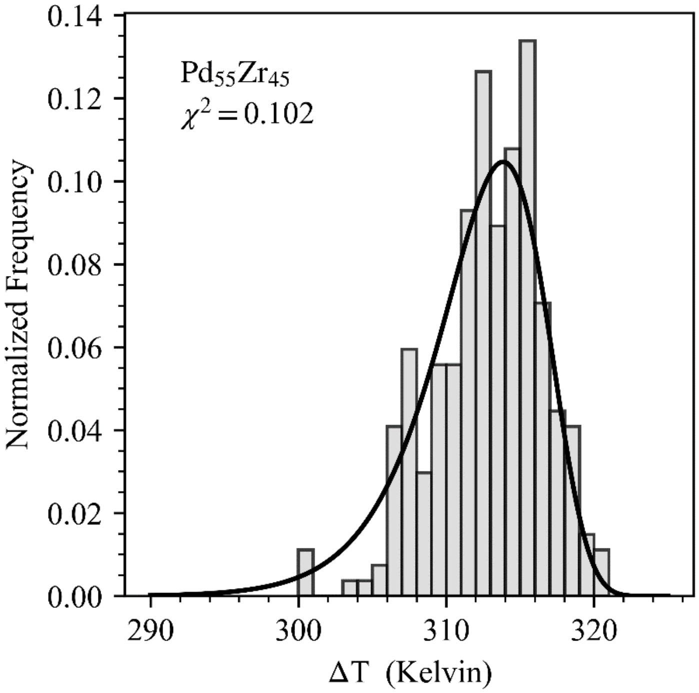

Figure 5.4: The histogram of maximum supercooling measurements for $Pd_{55}Zr_{45}$. The average supercooling was 313°C (17.1%). The curve is the fitted probability density with a p-value > 0.999, indicating a good fit.

TABLE 5.2. Calculated nucleation parameters for $Pd_{55}Zr_{45}$ at the average supercooling for different approximations of ΔG and the assumed temperature dependence of σ.

Approximation [a]	A^* $(m^3s)^{-1}$	W^*/k_BT	r^* (nm)	σ (J/m^2) [b]	σ_0 (J/m^2K) [c]
Turnbull, σ = *constant*	2.23×10^{31}	50.25	1.30	0.149	
Turnbull, $\sigma \propto T$	5.59×10^{25}	37.35	1.18	0.135	8.89×10^{-5}
Thompson-Spaepen, σ = *constant*	3.04×10^{34}	57.47	1.40	0.146	
Thompson-Spaepen, $\sigma \propto T$	2.70×10^{27}	41.23	1.26	0.131	8.60×10^{-5}

[a] The approximation used for the driving free energy and assumption made about the dependence of σ on temperature.

[b] The value of σ, when assumed to be a constant, or calculated at T_u, the average supercooling temperature, when assumed to be linearly temperature dependent.

[c] The temperature coefficient (σ_0) for $\sigma = \sigma_o T$.

A total of 221 measurements were obtained for a 55.89mg sample of $Zr_{75.5}Pd_{24.5}$, with an average supercooling of 283°C (21.3% supercooling). While the overall magnitude of supercooling for this composition is the smallest within the studied Zr-Pd family, the percentage supercooling is the largest. However, the calculated parameters at the average supercooling in Table 5.3 are still the smallest of the Zr-Pd alloys studied here.

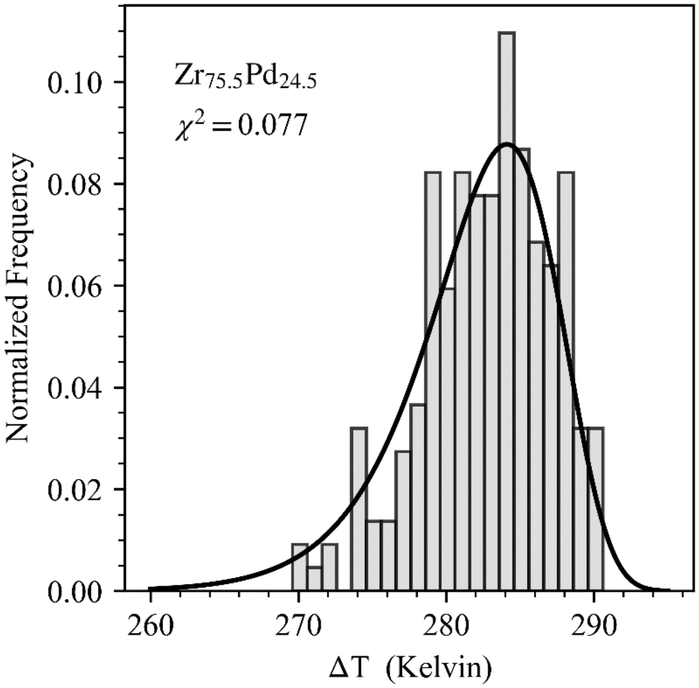

Figure 5.5: The histogram of maximum supercooling measurements for $Zr_{75.5}Pd_{24.5}$. The average supercooling was 283°C (21.3%). The curve is the fitted probability density with a p-value > 0.999, indicating a good fit.

TABLE 5.3. Calculated nucleation parameters for $Zr_{75.5}Pd_{24.5}$ at the average supercooling for different approximations of ΔG and the assumed temperature dependence of σ.

Approximation [a]	A^* $(m^3s)^{-1}$	W^*/k_BT	r^* (nm)	σ (J/m^2) [b]	σ_0 (J/m^2K) [c]
Turnbull, $\sigma = constant$	$1.63x10^{26}$	40.15	1.15	0.104	
Turnbull, $\sigma \propto T$	$3.97x10^{20}$	27.22	1.01	0.092	$8.79x10^{-5}$
Thompson-Spaepen, $\sigma = constant$	$8.27x10^{29}$	48.68	1.28	0.102	
Thompson-Spaepen, $\sigma \propto T$	$1.70x10^{22}$	30.98	1.10	0.088	$8.43x10^{-5}$

[a] The approximation used for the driving free energy and assumption made about the dependence of σ on temperature.

[b] The value of σ, when assumed to be a constant, or calculated at T_u, the average supercooling temperature, when assumed to be linearly temperature dependent.

[c] The temperature coefficient (σ_0) for $\sigma = \sigma_0 T$.

Using the DIT to fit the probability density to the histogram of supercoolings did not result in a change in the overall shape of the fitted curve. The histograms for Zr-Pd using the DIT are thus not reproduced. The best fit values calculated at the average supercooling and the corresponding driving free energy approximation are listed in Table 5.4.

TABLE 5.4. Calculated nucleation parameters for Zr-Pd family using the Diffuse Interface Theory

Sample	Approximation [a]	A^* (m^{3}s)$^{-1}$	W^*/k_BT	r^* (nm)	δ (Å) [b]
$Zr_{50}Pd_{50}$	Turnbull	4.07x10^{31}	51.08	1.29	1.43
$Zr_{50}Pd_{50}$	Thompson-Spaepen	5.99x10^{36}	62.98	1.43	1.39
$Pd_{55}Zr_{45}$	Turnbull	1.49x10^{28}	42.94	1.29	1.15
$Pd_{55}Zr_{45}$	Thompson-Spaepen	1.43x10^{39}	49.80	1.40	1.13
$Zr_{75.5}Pd_{24.5}$	Turnbull	8.32x10^{22}	32.57	1.14	1.29
$Zr_{75.5}Pd_{24.5}$	Thompson-Spaepen	2.16x10^{26}	40.43	1.27	1.25

[a] The approximation used for the driving free energy.

[b] The value of δ calculated at the maximum supercooling temperature T_u.

A total of 355 measurements were acquired from three different samples of $Cu_{50}Zr_{50}$, ranging in mass from 55.91mg to 57.92mg. The slight differences in sample volume were considered by normalizing for the different masses. The average supercooling was found to be 322°C (27.0% supercooling), which was typically accompanied by significant hypercooling during recalescence. The average supercooling was used to calculate the parameters obtained from the fit curve, which are listed in Table 5.5.

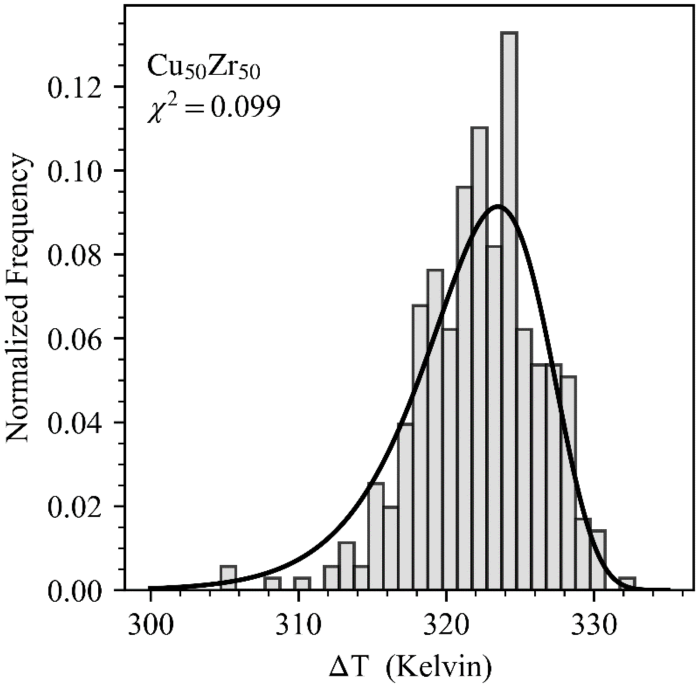

Figure 5.6: The histogram of maximum supercooling measurements for $Cu_{50}Zr_{50}$. The average supercooling was 322°C (27.0%). The curve is the fitted probability density with a p-value > 0.999, indicating a good fit.

TABLE 5.5. Calculated nucleation parameters for $Cu_{50}Zr_{50}$ at the average supercooling for different approximations of ΔG and the assumed temperature dependence of σ.

Approximation [a]	A^* $(m^3s)^{-1}$	W^*/k_BT	r^* (nm)	σ (J/m^2) [b]	σ_0 (J/m^2K) [c]
Turnbull, σ = *constant*	$2.47x10^{31}$	52.85	1.17	0.113	
Turnbull, $\sigma \propto T$	$1.56x10^{22}$	31.66	0.98	0.092	$1.08x10^{-4}$
Thompson-Spaepen, σ = *constant*	$1.86x10^{39}$	70.99	1.21	0.141	
Thompson-Spaepen, $\sigma \propto T$	$5.24x10^{24}$	37.48	1.10	0.087	$1.02x10^{-4}$

[a] The approximation used for the driving free energy and assumption made about the dependence of σ on temperature.

[b] The value of σ, when assumed to be a constant, or calculated at T_u, the average supercooling temperature, when assumed to be linearly temperature dependent.

[c] The temperature coefficient (σ_0) for $\sigma = \sigma_o T$.

For $Cu_{55}Zr_{45}$, a total of 310 measurements from two samples of mass 55.91mg and 60.42mg were obtained. Like for $Cu_{50}Zr_{50}$, the slight difference in sample volume was normalized. The average supercooling was found to be 295°C (24.7% supercooling), which was used to calculate the fit parameters listed in Table 5.6.

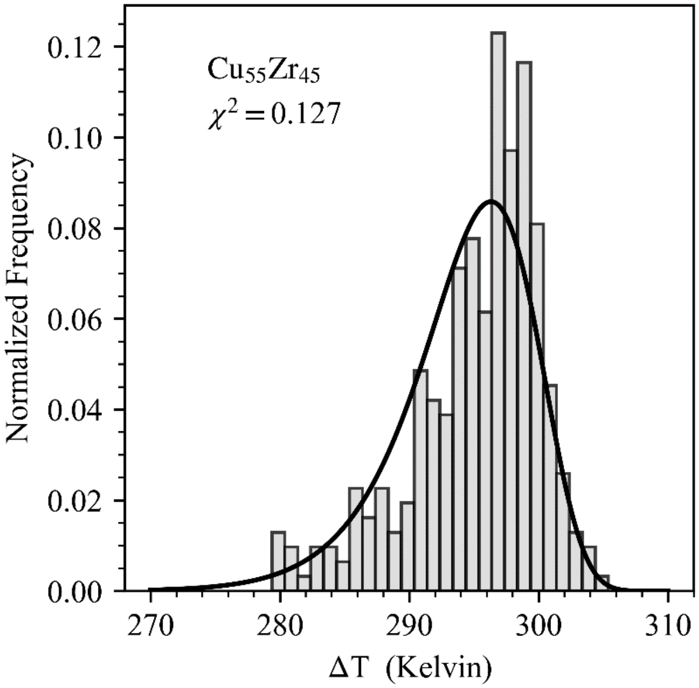

Figure 5.7: The histogram of maximum supercooling measurements for $Cu_{55}Zr_{45}$. The average supercooling was 295°C (24.7%). The curve is the fitted probability density with a p-value > 0.999, indicating a good fit.

TABLE 5.6. Calculated nucleation parameters for $Cu_{55}Zr_{45}$ at the average supercooling for different approximations of ΔG and the assumed temperature dependence of σ.

Approximation [a]	A^* $(m^3s)^{-1}$	W^*/k_BT	r^* (nm)	σ (J/m^2) [b]	σ_0 (J/m^2K) [c]
Turnbull, $\sigma = constant$	$7.42\text{x}10^{27}$	44.82	1.12	0.105	
Turnbull, $\sigma \propto T$	$3.97\text{x}10^{20}$	28.07	0.96	0.088	$1.00\text{x}10^{-4}$
Thompson-Spaepen, $\sigma = constant$	$2.92\text{x}10^{33}$	57.70	1.28	0.104	
Thompson-Spaepen, $\sigma \propto T$	$4.40\text{x}10^{22}$	32.78	1.06	0.084	$9.54\text{x}10^{-5}$

[a] The approximation used for the driving free energy and assumption made about the dependence of σ on temperature.

[b] The value of σ, when assumed to be a constant, or calculated at T_u, the average supercooling temperature, when assumed to be linearly temperature dependent.

[c] The temperature coefficient (σ_0) for $\sigma = \sigma_o T$.

Finally, 210 measurements were obtained from three samples, ranging in mass from 54.79mg to 65.38mg, with the slight difference in sample volume normalized out. The average observed supercooling was 233°C (18.6% supercooling), representing both the lowest magnitude of supercooling and lowest supercooling percentage. The best fit parameters calculated at the average supercooling are listed in Table 5.7. The distribution of supercoolings for $Cu_{64}Zr_{36}$ are more sharply peaked than the others. Interestingly, $Cu_{64}Zr_{36}$ required the most conditioning before reproducible supercooling measurements could be performed; however, once the sample was conditioned, the supercooling varied little from the average, as seen in the sharper peak. While the percentage supercooling measured here is slightly smaller than reported elsewhere, the interfacial free energy is still in agreement with other published data [31].

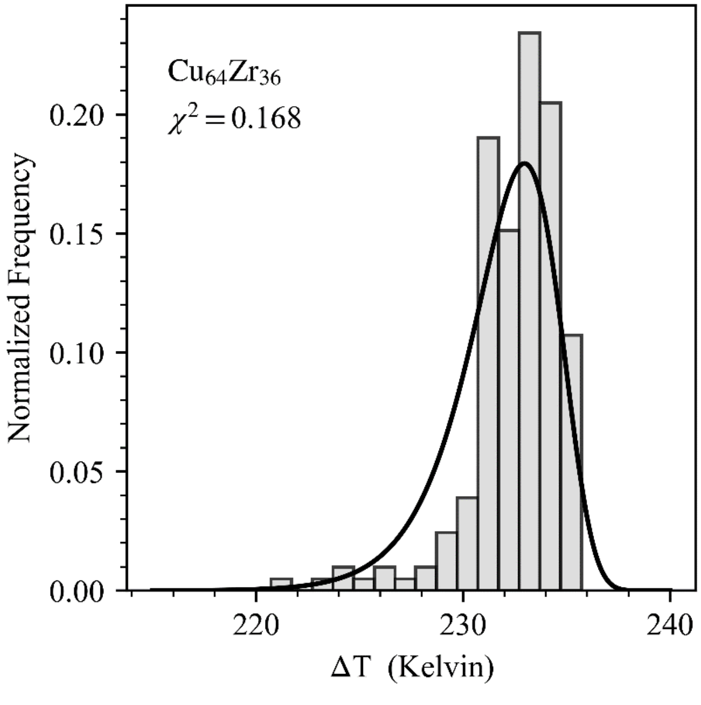

Figure 5.8: The histogram of maximum supercooling measurements for $Cu_{64}Zr_{36}$. The average supercooling was 233°C (18.6%). The curve is the fitted probability density with a p-value > 0.999, indicating a good fit.

TABLE 5.7. Calculated nucleation parameters for $Cu_{64}Zr_{36}$ at the average supercooling for different approximations of ΔG and the assumed temperature dependence of σ.

Approximation [a]	A^* $(m^3s)^{-1}$	W^*/k_BT	r^* (nm)	σ (J/m^2) [b]	σ_0 (J/m^2K) [c]
Turnbull, $\sigma = constant$	$1.98\text{x}10^{37}$	65.47	1.30	0.130	
Turnbull, $\sigma \propto T$	$1.75\text{x}10^{29}$	46.94	1.17	0.116	$1.14\text{x}10^{-4}$
Thompson-Spaepen, $\sigma = constant$	$4.64\text{x}10^{41}$	75.54	1.42	0.126	
Thompson-Spaepen, $\sigma \propto T$	$2.49\text{x}10^{31}$	51.89	1.25	0.112	$1.10\text{x}10^{-4}$

[a] The approximation used for the driving free energy and assumption made about the dependence of σ on temperature.

[b] The value of σ, when assumed to be a constant, or calculated at T_u, the average supercooling temperature, when assumed to be linearly temperature dependent.

[c] The temperature coefficient (σ_0) for $\sigma = \sigma_o T$.

Just like for Zr-Pd, the DIT was used to fit the probability density to the histogram of supercoolings for Cu-Zr. The histograms are not reproduced here, as the overall shape did not change. The best fit values calculated at the respective average supercooling temperatures and the corresponding driving free energy approximation are listed in Table 5.8.

TABLE 5.8. Calculated nucleation parameters for Cu-Zr family using the Diffuse Interface Theory

Sample	Approximation [a]	A^* $(m^3s)^{-1}$	W^*/k_BT	r^* (nm)	δ (Å) [b]
$Cu_{50}Zr_{50}$	Turnbull	$5.57\text{x}10^{25}$	39.85	1.15	1.65
$Cu_{50}Zr_{50}$	Thompson-Spaepen	$3.64\text{x}10^{32}$	55.54	1.34	1.61
$Cu_{55}Zr_{45}$	Turnbull	$3.06\text{x}10^{23}$	34.72	1.11	1.47
$Cu_{55}Zr_{45}$	Thompson-Spaepen	$2.89\text{x}10^{28}$	46.18	1.27	1.43
$Cu_{64}Zr_{36}$	Turnbull	$4.88\text{x}10^{32}$	54.87	1.29	1.26
$Cu_{64}Zr_{36}$	Thompson-Spaepen	$1.39\text{x}10^{37}$	65.13	1.41	1.23

[a] The approximation used for the driving free energy.

[b] The value of δ calculated at the maximum supercooling temperature T_u.

5.5 Discussion

The general magnitude in σ appears to be consistent with previous studies [28,32,33], with a temperature independent σ typically 0.1 J/m^2 to 0.2 J/m^2 and a linearly-temperature dependent coefficient σ_0 from 8x10^{-5} J/m^{2}K to 1.1x10^{-4} J/m^{2}K. Similar to previous studies, W^* and σ appear relatively insensitive to the approximation of the driving free energy. Large differences are still observed in the values of A^* between alloys both within the same binary family and out to other compositions. However, the values for σ calculated for the Cu-Zr family appear to agree with other published data [31].

As outlined elsewhere [34], the difference in r^* between the CNT and DIT is of order $\delta/2$. The difference in the calculated values of r^* between CNT and DIT here are smaller (approximately 0.1 Å) than $\delta/2$, which is between 0.6 to 0.8 Å. However, they are of the same order-of-magnitude. The relative difference between the prediction and experimental data may be due to a first-order expansion used to arrive at the relatively simple $\delta/2$ term.

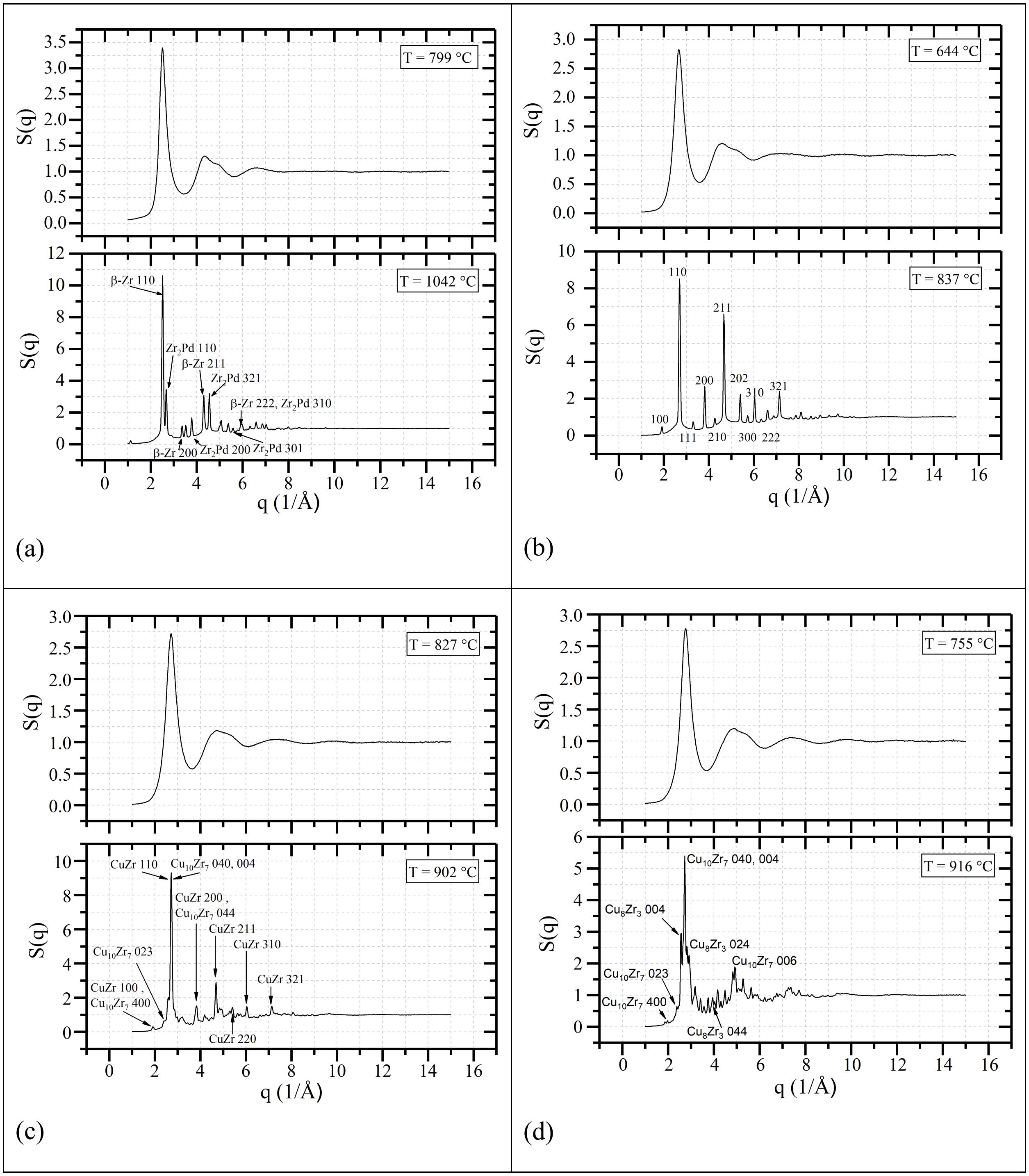

Figure 5.9: The collection of static structure factors *S(q)* for (a) $Zr_{75.5}Pd_{24.5}$, (b) $Cu_{50}Zr_{50}$, (c) $Cu_{55}Zr_{45}$, and (d) $Cu_{64}Zr_{36}$. The top plot of *S(q)* for each composition represents the liquid immediately before crystallization at the indicated maximum supercooling temperature, while the plot below represents the crystal phase formed shortly after. The Miller indices characteristic of the crystal structure of that phase are indicated. For (c) and (d), the lattice parameters are quite large, resulting in lower-order Miller Index peaks (i.e. 110, 200, etc.) that are below the lowest resolution in *q*.

In the Zr-Pd family, a steady increase in σ is observed from $Zr_{75.5}Pd_{24.5}$ to $Zr_{50}Pd_{50}$. Studies of zirconium-noble metal binary alloys [35] and $Zr_{75.5}Pd_{24.5}$ [36] have shown that medium range order is established in these supercooled liquids and that, for $Zr_{75.5}Pd_{24.5}$, there is a general increase in "icosahedral-like" clusters with supercooling temperature. The *S(q)* for $Zr_{75.5}Pd_{24.5}$ is shown in Fig. 5.9 (a), obtained from X-ray scattering measurements made at the Advanced Photon Source (APS) at Argonne National Laboratory (ANL). As reported by Waterstrat and Okamoto [8–10], the crystal structure for $Zr_{75.5}Pd_{24.5}$ is a phase mixture of bcc β-Zr and tetragonal $PdZr_2$. The Miller indices corresponding to this phase mixture are labeled on the *S(q)*. The crystal structures for (i) (i) $Zr_{50}Pd_{50}$ and (ii) $Pd_{55}Zr_{45}$ are reported to be (i) a cubic B2 structure with tendencies to develop martensite orthorhombic features upon cooling and (ii) a distorted and stressed A-B alternating B2 type structure [8]. With the propensity of this alloy family to develop significant medium-range order in the supercooled liquid, the increase in σ may indicate an increasing nucleation barrier, consistent with Frank's hypothesis [37]. Especially in the cases of $Zr_{50}Pd_{50}$ and $Pd_{55}Zr_{45}$, a significant rearrangement and breaking of this medium-range order must occur to form the cubic lattice.

The smallest σ and A^* for the Zr-Pd family is observed in $Zr_{75.5}Pd_{24.5}$, which may indicate it has a smaller nucleation barrier. Studies on $PdZr_2$ performed by Herlach *et. al.* in ESL and EML were reportedly limited by heterogeneous nucleation [38], as the maximum supercooling could not be achieved. The $PdZr_2$ studied by Herlach *et. al.* is not the same composition as $Zr_{75.5}Pd_{24.5}$; however, $PdZr_2$ forms part of the solid phase mixture observed in $Zr_{75.5}Pd_{24.5}$. It is possible that $Zr_{75.5}Pd_{24.5}$'s tendency of solute-solute avoidance [36] may lead to the clustering of zirconium and facilitation of the crystallization of the β-Zr phase. While $PdZr_2$ is tetragonal, it can be regarded as a stretched bcc phase. β-Zr, which is also bcc ordered, could act like a heterogeneous nucleation site that could catalyze formation of the $PdZr_2$ phase. X-ray observations of crystallization suggest that either both phases form at the same time or form separately on a timescale faster than 0.5 seconds. As indicated from the supercooling data for $Zr_{75.5}Pd_{24.5}$ in Fig. 5.9, a consistent maximum supercooling temperature was achieved, suggesting heterogeneous nucleation was likely not present. Turnbull noted that, in the case of heterogeneous nucleation, the magnitude of A^* should be smaller [39]. However, other metallic systems, such as $Ti_{39.5}Zr_{39.5}Ni_{21}$ [28], have shown both reproducible maximum supercooling and smaller values of A^*. It should be noted that Herlach *et. al.* report a value of A^* of approximately 10^{16} $(m^3s)^{-1}$, clearly suggesting a heterogeneous nucleation mechanism. The A^* presented here for $Zr_{75.5}Pd_{24.5}$ is ten orders of magnitude larger. Future studies could attempt to reproduce these results using higher purity Pd bar stock to further minimize the possibility of heterogeneous nucleation.

For the Cu-Zr family, the values of σ are much closer to each other and are smaller than those found in the Zr-Pd family. As reported by Holland-Moritz *et. al.* from X-ray and neutron scattering experiments, the Cu-Zr supercooled liquids are not dominated by short and medium range icosahedral order [40]. Instead, the local order in Cu-Zr liquids is likely a combination of multiple motifs and higher order structures. While this may appear in contradiction with [31], which reports significant icosahedral order in $Cu_{64}Zr_{36}$ metallic glass, it should be noted that the two studies examined different cases for Cu-Zr, with the former studying electrostatically levitated supercooled liquids and the latter studying a quenched $Cu_{64}Zr_{36}$ metallic glass at ambient temperatures. The lack of icosahedral order in the supercooled liquid could mean less competing structure must be broken to form the crystal, which could lower the nucleation barrier and the value of σ. The calculated values of σ are also in agreement with [31].

The crystal structures of the Cu-Zr alloys studied here are (i) primitive cubic for $Cu_{50}Zr_{50}$, (ii) a phase mixture of primitive cubic and orthorhombic $Cu_{10}Zr_7$ for $Cu_{55}Zr_{45}$, and (iii) a phase mixture of orthorhombic Cu_8Zr_3 and $Cu_{10}Zr_7$ for $Cu_{64}Zr_{36}$ [6,7]. Like for Zr-Pd, the corresponding liquid and crystal X-ray *S(q)*'s obtained from the APS are produced in Fig. 5.9, with the predicted Miller indices indicated. For $Cu_{50}Zr_{50}$, the predicted Bragg scattering from a primitive cubic structure trivially maps onto the *S(q)*, while the more complicated orthorhombic $Cu_{10}Zr_7$ (C2ca space group) [27] and orthorhombic Cu_8Zr_3 (Pnma space group) [27] structures show more peaks and oscillations in the crystal *S(q)*. In each case, lattice parameters from [7] were used to calculate the predicted scattering peak locations.

The largest σ corresponds to $Cu_{64}Zr_{36}$, which would suggest the phase mixture of two orthorhombic structures was more difficult to nucleate. It is also the most sharply peaked supercooling distribution presented here, suggesting that the supercooling limit may have been reached. The higher supercooling percentage reported elsewhere [31] may be due to discrepancies in the value of T_l used in the calculation of the maximum supercooling temperature.

The DIT can provide more insight into the relative order between the liquid and crystal phases. For example, $Ti_{39.5}Zr_{39.5}Ni_{21}$ has a small value for δ (0.76 Å) since the liquid and crystal share similar order [28], while Gránásy [4] found the value of δ for supercooled mercury to be 2.12 Å. In the case of mercury, the liquid and crystal are structurally different [41], possibly due to the presence of icosahedral clusters in the liquid [19,37]. In contrast to the trends observed with σ from CNT, the Cu-Zr alloys have larger magnitudes of δ compared to those from Zr-Pd. δ gives information about the difference between entropy and enthalpy surfaces. From a statistical mechanics argument, the highest entropy configuration of a system occurs with maximum disorder. Based on the results from Holland-Moritz [40], a lack of short and medium range icosahedral order in Cu-Zr supercooled liquids, implying a higher entropy configuration, could explain the systematically larger δ, compared to the smaller δ found in more ordered Zr-Pd supercooled liquids. Molecular dynamics studies of Cu-Zr in the same temperature region appear to reinforce these ideas [42,43].

The calculated values of δ also appear to depend on the number of phases formed. In both alloy families studied, the single-phase forming intermetallic compositions have the largest δ for their respective families, followed by the eutectic and the off-intermetallic compositions. The intermetallic compositions studied here nucleate to γPdZr in the case of $Zr_{50}Pd_{50}$ [9] or cubic Cu-Zr for $Cu_{50}Zr_{50}$ [6]. Both of these cubic phases would require a significant rearrangement of the liquid into a single crystal lattice. Meanwhile, the eutectic compositions, which have middle-range values of δ, and off-intermetallic compositions, which have the smallest values of δ, generally nucleate two-phase mixtures. For these alloys, the splitting of the main peak in the crystal $S(q)$ is observable in section (a), (c), and (d) of Fig. 5.9. In these cases, the first peak in the liquid $S(q)$ appears to contain multiple characteristic Miller indices of both crystal phases. This could explain the smaller δ, as the primary order in the liquid could more closely mirror the complex structural motifs found in multiple phase forming alloys. Through a simple comparison between the $S(q)$ from $Cu_{50}Zr_{50}$ to the $S(q)$ of $Cu_{64}Zr_{36}$, it appears as though multiple phase formation—especially with lower symmetry orthorhombic crystal phases—leads to a relatively more disordered crystal. Again, this likely decreases the difference between entropy and enthalpy surfaces when compared to a system that forms a higher symmetry, more-ordered crystal.

5.6 Conclusion

A study of over 1,500 supercooling measurements from $Zr_{50}Pd_{50}$, $Pd_{55}Zr_{45}$, $Zr_{75.5}Pd_{24.5}$, $Cu_{50}Zr_{50}$, $Cu_{55}Zr_{45}$, and $Cu_{64}Zr_{36}$ was performed and the nucleation parameters were calculated using the Classical Theory and Diffuse Interface Theory with the Skripov Method. Comparing the nucleation parameters within the Zr-Pd and Cu-Zr alloy families using the CNT suggests that $Zr_{50}Pd_{50}$ and $Cu_{64}Zr_{36}$ have the largest nucleation barriers, while the eutectics $Zr_{75.5}Pd_{24.5}$ and $Cu_{55}Zr_{45}$ have the smallest nucleation barriers. This appears to contradict results from the DIT, whereby the intermetallics show the largest δ and the off-intermetallics show the smallest δ. However, a pattern appears to have emerged on the impact of multiple phase formation in the nucleation of crystals from the supercooled liquid. Further broad studies of alloys from the same family are required to more fully understand these results. It may be the combination of structural differences, number of phases formed, crystal composition, number of alloy components, and other kinetic and thermodynamic considerations are all required to arrive at a full picture describing the nucleation of these phases from the liquid.

5.7 References

1. Turnbull, D. & Fisher, J. C. Rate of nucleation in condensed systems. *J. Chem. Phys.* **17**, 71–73 (1949).
2. Spaepen, F. Homogeneous nucleation and the temperature dependence of the crystal-melt interfacial tension. in *Solid State Physics* (eds. Ehrenreich, H. & Turnbull, D.) **47**, 1–32 (Academic Press, 1994).

3. Gránásy, L. Diffuse interface theory of nucleation. *J. Non. Cryst. Solids* **162**, 301–303 (1993).

4. Gránásy, L. Nucleation theory for diffuse interfaces. *Mater. Sci. Eng. A* **178**, 121–124 (1994).

5. Wang, D. *et al.* Bulk metallic glass formation in the binary Cu-Zr system. *Appl. Phys. Lett.* **84**, 4029–4031 (2004).

6. Okamoto, H. Cu-Zr (Copper-Zirconium). *J. Phase Equilibria Diffus.* **33**, 417–418 (2012).

7. Arias, B. D. & Abrlata, J. P. Cu-Zr (Copper-Zirconium). *J. Phase Equilibria* **11**, 452–459 (1990).

8. Waterstrat, R. M., Shapiro, A. & Jeremie, A. The palladium-zirconium phase diagram. *J. Alloys Compd.* **290**, 63–70 (1999).

9. Okamoto, H. Pd-Zr (palladium-zirconium). *J. phase equilibria Diffus.* **30**, 413–414 (2009).

10. Okamoto, H. Pd-Zr (Palladium-Zirconium). *J. Phase Equilibria* **23**, (2002).

11. Gangopadhyay, A. K. *et al.* Beamline electrostatic levitator for in situ high energy x-ray diffraction studies of levitated solids and liquids. *Rev. Sci. Instrum.* **76**, 073901 (2005).

12. Mauro, N. A. & Kelton, K. F. A highly modular beamline electrostatic levitation facility, optimized for in situ high-energy x-ray scattering studies of equilibrium and supercooled liquids. *Rev. Sci. Instrum.* **82**, 035114 (2011).

13. Chung, S. K., Thiessen, D. B. & Rhim, W. K. A noncontact measurement technique for

the density and thermal expansion coefficient of solid and liquid materials. *Rev. Sci. Instrum.* **67**, 3175–3181 (1996).

14. Lamb, H. On the Oscillations of a Viscous Spheroid. *Proc. London Math. Soc.* **s1-13**, 51–70 (1881).

15. Bendert, J. C. & Kelton, K. F. Containerless measurements of density and viscosity for a Cu48Zr52 liquid. *Int. J. Thermophys.* **35**, 1677–1686 (2014).

16. Bendert, J. C., Pueblo, C. E., Veligati, S., Mauro, N. A. & Kelton, K. F. Temperature calibration for optical pyrometry in containerless systems using differential scanning calorimetry: Application to Cu100−xZrx(x = 45–50). *Int. J. Thermophys.* **35**, 1687–1696 (2014).

17. Ge, L. *et al.* Prediction of the glass forming ability in Cu-Zr binary and Cu-Zr-Ti ternary alloys. *Intermetallics* **16**, 27–33 (2008).

18. Skripov, V. P. Homogeneous Nucleation in Melts and Amorphous Films. *Curr. Top. Mater. Sci.* **2**, 328–378 (1977).

19. Turnbull, D. Kinetics of Solidification of Supercooled Liquid Mercury Droplets. *J. Chem. Phys.* **20**, 411–424 (1952).

20. Thompson, C. V & Spaepen, F. On the Approximation of the Free Energy Change on Crystallization. *Acta Metall.* **27**, 1855 (1979).

21. Baser, T. A. & Baricco, M. Glass forming ability of (Cu50Zr50)96 M4 (M=none Al, Nb) bulk metallic glasses. *Rev. Adv. Mater. Sci.* **18**, 71–76 (2008).

22. Suo, Z. Y. *et al.* A new parameter to evaluate the glass-forming ability of bulk metallic glasses. *Mater. Sci. Eng. A* **528**, 429–433 (2010).

23. Kubaschewski, O. & Alcock, C. B. *Metallurgical Thermochemistry*. (Pergamon Press, 1979).

24. Blodgett, M. E., Egami, T., Nussinov, Z. & Kelton, K. F. Proposal for universality in the viscosity of metallic liquids. *Sci. Rep.* **5**, 1–8 (2015).

25. Ashcraft, R. A. Linking Structure and Dynamics in Metallic Liquids: A Combined Experimental and Molecular Dynamics Approach. (Washington University in St. Louis, 2018).

26. Villars, P., Calvert, L. D. & Pearson, W. B. Pearson's Handbook of Crystallographic Data for Intermetallic Phases. Volumes 1, 2, 3. *Am. Soc. Met. 1985,* 3258 (1985).

27. Cockcroft, J. A hypertext book of crystallographic space group diagrams and tables. (1999).

28. Sellers, M. E., Van Hoesen, D. C., Gangopadhyay, A. K. & Kelton, K. F. Maximum supercooling studies in $Ti_{39.5}Zr_{39.5}Ni_{21}$, $Ti_{40}Zr_{30}Ni_{30}$, and $Zr_{80}Pt_{20}$ liquids—Connecting liquid structure and the nucleation barrier. *J. Chem. Phys.* **150**, 204510 (2019).

29. Klein, S., Holland-Moritz, D. & Herlach, D. M. Crystal nucleation in undercooled liquid zirconium. *Phys. Rev. B* **80**, 2–5 (2009).

30. Morton, C. W., Hofmeister, W. H., Bayuzick, R. J., Rulison, A. J. & Watkins, J. L. The kinetics of solid nucleation in zirconium. *Acta Mater.* **46**, 6033–6039 (1998).

31. Kang, D. H. *et al.* Interfacial free energy controlling glass-forming ability of Cu-Zr alloys. *Sci. Rep.* **4**, 1–5 (2014).

32. Kelton, K. F. Crystal Nucleation in Liquids and Glasses. *Solid State Phys. - Adv. Res. Appl.* **45**, 75–177 (1991).

33. Kobold, R., Kolbe, M., Hornfeck, W. & Herlach, D. M. Nucleation study for an undercooled melt of intermetallic NiZr. *J. Chem. Phys.* **148**, 114502 (2018).

34. Kelton, K. & Greer, A. L. *Nucleation in condensed matter: applications in materials and biology*. **15**, (Elsevier, 2010).

35. Mauro, N. A. & Kelton, K. F. Medium range order in Zr-noble metal eutectic liquids. *J. Non. Cryst. Solids* **358**, 3057–3059 (2012).

36. Mauro, N. *et al.* Local atomic structure in equilibrium and supercooled liquid Zr75.5 Pd 24.5. *J. Chem. Phys.* **137**, (2012).

37. Frank, F. C. Supercooling of Liquids. *Proc. R. Soc. London.* **215**, 43–46 (1952).

38. Herlach, D. M., Kobold, R. & Klein, S. Crystal Nucleation and Growth in Undercooled Melts of Pure Zr, Binary Zr-Based and Ternary Zr-Ni-Cu Glass-Forming Alloys. *J. Miner. Met. Mater. Soc.* **70**, 726–732 (2018).

39. Turnbull, D. Formation of crystal nuclei in liquid metals. *J. Appl. Phys.* **21**, 1022–1028 (1950).

40. Holland-Moritz, D. *et al.* Does an icosahedral short-range order prevail in glass-forming Zr-Cu melts? *Epl* **100**, (2012).

41. Bosio, L., Cortes, R. & Segaud, C. X-ray diffraction study of liquid mercury over temperature range 173 to 473 K. *J. Chem. Phys.* **71**, 3595–3600 (1979).

42. Hao, S. G., Wang, C. Z., Kramer, M. J. & Ho, K. M. Microscopic origin of slow dynamics at the good glass forming composition range in Zr1-x Cux metallic liquids. *J. Appl. Phys.* **107**, 1–7 (2010).

43. Soklaski, R., Nussinov, Z., Markow, Z., Kelton, K. F. & Yang, L. Connectivity of icosahedral network and a dramatically growing static length scale in Cu-Zr binary metallic glasses. *Phys. Rev. B - Condens. Matter Mater. Phys.* **87**, 1–8 (2013).

Chapter 6: Summary and Future Work

This dissertation was primarily focused on studies of nucleation, either through a statistical analysis of hundreds of maximum supercooling measurements or by studying a few nucleation measurements made under different stirring conditions. Throughout this dissertation, several nucleation theories were used to analyze and interpret results, including the Classical Nucleation Theory (CNT), Diffuse Interface Theory (DIT), and Coupled-Flux Theory. The Skripov probability density was used in conjunction with the CNT and DIT to fit distributions of supercooling measurements to extract the relevant nucleation parameters A^*, W^*, σ, and δ.

Chapter 3 analyzed data from $Cu_{50}Zr_{50}$ and Vit106 liquids acquired in the microgravity environment of the International Space Station to explore the Coupled-Flux theory's predictions regarding the role of stirring and diffusion on nucleation. Initial results from calculations using the CNT and DIT and computational fluid dynamics calculations suggest that highly stirred liquids are likely not diffusion-limited; thus, the CNT and DIT likely describe the nucleation kinetics. Meanwhile, the quiescent liquids studied in microgravity may have nucleation processes limited by diffusion, as they were shown to have smaller values of A^* than the highly stirred cycles and smaller shear-rates from stirring calculations, in agreement with predictions from the Coupled-Flux theory. This study served as a first pass at probing the nucleation data from the ISS and to begin applying the Coupled-Flux theory to experiments.

Chapter 4, which was slightly modified from a publication in the Journal of Chemical Physics, explored the role of local structure on the nucleation barrier in $Ti_{39.5}Zr_{39.5}Ni_{21}$, $Ti_{40}Zr_{30}Ni_{30}$, and $Zr_{80}Pt_{20}$. Over 1000 supercooling measurements were gathered using the

Electrostatic Levitation processing techniques, with 686 from $Ti_{39.5}Zr_{39.5}Ni_{21}$, 191 from $Ti_{40}Zr_{30}Ni_{30}$, and 274 from $Zr_{80}Pt_{20}$. Using the Skripov method, the data were analyzed using the CNT and DIT to understand the potential impact of local order on the nucleation barrier. Results from $Ti_{39.5}Zr_{39.5}Ni_{21}$ suggest that comparable local icosahedral order in the supercooled liquid reduces the nucleation barrier for the icosahedral quasicrystal. Meanwhile, conflicting liquid and crystal order in the case of $Ti_{40}Zr_{30}Ni_{30}$ and $Zr_{80}Pt_{20}$ likely increase the nucleation barrier. This can be seen in σ from the CNT and δ from the DIT. The data from $Ti_{39.5}Zr_{39.5}Ni_{21}$ yielded the smallest values for these two parameters, suggesting a small nucleation barrier and a small entropy difference between the liquid and quasicrystal phase, while the values for σ and δ from $Zr_{80}Pt_{20}$ are at least a factor of two larger, suggesting a large nucleation barrier and significant differences in the structures and entropy.

Chapter 5 was an extension of the studies performed in Chapter 4 to further explore the role of local order and number of phases formed on nucleation. The Cu-Zr and Zr-Pd binary alloy families were picked because these alloys are of interest in upcoming ISS experiments and because of their relevance for metallic glass formation. Three alloys from each family were studied ($Zr_{50}Pd_{50}$, $Pd_{55}Zr_{45}$, $Zr_{75.5}Pd_{24.5}$, $Cu_{50}Zr_{50}$, $Cu_{55}Zr_{45}$, and $Cu_{64}Zr_{36}$) by performing over 200 maximum supercooling measurements for each, giving a total over 1,600 measurements. The data were analyzed with the Skripov method, using both CNT and DIT. X-ray scattering measurements for both the liquid and crystal phases were analyzed to explore any similarities in their structures. The findings from this study further imply that the order between the liquid and crystal phase has an impact on the nucleation barrier, with the results from DIT suggesting that highly complex crystal structures are entropically more like the liquid than simple crystal structures. Furthermore, the number of phases formed appears to have some relation to the nucleation barrier as well, where intermetallic alloys forming one phase typically gave the larger nucleation parameters of the family.

Future studies should continue to explore maximum supercooling measurements in several different liquid alloys, such as Zr-Ni, Zr-Rh, Cu-Zr-Al, Vit106/106a, Cu-Zr-Ti-Al, and others to both support continuing experiments on the International Space Station and answer questions about the impact of multiple phase formation, local order, and number of components on nucleation. Future ISS studies should also continue experiments outlined in Chapter 3, where the heater and positioner settings of the EML are systematically varied to extract information related to the impact of stirring on nucleation. Continued collaboration with the Bob Hyers group at the University of Massachusetts, Amherst will improve the understanding of stirring on nucleation and could provide information to implement simulations and modeling of nucleation from the coupled flux theory. Other smaller computational projects could explore the impact of a non-constant cooling rate on the Skripov analysis of supercooling measurements or apply other nucleation theories to the Skripov method as demonstrated in earlier chapters.

Appendix A: ESL Operating Procedure

This appendix covers routine ESL operation and documents some of the more common fixes required to keep the ESL operational.

Initial Setup (Cleaning, Loading, and Running Programs)

a) If there is significant deposition on the top and bottom electrodes, clean them with sandpaper, acetone, and methanol, then blow dry with compressed air to remove particles. If you must remove the top and bottom electrode, turn on the ESL computers and open the Capture OEM for the visualization camera (PC1) and ESL program (PC2), (see later in appendix). Mark the position of the bottom electrode on the monitor with a sticky note so you know how much to screw it in. The top electrode should be able to fit two glass slides between it and the top macor block. Make sure that all glass slides in front of the optical windows are clean (no visible gray deposition) and electrical connections to the electrodes are firmly attached.

b) Screw in the bottom electrode. The top of the bottom electrode should be just a tad below the top of the side electrodes. Reference figures later in the manual for approximate bottom electrode position (Fig. A.5).

c) Load the carousel with samples. The carousel should contain a WC standard after every two samples. On the other end, some Al and WC samples should be loaded, in case the ESL optics need to be realigned. All sample masses and positions must be recorded in the carousel spreadsheet.

d) If using the stainless-steel carousel, the “zero” position is located at 18. Thus, your samples should start at position 19. The back Al and WC samples should start at position 17.

e) The two pins that engage with the carousel need to be in elevated positions. Otherwise, the carousel cannot be engaged to the drive mechanism. Place the carousel in position and tighten the set screw. Make sure that the anchoring screw is removed before closing the chamber. There is a drilled and tapped hole for the anchoring screw directly below the carousel mechanism. If the anchoring screw is not removed, the carousel cannot be operated.

f) If using the stainless-steel carousel, do not screw in the set screw all the way. Before placing the carousel onto the mechanism, rotate the set screw until it is flush with the interior bore. Place the carousel onto the drive mechanism; the set screw should be facing you. Insert the hex key into the set screw and keep track of your starting position. Rotate the hex key 1.5 revolutions to engage the carousel with the drive mechanism. Before removing the anchoring screw, gently lift the carousel up to test if is engaged with the mechanism. Overtightening the carousel will cause the upper plate to lift up and samples to spill out.

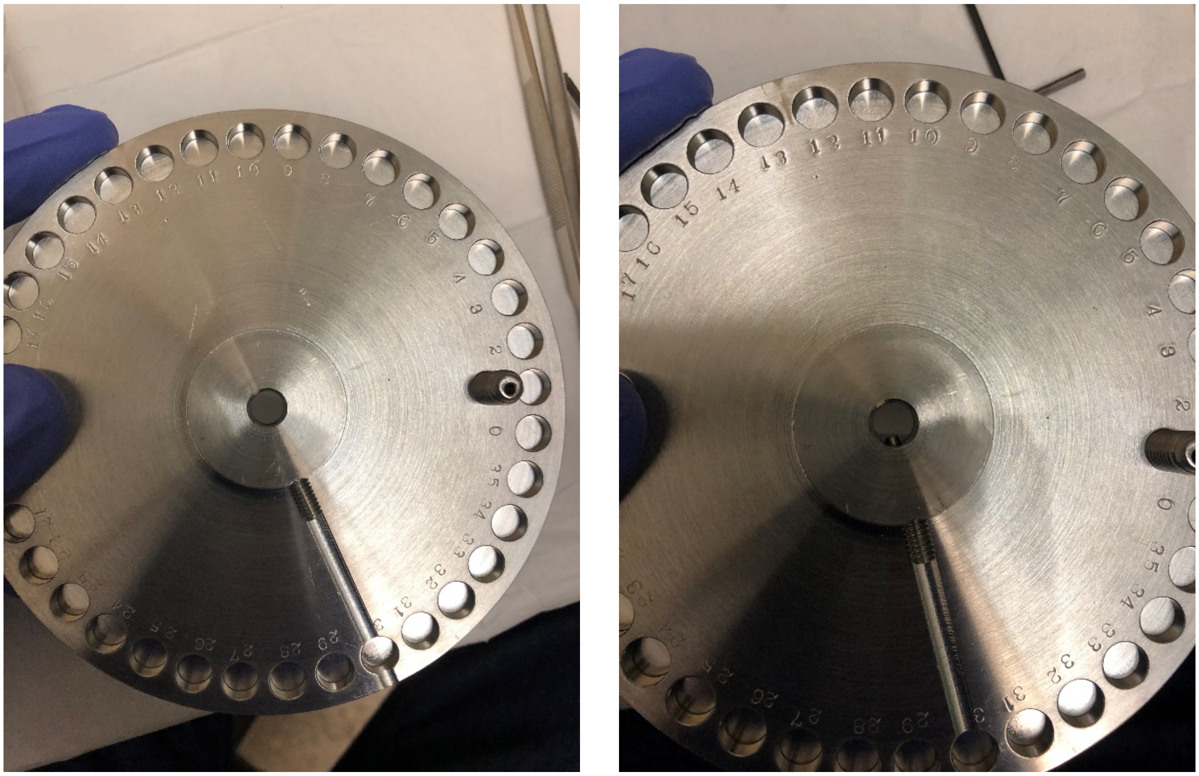

Figure A.1: The stainless-steel carousel. (Left) the set screw is flush with the wall of the interior bore. (Right) After 1.5 turns, the set screw should engage with the carousel mechanism. Do not overtighten.

g) Make sure that the copper spacer is sitting in the right position on the vacuum flange. It should be just inside the knife edge. Check the O-ring around the spacer for dirt and lubrication. Clean with methanol as needed and reapply a thin layer of silicone vacuum grease. The channel for the O-ring, copper spacer, and upper knife edge should be gently cleaned with acetone and methanol as needed. The O-ring should rest in the channel between the copper gasket and the wall of the flange.

h) Close the ESL chamber. Turn on both scroll pumps. Open the gate valve to the chamber slowly. Open the valves that connect to the UV lamp. They are at the back of the instrument. One valve is a rotary, hand-tightened one, located to the left when facing the instrument from the back side. The other is a hand-tightened screw that is on the right side, while facing the instrument from the rear side. The final one is a Swagelok-branded valve that supplies helium to the UV, located to the left of the UV. Turn on the main turbo pump (Osaka) after the chamber pressure goes below 100 mTorr. Turn on the small turbo pump (Pfeiffer) with the Osaka turbo.

i) Depending on the exposure time to the ambient, it will take 1-3 days to bring the vacuum to 10^{-8} Torr. The ESL can be operated at higher pressures (not exceeding 5×10^{-6}); however, due to higher oxygen concentrations, samples will likely become contaminated more quickly.

j) Turn on PC1 (viscosity computer) and PC2 (ESL computer), if not already on.

k) Turn on Target PC (on the rack), PSD readout box, green and blue LEDs, and the power amplifiers for x-, y-, and z-electrodes. **Do not switch the z-high voltage until you are ready to launch. This voltage must be off during sample transfer from the carousel to avoid arcing.**

l) Open the He-tank valves that feed the UV lamp. **Do not change the middle knob on the regulator**. Turn on the power supply that feeds the UV lamp. Set voltage to 800 V and current to 130 mA. Wait about 10 minutes so the helium has a chance to flow through the needle valve and into the ignition chamber. Attempting to ignite the UV immediately after opening the helium tank valves will result in the UV shutting itself off from lack of helium. After approximately 10 minutes, ignite the UV. The voltage should start around 700-750 and then gradually come down near 600 V. The pressure indicated on the UV control panel must be maintained at around 1.1×10^{-1} mbar. This pressure may be adjusted by turning the needle valve located directly above the helium tank. Ensure the pressure stays around this level. Otherwise, adjust the regulator and needle valve until a constant pressure is achieved.

m) Open Matlab 2011b on PC2. Connect to the Target PC by typing and running “xpcexplr” from the front console. The TargetPC interface will appear at left of the window. Right click on TargetPC1 and then click on connect to connect to the TargetPC. Download the program “WC_m1100_20180726” (or some other algorithm that is displayed at the top left) to the target PC by dragging it to PC1. Typing “ControlGUI” on the Matlab command line allows for new algorithms to be generated. However, this usually isn’t necessary since the algorithms are fairly robust. You can use the WC algorithm for almost all samples using the gain switching technique and setting the saturation z voltages to the appropriate levels.

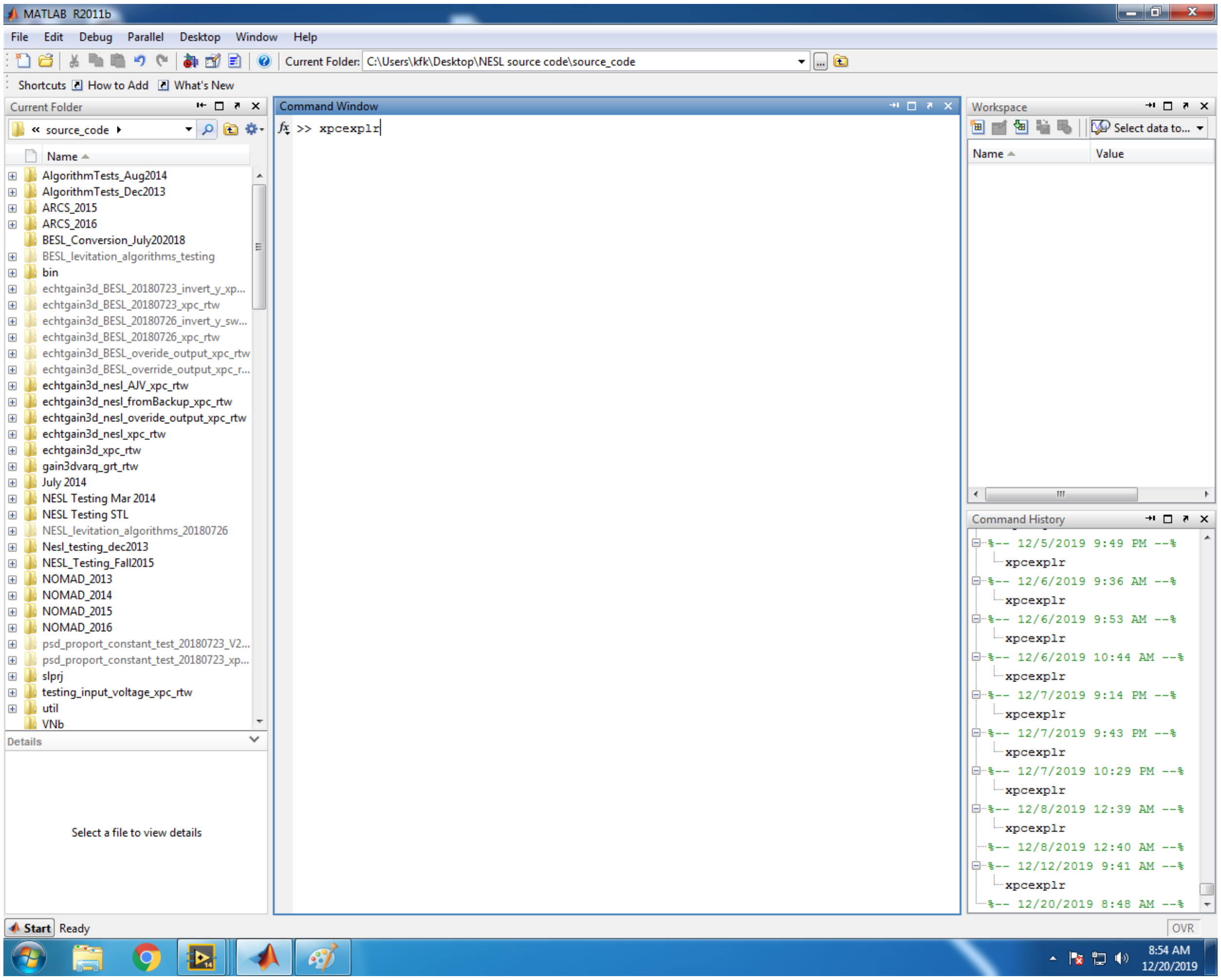

Current Folder: C:\Users\kfk\Desktop\NESL source code\source_code

```
>> xpcexplr
```

```
%-- 12/5/2019 9:49 PM --%
   xpcexplr
%-- 12/6/2019 9:36 AM --%
   xpcexplr
%-- 12/6/2019 9:53 AM --%
   xpcexplr
%-- 12/6/2019 10:44 AM --%
   xpcexplr
%-- 12/7/2019 9:14 PM --%
   xpcexplr
%-- 12/7/2019 9:43 PM --%
   xpcexplr
%-- 12/7/2019 10:29 PM --%
   xpcexplr
%-- 12/8/2019 12:39 AM --%
   xpcexplr
%-- 12/8/2019 12:40 AM --%
%-- 12/12/2019 9:41 AM --%
   xpcexplr
%-- 12/20/2019 8:48 AM --%
```

Figure A.2: Screenshot of the command prompt screen for MATLAB. Type in xpcexplr to open the TargetPC interface.

n) Click on “Model Hierarchy” to modify the necessary levitation parameters.

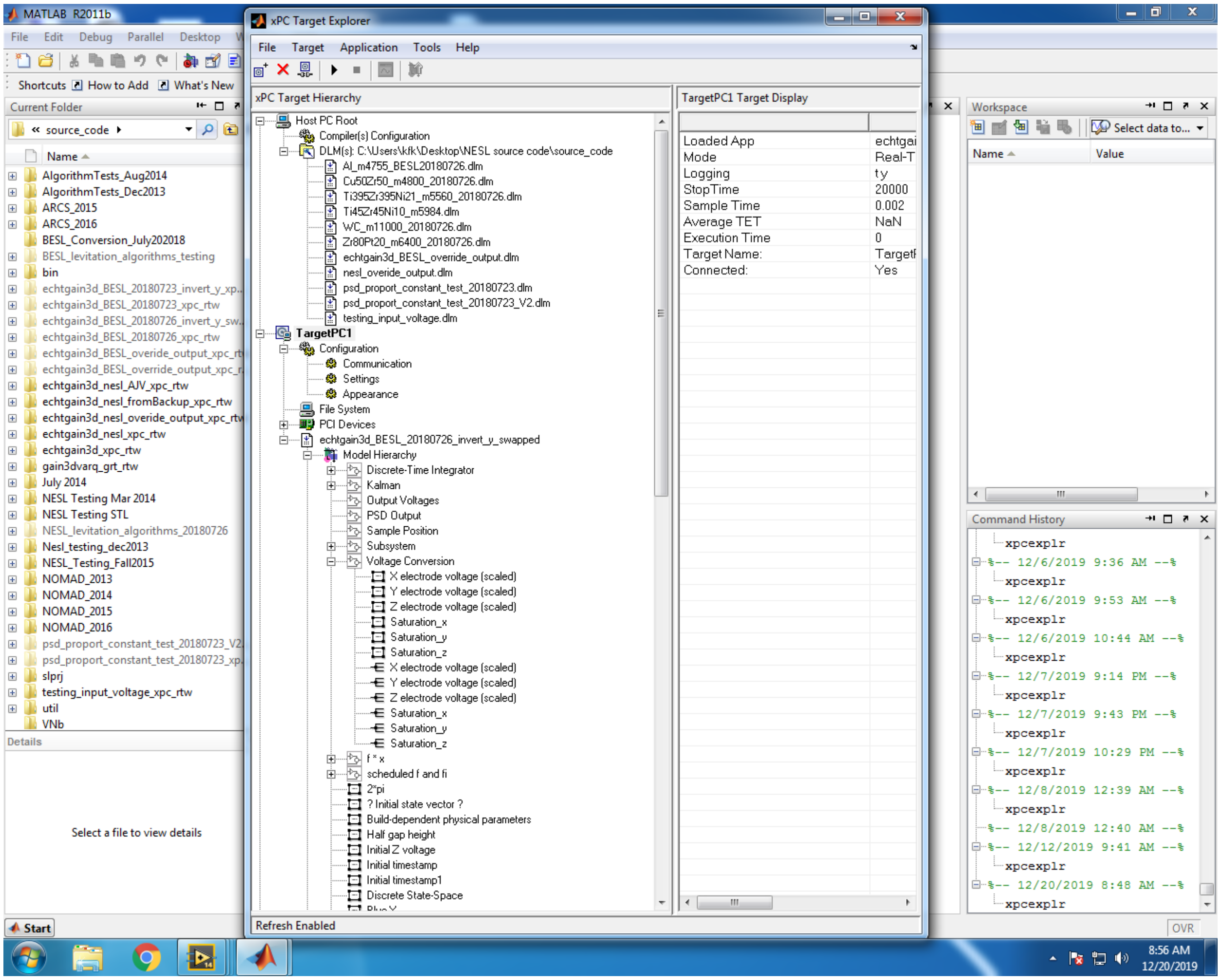

Loaded App	echtgai
Mode	Real-T
Logging	t y
StopTime	20000
Sample Time	0.002
Average TET	NaN
Execution Time	0
Target Name:	Target
Connected:	Yes

Figure A.3: The xPC Target Explorer GUI, after connecting to TargetPC1. Note that an algorithm has already been downloaded. If the TargetPC was recently turned on, a fresh algorithm will need to be downloaded.

a. Set initial launch gains by changing “Blue X” and “Green X” to -0.01 and “Green Y’ to -0.012. Be sure to click the “update parameter” button after changing each one. All three of these parameters will be reduced to -0.006 (see 15e)) after launching the sample as it gives better stability. The sign is important. Setting a positive value will result in sample instability.

b. Check that “x position” and “y position” are 0, and set “z position” to 0.0043. After launching, if the x, y, voltages appear large, these positions need to be adjusted to reduce x,y voltages to near zero so that the sample floats near the center (see step 15h) below). The z-position needs to be adjusted if the sample appears to be floating high/low in the visualization/density camera. If levitating Al samples, the z-pos may need to be reduced to as low as 0.0035-0.0038 (see step 15g)).

c. Click on “z-voltage saturation” setting. Change the “upper limit” to 0 and “lower limit” to between -13000 to -15000 to launch metallic alloys, -18000 for WC, and -10000 for Al.

d. If a sample needs to be kicked out after launch or after completion of the experiment, set the Saturation Z upper limit to match the sign and magnitude of Saturation Z lower limit. Upon updating the upper limit, the sample will fly away. After kicking the sample out, stop the algorithm.

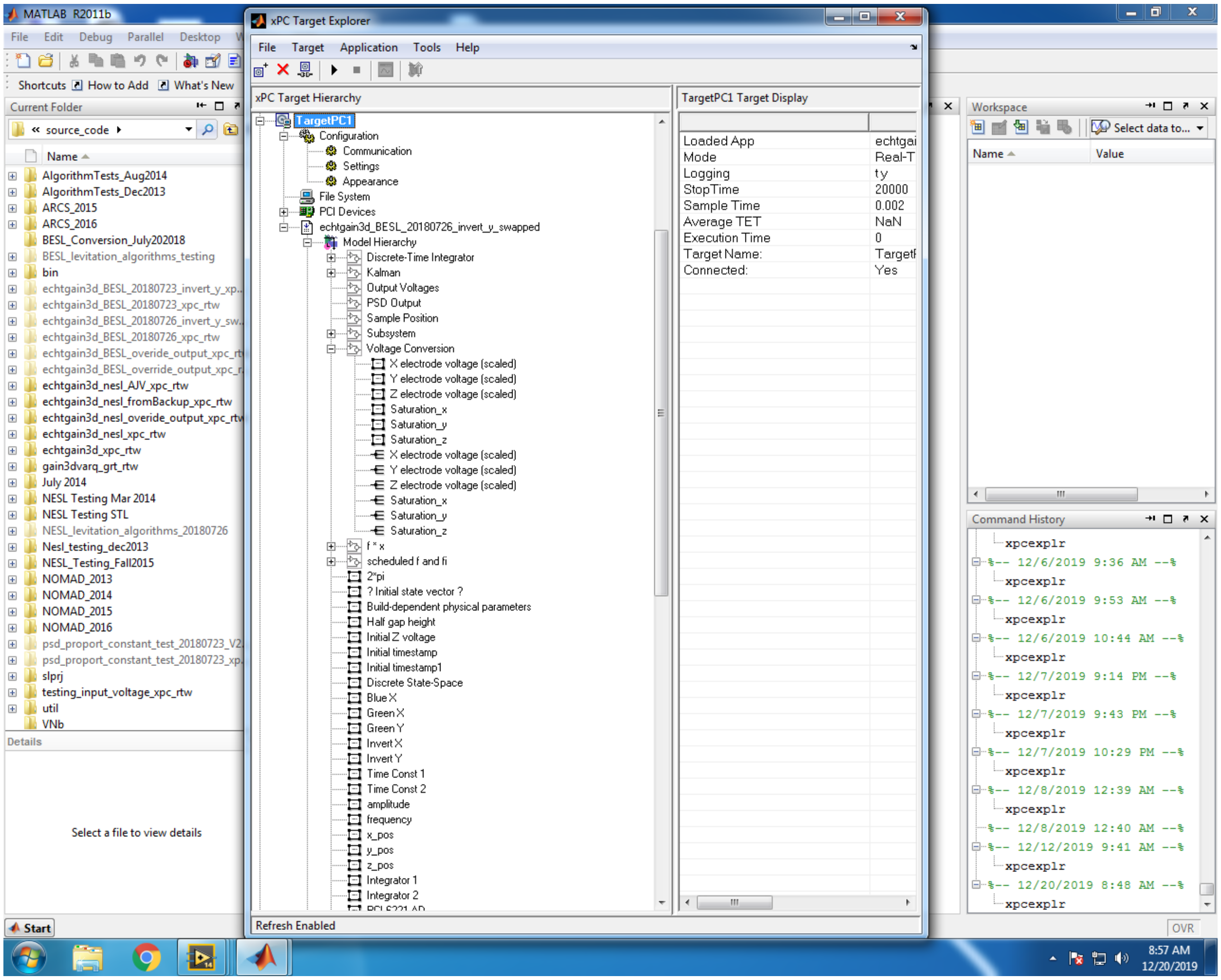

Loaded App	echtgai
Mode	Real-T
Logging	ty
StopTime	20000
Sample Time	0.002
Average TET	NaN
Execution Time	0
Target Name:	Target‹
Connected:	Yes

```
xpcexplr
%-- 12/6/2019 9:36 AM --%
xpcexplr
%-- 12/6/2019 9:53 AM --%
xpcexplr
%-- 12/6/2019 10:44 AM --%
xpcexplr
%-- 12/7/2019 9:14 PM --%
xpcexplr
%-- 12/7/2019 9:43 PM --%
xpcexplr
%-- 12/7/2019 10:29 PM --%
xpcexplr
%-- 12/8/2019 12:39 AM --%
xpcexplr
%-- 12/8/2019 12:40 AM --%
%-- 12/12/2019 9:41 AM --%
xpcexplr
%-- 12/20/2019 8:48 AM --%
xpcexplr
```

Figure A.4: All of the parameters available for change in the algorithm. Note that Saturations are located under “Voltage Conversion” and the gains and positions are located under “Model Hierarchy”.

o) The x, y voltage upper and lower saturation limit is set by default to +/- 3000. This does not need to be changed.

p) Open the LabVIEW ESL program, labeled as “ESL_20181204 shortcut” and located at the top left corner of the desktop. Start this program by clicking the arrow button at the top left corner. This window contains all necessary controls for sample heating and measurements. The image of the bottom electrodes will appear at the bottom right corner as seen by the “density camera”.

q) Run the motor control program. At the top left corner of the desktop, click on "TMC for labview shortcut". A window with a list of options will appear. Go to the bottom of this list and double click on "TMCM_310_testapplication.vi". The motor control window will appear as a separate window. Turn on the black motor control box to the right of the monitor by flipping the toggle switch to "on". Then start the "TMCM_310_testapplication.vi" program by clicking on the arrow in the upper left corner. This will enable movement of the a) sample post, b) UV shutter, and c) carousel.

r) Open the "capture OEM" program on the desktop of PC1 monitor. The visualization camera should already be selected from the drop-down menu at the upper left of the OEM program. Start play. **Note that there are separate mice for PC1 and PC2**. The images of the electrodes will appear, as seen by the visualization camera. If a black and white image appears, it means you are looking through the viscosity camera. Go to the drop-down menu and select the other option to view the visualization camera.

Optical Alignment Check Before Sample Launch

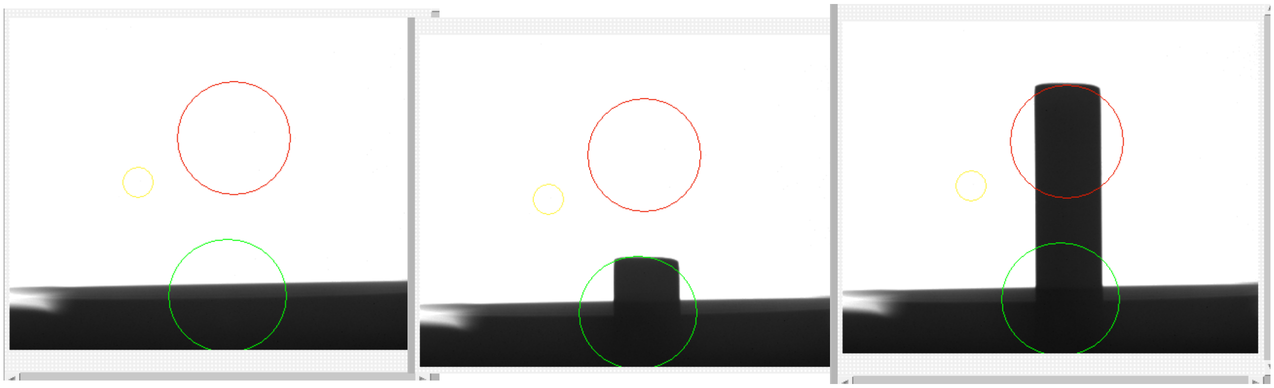

Figure A.5: The three post positions to use for alignment. (Left) post down (middle) post nub (right) post full.

Note: Only attempt this method of alignment with a *straight* sample post. Attempting this method of alignment with a bent post will drastically reduce its effectiveness, as the anisotropy in the post requires you to keep track of how it was inserted into the bottom electrode.

a) Usually, the system is near alignment unless the optical system was disturbed, the ESL chamber was recently opened, the electrodes were cleaned and repositioned. The optical system check should be done when **No Sample is Present**. The post should be moved to three distinct positions: a) down until not visible in the camera, b) slightly above the side electrodes (also called the "nub" in the notebooks), c) up all the way slightly above the typical sample position (the red circle in the density camera, also labeled as "full" in the notebooks). At each position, the optical tables for the Green and Blue LEDs need to be adjusted using the translation and tilt knobs for xlocal values and the vertical knob for ylocal values.

The following settings were found to be best as of November 6, 2019. Note that these values shift over time and you should reference the ESL Notebook for more up-to-date values. After a successful batch of ESL measurements, it is good form to record the X and Y values for the Green and Blue PSDs at the three positions indicated below. Doing so will save you time and headaches later if you are unable to launch a sample because of poor starting alignment.

	Post Down	Post Nub	Post Full
Green xlocal	0.10	0.09	-0.04
Green ylocal	0.17	0.12	-0.14
Blue xlocal	-0.17	-0.10	0.23
Blue ylocal	-0.03	-0.07	-0.27

When adjusted properly, a symmetric image of the post will be seen entering the lenses in front of be the PSD detectors.

Old method for optical alignment

Note: This method is reproduced here for records. Attempting this method of alignment can cause either one or both of the lateral voltages to saturate. Try at your own risk if other alignment methods aren't working.

a) Bring the post down until it is visible a little above the side electrodes.

b) Set the xlocal reading for the green LED to zero by moving the tilt Vernier (small horizontal one) for the optical table. Bring the ylocal reading for the green LED to zero by moving the table along z-direction by adjusting the Vertical Vernier.

c) Set the xlocal reading for the blue LED to zero by moving the large horizontal Vernier attached to the optical table. Bring the ylocal reading for the blue LED to zero by moving the table along z-direction by adjusting the Vertical Vernier.

d) Move the post up above the red circle (region within which the sample floats) in the density camera.

e) Set the xlocal reading for the green LED reading to zero by moving the large horizontal Vernier.

f) Set the xlocal reading for the blue LED to zero by moving the tilt Vernier (the small horizontal one).

Iterate steps a) to f) until no change of the PSD readings occur when the post is moved up and down.

Sample Loading

a) **Make sure that the z-voltage amplifier has been turned off.**

b) Move the post upward toward the top electrode by clicking on motor control for the post in the “TMCM_310_testapplication.vi” program. Set the velocity to 1000-1200. When the post approaches the top electrode, this velocity may be reduced to 300-500 for finer movement. Bring the post close to the top, but don’t allow it to go into the hole in the top electrode. Stop the post to leave a small gap between the top electrode and the post. When a sample is loaded from the carousel, you should see the bottom of it sticking through the top electrode.

If there is no response from the sample post, check that the master power is on for the black motor control box to the right of the computer monitors. Also check that power is on to the motor controlling the post.

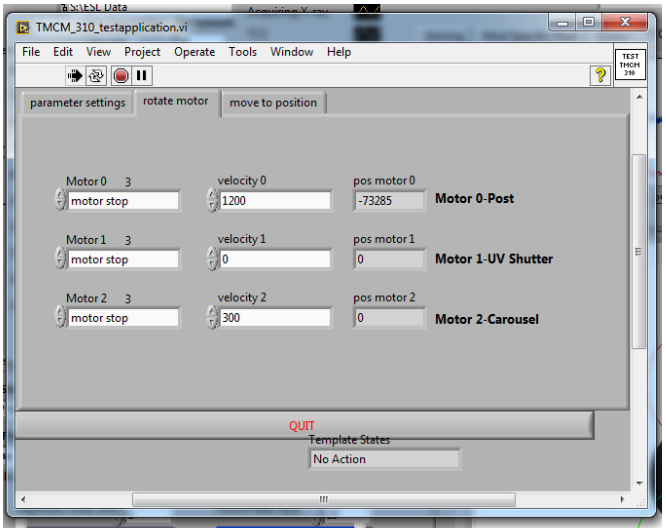

Motor 0 3: motor stop
velocity 0: 1200
pos motor 0: -73285
Motor 0-Post

Motor 1 3: motor stop
velocity 1: 0
pos motor 1: 0
Motor 1-UV Shutter

Motor 2 3: motor stop
velocity 2: 300
pos motor 2: 0
Motor 2-Carousel

Template States: No Action

Figure A.6: The motor control LabVIEW program. The first row (labeled Motor 0-Post) is for the sample post. The middle row (labeled Motor 1-UV Shutter) should not be used unless necessary. Moving the UV shutter can cause it to clip into a PSD. It is also recommended to turn the motor off on the black box, as poor grounding lets the shutter move when other motors run. The last row (Motor 2-Carousel) controls the carousel. To load samples, rotate in the positive direction.

c) Click on the “carousel motor” in the “TMCM_310_testapplication.vi” program. Set the velocity to 300. Click on “positive” (counterclockwise rotation) to select a sample that is down in the list for the carousel samples from the present position. If a sample listed upward from the present position needs to be retrieved, click on “negative” (clockwise rotation). Some numbers will appear to show the progress of the rotation. Typically, it takes the counter reading to change by about 15000 (more, if there is some backlash in the movement) to go from one sample position to the next in the carousel. The first sample of the carousel usually takes awhile to load.

If no sample is loaded after waiting a long time, check that the power to the carousel motor is on. Also check that the gearbox is meshed to the gear controlling carousel rotation. It is located to the left of the main gate valve for the Osaka (large) turbo. If the gear box has shifted away from the gear, *gently* move it back into place, taking care to not rotate the large

gear. Moving this gear can cause a sample to drop and you can lose track of your carousel position. Tighten the gear box down with a hex key.

d) Keep on looking in the visualization camera in PC2. As soon as the sample drops onto the post, stop the carousel motor. Lower the post, you can use any speed (1200 is usually what I use). After some time, the sample will drop from the post onto the Cu bottom electrode. Bring the post down below the bottom electrode. The sample should sit at the center hole of the bottom electrode.

e) If the sample drops on a flat edge (arc melted samples always have one), it does not usually roll over to the center of the bottom electrode. If that happens, we will use the voltage settings in the levitation algorithm to push the sample to the center. Turn on the z-voltage amplifier. Set the z-saturation upper limit to -10000 and lower limit to -15000. Note that the upper and lower limits may have to increase if the sample is not moving. Click on the play button for the Matlab algorithm and then immediately turn the algorithm off ("stop button"). Depending on the size and location of the sample on the bottom electrode, this may be enough to push the sample to the center. If the sample did not move, stop the levitation algorithm and change the saturation z upper limit in increments of -1000 (from -10000 to -11000 to -12000, etc). Start the algorithm again. If the sample moved to the center, change the upper limit back to 0. If not, continue to gently raise the saturation until the sample moves to the center. If the lower saturation limit is reached, increase it by 1000 as well. Be careful with this step, as increasing the saturation too much may cause the sample to fly away.

Launching a Sample

a) Open the "HV_readout_shortcut" in PC1. This program displays x, y, and z voltages continuously as a function of time with a history of 500 seconds. These voltages are direct indicators of sample stability. Keep an eye on these voltages throughout the experiment. The green and blue voltages should be kept as close to zero as possible.

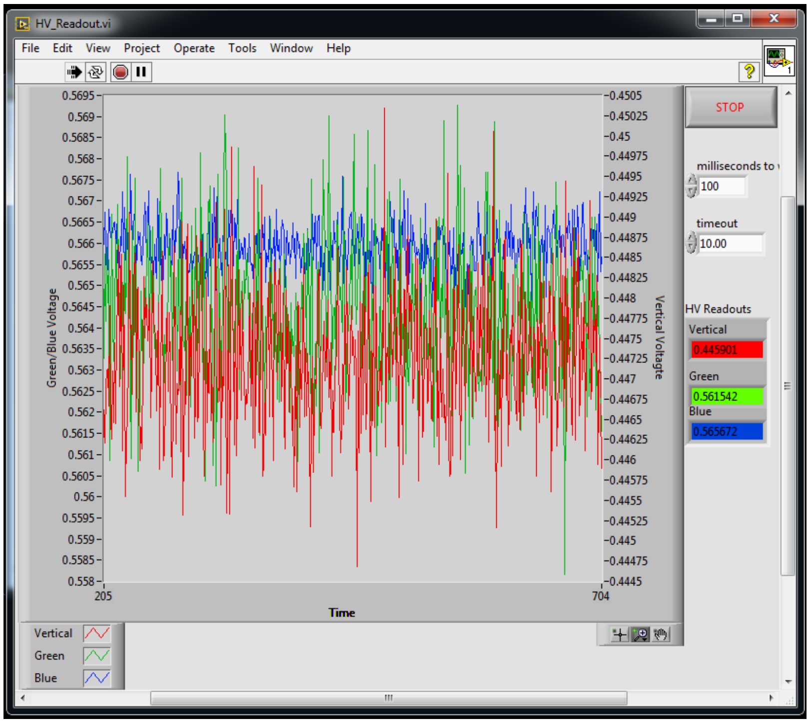

milliseconds to
100

timeout
10.00

HV Readouts
Vertical 0.445901
Green 0.561542
Blue 0.565672

Figure A.7: Screenshot of HV_Readout. Note that the green and blue voltages are read from the left y-axis, while the red vertical voltage is read from the right y-axis. The program will auto-update the x-axis as a function of time after 500 seconds have passed.

b) Make sure that the z-saturation voltages are correct for the sample. Make sure that all x, y, z voltage amplifiers are on. Make sure that the UV source has been turned on and working (the glow can be observed from the window at the back of the instrument and the operating voltage is stable).

c) Raise the sample to the launch position using the post. The post should be flush with the lateral electrodes and you should be able to see almost the entire perimeter of the sample in the density camera. If you only see 50-75% of the perimeter, the sample is too low. If you can clearly see a distinction between the post and lateral electrodes, the sample is likely too high.

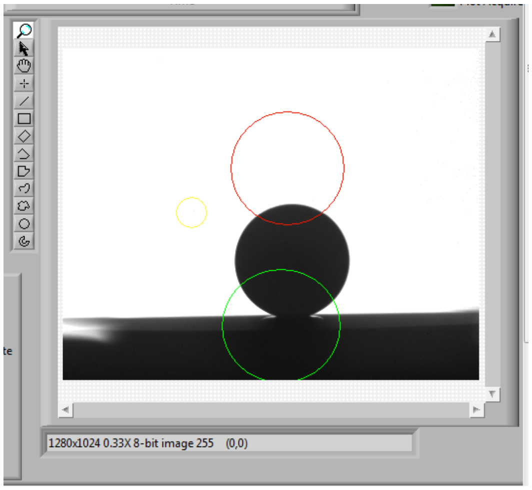

Figure A.8: Launching position for a sample. You may have to go a bit higher or lower depending on the sample and launch stability.

d) Click on the play button in the Matlab xPC Target window to start the algorithm and launch the sample. Immediately after launch, click on “Green y” and change its setting to -0.006. This gives a good stable levitation, however you may need to play with this value. Change the “Blue X” and “Green X” values to -0.006 as well to improve lateral stability. Remember to save these changes for each setting by clicking on the “update parameter” button. If you are launching a WC, you may need to wait for the sample to float higher up before changing Green Y. Switching its value from -0.012 to -0.006 too quickly may cause the sample to drop.

e) Bring the post down below the hole in the bottom electrode so that the post becomes invisible in either of the two cameras.

f) Monitor x, y, and z voltages in PC1. Usually, the z-voltage is between, -4 and -5 KV for most of the samples at room temperature. If higher, the optical alignment may not be good, the UV may be misaligned, malfunctioning, or off, or the sample is very dense (i.e. WC). To check UV functionality, launch a sample with the UV off. Then, when the sample has reached its final levitation position, turn the UV on. You should see a characteristic jump of approximately 0.5 to 1 volts in the vertical voltage trace.

g) Usually, the x and y voltages attain a small non-zero value after launch. If they start rising, you must perform some alignment. You have two options for this. The first is to manually adjust the PSDs using the translation and tilt knobs until the Green and Blue voltages are close to zero. The other option is to slowly modify the "x pos" and "y pos" values within the algorithm. Be extremely careful with this second option, as seemingly small values in either of these parameters can cause the respective voltage to saturate (0.001). Regarding the sign necessary for these adjustments, the rule of thumb is to match the sign of the current voltage readout. For example, if the green voltage is hovering around +3, you should enter a positive value into "x pos". Similarly, a value of -3, you should entire a negative value into "x pos". Slowly change the x and y positions from 0 to either positive or negative values in steps of 0.0001-0.0002 until the x and y voltages approach zero and stays constant. You may also reduce/increase the z-position from 0.0043 to center the sample image in the density camera. Be aware that changing the z-position may change the x and y alignment, requiring you to make a few more adjustments.

If the sample drops, immediately stop the algorithm by pressing the square "stop" button on the TargetPC interface.

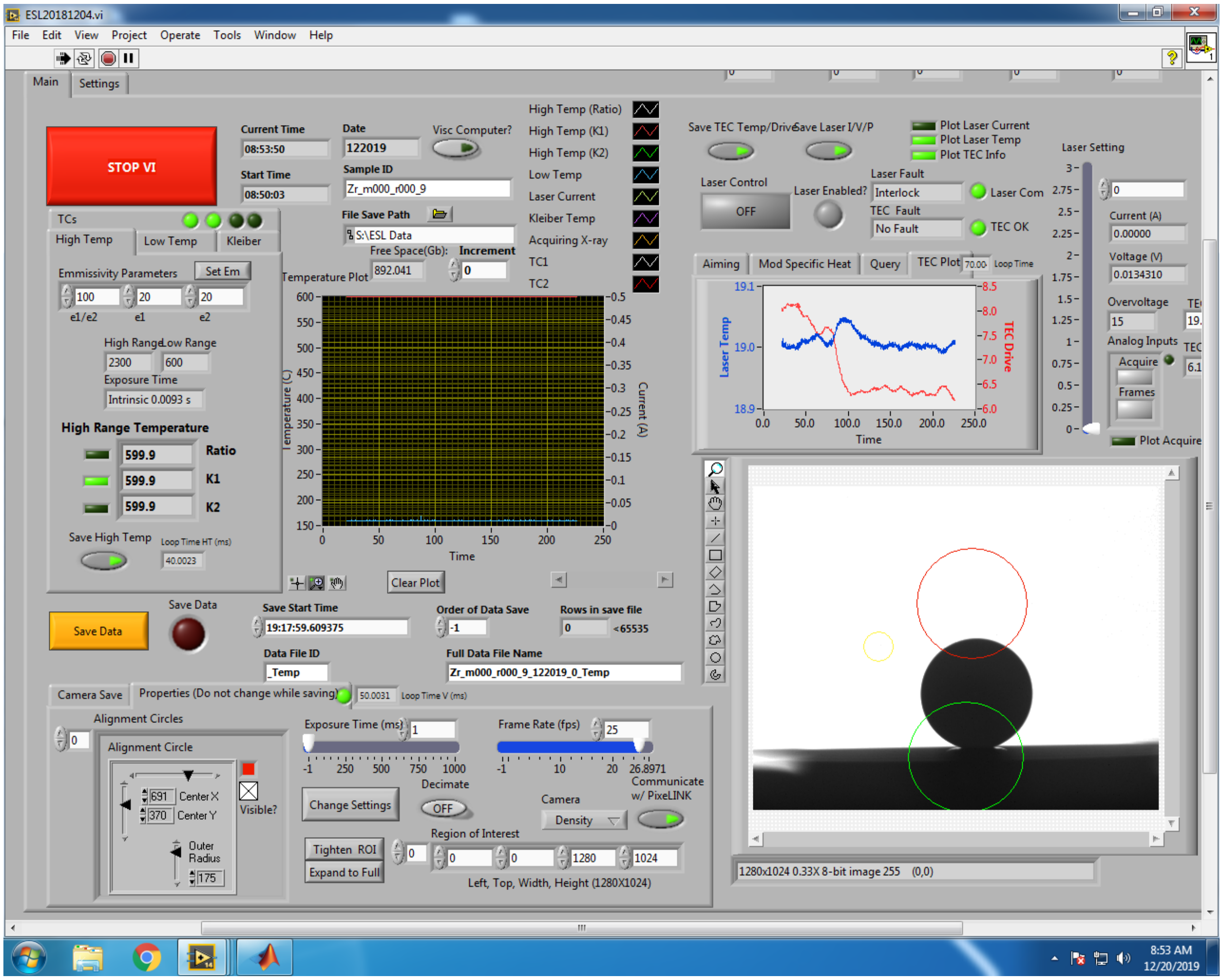

Current Time: 08:53:50

Date: 122019

Start Time: 08:50:03

Sample ID: Zr_m000_r000_9

File Save Path: S:\ESL Data

Free Space(Gb): 892.041

Increment: 0

Emmissivity Parameters: e1/e2 100, e1 20, e2 20

High Range: 2300; Low Range: 600

Exposure Time: Intrinsic 0.0093 s

High Range Temperature: Ratio 599.9; K1 599.9; K2 599.9

Loop Time HT (ms): 40.0023

Laser Fault: Interlock

TEC Fault: No Fault

Laser Setting: 0

Current (A): 0.00000

Voltage (V): 0.0134310

Overvoltage: 15

Loop Time: 70.00

Save Start Time: 19:17:59.609375

Order of Data Save: -1

Rows in save file: 0 <65535

Data File ID: _Temp

Full Data File Name: Zr_m000_r000_9_122019_0_Temp

Loop Time V (ms): 50.0031

Alignment Circles: 0

Center X: 691; Center Y: 370; Outer Radius: 175

Exposure Time (ms): 1

Frame Rate (fps): 25 (26.8971)

Region of Interest: 0; Left, Top, Width, Height (1280X1024): 0, 0, 1280, 1024

1280x1024 0.33X 8-bit image 255 (0,0)

8:53 AM 12/20/2019

Figure A.9: Full screenshot of the ESL program. Refer back to this figure on later steps for general regions of interest within the program.

Processing a Sample

a) To turn on the heating later, go inside the ESL room and close the door behind you. Turn on the key on the console on the left wall that is used for laser safety. Check that the interlock was engaged, indicated by the “entryway closed” light on the console. First press the “press to start” button and then press the “press to exit” button. The alarm will start beeping. Come out of the room and close the door behind you. The beep will stop. The safety light to the upper right of the door should now indicate that the laser is operational and ready for use. At this point, entry into the room will disengage the laser through the tripping of the interlock. The laser must then be turned on by repeating this procedure.

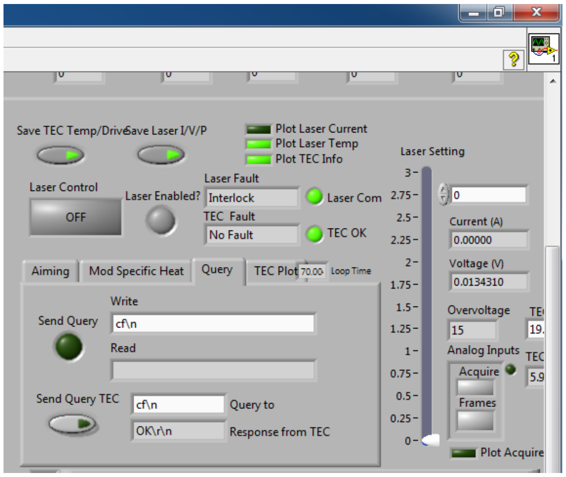

Laser Fault: Interlock

TEC Fault: No Fault

Loop Time: 70.00

Write: cf\n

Read:

Query to: cf\n

Response from TEC: OK\r\n

Laser Setting: 0

Current (A): 0.00000

Voltage (V): 0.0134310

Overvoltage: 15

Figure A.10: Laser query tab. Click on the dark green "send query" button to check for any laser faults (like the interlock, etc). If the "Laser Fault" window reads "No Fault" then the laser can be turned on with the "Laser Control" button. It will turn red and the "Laser enabled" light next to it will turn on. The laser current is controlled on the far-right slider or through direct input of values in the top dialogue box.

b) From the front panel of the ESL program, specify save path for our data. The sample file name and save path are indicated at the top of the program, along the same line as the big red rectangular stop button. First, select the data path. It will take you to a separate window. Usually, data are stored in folders with the name of the month and year (e.g. December2019). Open this folder and then create a sub-folder with a name by date (12122019). Within this sub-folder create a folder with the sample name and **keep this folder open** before exiting this window. In the "ESL_20181204 shortcut" program window, give a name for the data file. We usually include the sample composition and sample mass, e.g. Cu50Zr50_m4523. **<u>DO NOT PRESS ENTER AFTER TYPING THE SAMPLE NAME. Doing so will result in a LabVIEW crash after you click the "Save Data" button.</u>** Simply click anywhere on the screen after entering the filename and it will be saved in the program. Then select 0 or 1 in the “increment” path for the data. This is done because sometime the data file becomes too big. Up to about 66500 lines can be accepted. Therefore, we first store data during the first melt and superheat in one increment, say “increment 0”. All subsequent processing data are stored in “increment 1”, and so on.

c) Once the data file name and path has been selected, click on “save data”, located towards the far left of the panel, below the numerical readouts for the pyrometers. When you stop saving time-temperature data, **ALWAYS** raise the increment by 1. Clicking on save data without raising the increment will cause all of the previous data to be overwritten. Select the pyrometer (low temp for start from room temperature). The time-temperature graph will appear. The low-temperature pyrometer works between 150 and 800 C.

d) We are now well set to heat up the sample. Click on the “query” tab for the laser near the right top corner of the ESL LabVIEW program (Fig. A. 9, Fig. A. 10). Then, press the dark green “send query” button. This will check for any fault in the laser, such as the interlock being tripped. If the send query button gives an “interlock” fault, then make sure the door is completely closed and the main laser control console has power. If everything is working properly, this will enable to turn on the laser. Select a small current for the laser control, typically 0.4 A and click “laser on”. The sample will start to heat as will be visible in the time-temperature data.

e) In the lab notebook start recording the “laser current” (I), “temperature” (T) and “z-voltage” (V) as the sample heats up. Usually, the sample heats up to about 500-550 C quickly with 0.4 A laser current. Not much instability is observed in this temperature range, unless there is a glass-crystal or other type of solid-solid transformation. The z-voltage may show a small rise. Thereafter, increase the current in the increments of 0.01 or 0.02 Amp., depending on the stability of the sample; z-voltage should not change quickly. **If it does, slow down on heating**. **In some cases, long waits and even smaller heater current increments (0.005 A) may be necessary.**

If the sample drops, immediately turn off the laser and the high voltage (click on the stop button within the xPC Target Explorer window).

f) Above about 700 C, switch to the high temperature pyrometer; use the ratio reading. If your sample has an oxide layer such that the ratio is not providing an accurate reading (like in the case of Al-based samples), try switching on K1 or K2 for single color pyrometry. Continue until it starts to melt. This is another temperature zone where care has to be taken. When it starts to melt, the pyrometer reading does not change even when laser current is increased. Go slowly and watch for any instability. At the end of melting, temperature starts to shoot up. If it rises too fast, sample may become unstable. For incongruent melting, the sample often shows instability between the solidus and liquidus. Some samples (e.g. CuZr alloys) show some instability even up to 50 C above the liquidus. **Heat slowly in this temperature region**.

g) Superheat to at least 100 C above the liquidus, before the first cooling. Repeat heating and cooling as necessary to reach the maximum supercooling temperature.

h) Stop data saving for a moment. Go to "Increment 1" and then start data recording again. **If the increment is switched without stopping data saving, new data will overwrite on the old data**. Progressively, superheat and watch supercooling. Usually, after a few cycles, the maximum supercooling is achieved, unless the sample is dirty. For good quality samples, no more than 150-200 C superheat is necessary to achieve a maximum supercool. Once the maximum supercooling is achieved, you should not have to heat as high again.

To preserve the sample, heat by only 150-200 C. If the maximum supercooling temperature is not achieved with that degree of heating, return back to heating it 250-300 C above the liquidus.

i) When finished with all experiments, let the sample cool below about 300 C. It can be kicked out either by changing the “upper limit of the z-saturation” to -10000, or by moving the post towards the sample.

If ever it is necessary to drop (not kick out) the sample onto the bottom electrode, gradually reduce the z-position from 0.0043 to about half (0.0025). Be sure to stop the algorithm before the levitation becomes unstable. It has approximately a 90% success rate and is typically a more reliable way to drop a sample for later processing than simply stopping the levitation algorithm.

What to do when the program crashes

Although not very frequent, sometime the LabVIEW program crashes. If that happens, the sample will still float, since the levitation algorithm is controlled by the target PC.

If the laser was on when the LabVIEW ESL program crashed, it can be turned off by tripping the interlock. On top of the black motor control box are laser goggles with side-shields rated for OD5 at the operating wavelength. Put them on. If anyone else is in the room, have them wear laser goggles or leave the room. Open the door to the ESL room; the interlock should trip and stop the laser’s operation. To ensure this, turn the key on the laser control box to the off position; you can turn it on later after regaining control of levitation and data acquisition.

Familiarize yourself with this procedure before it happens. Speed is critical in order to maintain control of your sample.

a) If you are able (i.e., where the computer did not blue screen), disconnect the target PC from PC1 from the Matlab program. This is a precaution so that no unwanted command goes to the target PC. Close all running programs (including Matlab) in both PC1 And PC2 and restart the computers.
b) Reconnect with the target PC. It is critically important to regain full control of the sample and levitation. Do this step first.
c) Before starting data acquisition, type in the old data file name and flight paths before the crash. Change the "increment" to be one larger than the previous file; otherwise old data will be lost.

If the visualization or viscosity camera freezes / is not available

In rare occasions, the visualization camera freezes or crashes. If that happens, close this program in PC1. Turn off the power to this camera for a few seconds and turn power back on. The power plugs for the camera are labeled and are located on a power strip directly below the Green PSD. Also gently disconnect the camera USB cable and re-connect it. Even if the power is disconnected, there is still a small amount of power coming from the USB; thus, both need to be disconnected to perform a full restart. Open the "capture OEM" program in PC1. If the camera link is not automatically established, check the settings. Open the IPManager program for CaptureOEM on PC1—it has the same desktop icon. They should be:

IP address: 192.168.5.11

Subnet Mask: 255.255.255.0

MAC: 00-11-1C-F3-02-A8

IP Engine Version: 2.3.5

Viscosity camera settings are the following:

IP address: 192.168.5.8 or 192.168.5.9.

Subnet Mask: 255.255.0.0

MAC: 00-11-1C-F3-01-83

IP Engine Version: 2.1.9

If you have issues with the viscosity camera not showing up in CaptureOEM, try increasing the IP address by 1 (192.168.5.8 to 192.168.5.9, for example). You will likely need to adjust ROI settings if you lose communication with the viscosity camera. Ensure you have a 64x64 pixel ROI that is centered on the sample and that the exposure time is short enough to allow for 1500fps.

Sample fell into gap between lateral and bottom electrodes

In this case, your only option is to get rid of the sample. Otherwise, the chamber must be opened. To get rid of the sample, turn off the lateral voltage amplifiers. The sample may have tripped one of the amplifiers anyway, due to making a connection between the lateral electrode and bottom electrode.

Follow the same procedure for removing the sample if it was levitating. Try raising the post to the launch position or slightly higher, even if the sample is stuck on one of the lateral electrodes. This way, the PSDs see an object and will attempt to levitate it. Run the algorithm with the saturation settings for kicking out a sample (Saturation Z Upper Limit = Saturation Z Lower Limit). You may have to visually inspect the bottom electrode assembly through one of the open ESL ports. Otherwise, you will need to open the chamber and manually remove the sample. If you are quick, you can quickly pump back down to 10^{-8} Torr after a night.

If this happens regularly, consider screwing in the bottom electrode a bit more to minimize the shelf available for samples to fall onto.

Issues related to TargetPC communication

If you are unable to connect to the TargetPC because of a communication error, there may be several causes. It is not possible to list all problems, as some of them are related to specific IP address, Mask, protocols, or other computer settings. If that is the problem, enlist the help of Rich Schmaeng to help you. It will require significant use of the Windows DOS console to ping PCs on the local network to pinpoint the exact communication setting.

It is possible the control algorithm CD was corrupted. It is unlikely this occurred but burning a fresh disk may fix the problem. The instructions may be found on page 10 of the 06/28/2018 notebook. Be sure to use the echtgain ending in “20180726” if you are building any new algorithms, although this is not necessary since gain-switching is robust against sample size.

Previous versions of echtgain have flipped the blue and green PSDs, making it impossible to levitate at all. Steps to burn the CD are reproduced here:

To create a burn disk—format the CD first, default settings are fine. Burn the algorithm to CD using the built-in Matlab "burn to CD" function. Move copy of cdboot.iso to folder on the computer. Load in a new CD. Burn the .iso file to the new CD. Load this CD into the TargetPC.

One possible cause of this problem is related to peculiarities of the algorithm. The TargetPC has a built-in floppy drive, yet the control algorithm runs through CDs. Matlab attempts to run algorithms through the floppy drive. As such, it may be necessary to enter the BIOS for the TargetPC and check if the floppy drive is active.

Unstable levitation or completely unable to levitate samples.

The A->D or D->A cards may need to be recalibrated. Log into Windows (password phys2day) on the TargetPC and run the built-in LabVIEW card calibration software (NIMAX). The cables will need to be unplugged from the PSD router box, which maps the pins on the new cards to the old PSD setup. Run the self-test and self-calibration options. You may have to do this several times if you receive a failure notice. If the failure persists, take down the error code. If calibration fails, the cards may need to be replaced. We have purchased one set of replacement cards that live in Compton 150/152 on the workbench. They are next to the gray filing cabinet that is against the window facing the door to 152, unless they've been moved by someone else.

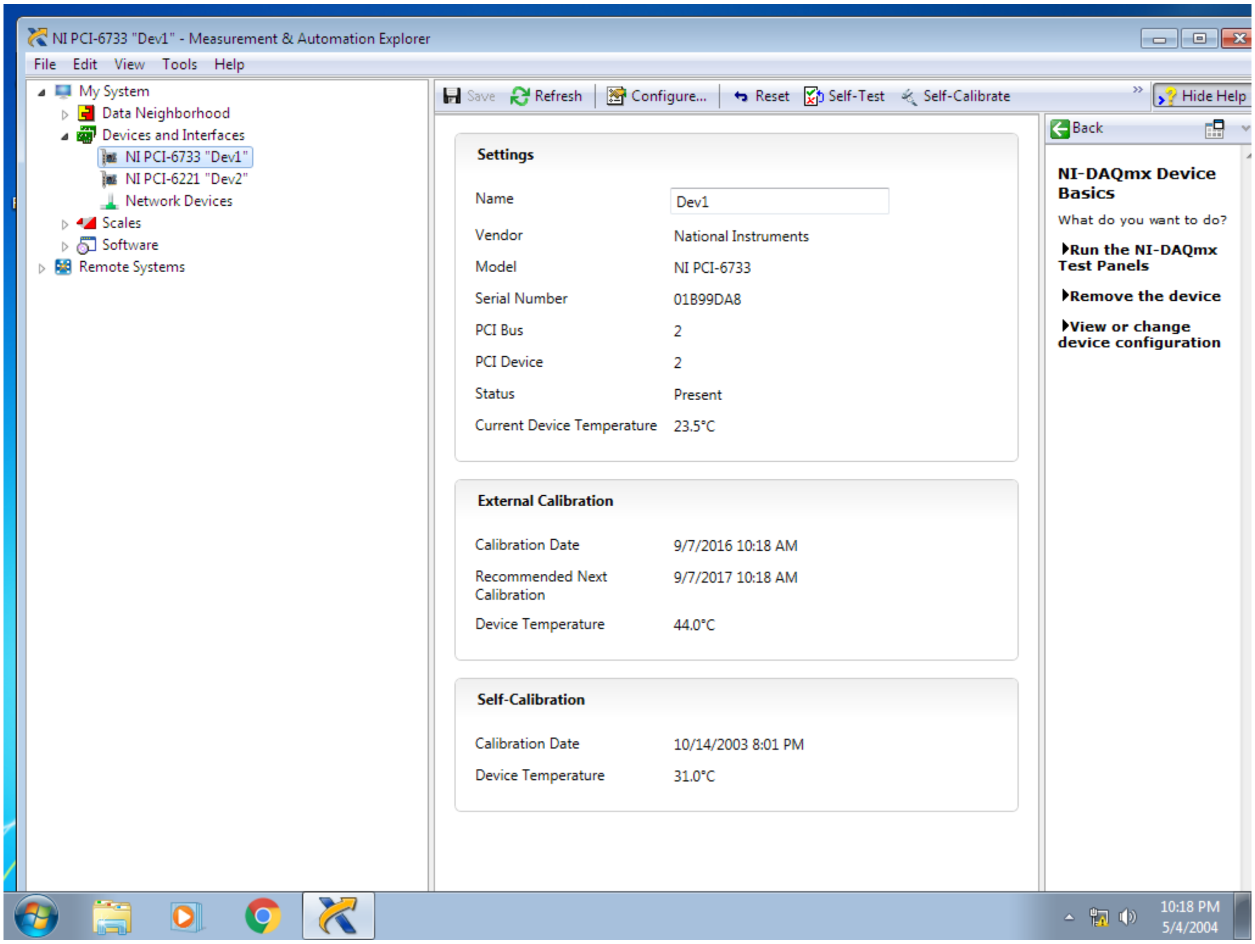

Settings

Name	Dev1
Vendor	National Instruments
Model	NI PCI-6733
Serial Number	01B99DA8
PCI Bus	2
PCI Device	2
Status	Present
Current Device Temperature	23.5°C

External Calibration

Calibration Date	9/7/2016 10:18 AM
Recommended Next Calibration	9/7/2017 10:18 AM
Device Temperature	44.0°C

Self-Calibration

Calibration Date	10/14/2003 8:01 PM
Device Temperature	31.0°C

Figure A.11: The NIMAX window on the TargetPC for recalibrating and testing the A to D and D to A cards. Note that these options are on the top ribbon, in-line with the “Refresh” icon.

For other troubleshooting and operating procedures, read the dissertations of James Bendert and Matt Blodgett.

Density Measurement

Whenever, density measurements are planned, before levitating the sample, a WC standard should be floated and video data for this calibration standard should be taken. In case that is forgotten, video data for a WC standard may be taken after sample measurements are completed.

a. After the sample/WC standard is floated, check that the “link” button in the density measurement menu (at the bottom right corner) is activated. It will turn green and the density video will be linked to the time-temperature measurements. You can check this by watching the timestamp update itself on the “Full Video Name” string.

b. Select the region of interest (ROI). This is done to reduce the file sizes of the video images. This can be done by clicking on the tightening ROI and then selecting an area of interest around the sample. Or, the ROI can be selected by entering the following numbers (corresponding to left, top, width, and height): 225/75/745/600.

b) And then click “change settings”. A smaller area around the sample will be visible in the density camera image. Whatever ROI settings you use for WC should be replicated for your other samples.

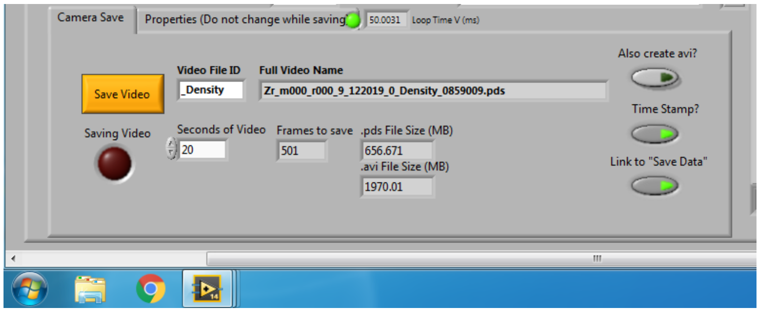

50.0031 Loop Time V (ms)

Video File ID: _Density

Full Video Name: Zr_m000_r000_9_122019_0_Density_0859009.pds

Seconds of Video: 20

Frames to save: 501

.pds File Size (MB): 656.671

.avi File Size (MB): 1970.01

Figure A.12: The Density Camera “Camera Save” tab. Note the “Link to Save Data” button is on. To stop saving video, click that button off. You can also change the seconds of video saved in this tab. To save video, click on the yellow “Save Video” button.

a. Usually, the video recording is made for 60s at 10 fps for the WC standard and 20s at 25 fps for the sample. Exposure time is typically set at 1s. After making these changes, click again on “change settings”.

b. Begin saving temperature data if not already. For WC, you do not need to heat the sample at all. At the bottom of the ESL LabVIEW program is a tab for saving density video. Click on "save video", which will move to the next screen. Make sure that the "link" button is green. Start recording. To save only one video, click on the "link" button after recording has started. This will finish saving video at the end of the current timeframe. Otherwise, it will start a new 60s or 20s video immediately after the completion of the first run. Multiple videos may be needed for samples with prolonged supercooling cycles. Make sure that you activate the "link" after completion of this run so that the system stays ready for the next density recording session.

c. For WC, we normally take 2-3 recordings for 60s each. For the sample, it is first heated to the desired temperature, then video recording is started just before the laser is turned off. Data are collected until crystallization. Density of the solid may also be measured. However, because of the surface roughness and slightly irregular shape of the sample, the density data are noisy.

Viscosity Measurement

Note: If you have already taken time-temperature or density data without the viscosity acquisition program running, you must restart the PC2 computer before acquiring viscosity data.

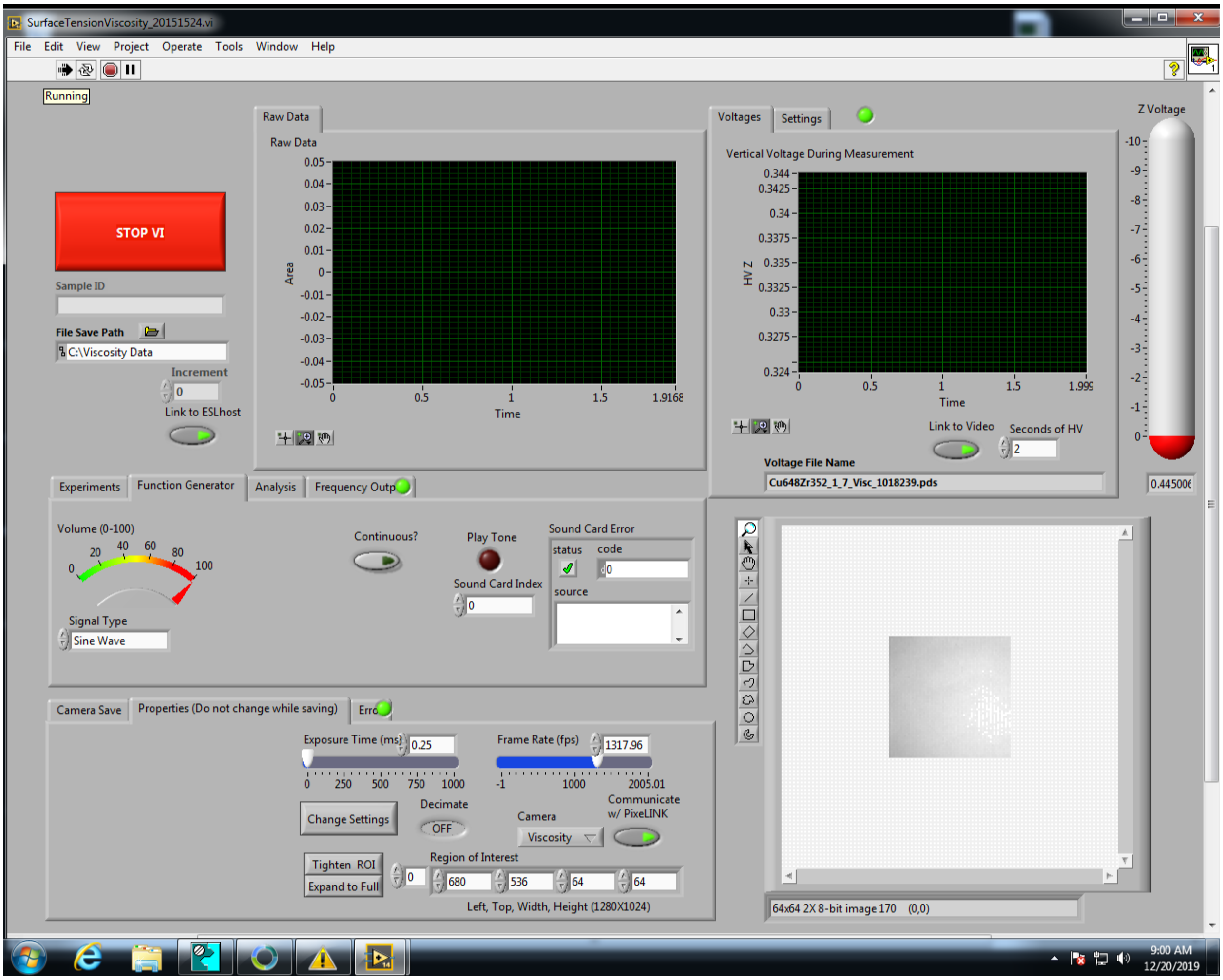

Sample ID

File Save Path: C:\Viscosity Data

Increment: 0

Link to ESLhost

Seconds of HV: 2

Voltage File Name: Cu648Zr352_1_7_Visc_1018239.pds

Z Voltage: 0.44500€

Signal Type: Sine Wave

Sound Card Index: 0

Sound Card Error: status ✓, code 0, source

Exposure Time (ms): 0.25

Frame Rate (fps): 1317.96

Decimate: OFF

Camera: Viscosity

Region of Interest: 0, 680, 536, 64, 64

Left, Top, Width, Height (1280X1024)

64x64 2X 8-bit image 170 (0,0)

9:00 AM
12/20/2019

Figure A.13: Screenshot of the main viscosity acquisition program. The ROI of the video can be changed towards the bottom of the program, much like the density capture program. Adjust the ROI first and minimize the exposure time before slowly increasing the FPS to 1500.

a) Open the “surface tension viscosity shortcut” program in PC1 and click the “run” arrow.

   a. Establish a link to the viscosity computer (PC1) from the “ESL_20181204_shortcut” program that records all experimental data from the ESL runs. Within the ESL LabVIEW program, click the button at the top of the window ***before*** running the ESL_20181204 program. If the button is pressed while the ESL program is running, LabVIEW will crash. If the button is pressed before running the ESL program and then you run the ESL program without the viscosity data program running on PC1, LabVIEW will crash.

The correct order is to open the surface tension and viscosity program, run it, open the ESL_20181204 program, click the link button, and then run the ESL program.

b. Make sure that the “data socket server” and “synergy” in PC1 are active. Usually, they are turned on when PC1 is started. If by any chance they are deactivated (it happened to me once while minimizing these icons), link between PC2 and PC1 cannot be established. When they are connected, the data socket program will show activities like number of “data packets received”, etc. If you are having issues with the Data Socket Server, in the words of the wise Dr. Robert Ashcraft “change things until it works” within the Data Socket Server Manager program.

c. If the two computers are properly connected, the same sample ID from PC2 will appear in the viscosity program. The sample oscillations may be induced by “sine”, “square”, “triangular” waves from the “Function Generator” menu. Usually, sinewave excitations are suitable. Sometimes, it is easier to excite oscillations with “triangular” or “square” voltages.

d. Keep the sample heated above the liquidus. Since it takes some time to probe the oscillation frequency, this temperature should not be kept too high to avoid evaporation loss from the sample. When performing measurements, try to acquire supercooled viscosity data first, as high temperature viscosity measurements for prolonged periods of time can result in significant mass loss and compositional changes.

e. Several parameters within the program much be changed to perform viscosity measurements.

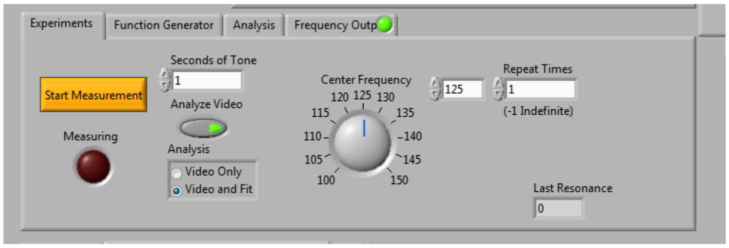

Seconds of Tone 1

Center Frequency 125

Repeat Times 1 (-1 Indefinite)

Analysis ○ Video Only ● Video and Fit

Last Resonance 0

Figure A.14: The Experiments tab from the viscosity program. The box to the right of the Center Frequency knob allows for specific frequencies to be inputted. The repeat time can be changed to any integer value or -1 for constant pulses.

b) Choose an oscillation frequency in the “experiments” menu. The resonance frequency of most of the samples lie between 100 and 150 Hz.

c) Select a region of interest, typically 740/535/64/64. A smaller image around the sample will appear. You may play with the above numbers to change the area of interest. Make sure you can see the entire perimeter of the sample clearly against the background

d) Select an exposure time of 0.04s. If it does not give good contrast, you may need to change it. However, the program may crash if you chose too high a value. Slowly modify the exposure time in increments from 0.05 to 0.1 seconds until a clear distinction is made between the sample and background.

e) With the exposure time and ROI set, slowly raise the frame rate to 1500. If you change this first, LabVIEW will likely have a memory full crash.

f) Excite the liquid drop once by clicking on the “Start Measurement”. The voltage profile and sample area profiles will appear in two graphical forms at the top right corner of this window. Some sample movement will also be noticeable in the density camera image in PC2.

g) Keep changing the frequency until a nice oscillation pattern is established. The area change will show a very nice smooth exponential decay. Reference James Bendert's, Matt Blodgett's, and Chris Pueblo's Ph.D. theses for images on "good" oscillations.

    a. Continue taking measurements once good oscillations have been found by changing the "repeat time" to -1. With this setting, when the "start measurement" button is clicked, the program will take data by continuously exciting the sample every 1s. This can be stopped by either clicking on the "start measurement" or changing the "repeat time" to 1.

    b. Change the sample temperature either manually by slowly reducing/increasing the heater voltage. The laser current may also be reduced at a certain rate automatically from the "Mod Specific Heat" menu in the main ESL program (located in the family of tabs controlling the laser query). From the "Mod Specific Heat" section, you can choose to either raise or lower the laser power in designated increments over a number of steps each lasting a set amount of time. This is useful to automatically change the laser power, enabling the user to focus on finding good viscosity oscillations. Continue taking oscillation measurements as you change the temperature.

    c. As the sample cools down, its viscosity and surface tension increases, which will change the resonance frequency. Below a certain temperature when the viscosity exceeds about 0.1 Pa·s, the damping becomes so fast that further measurements become impossible. If you cannot reliably attain good oscillations anymore, the liquid is either too viscous or too fluid.

Further information about density and viscosity data acquisition can be found in James Bendert's thesis and information about data analysis can be found in the thesis of Chris Pueblo.